Modification of Surfaces with Buckybowls: Fivefold Symmetry and Two-Dimensional Self-Assembly

---

Dissertation
zur
Erlangung der naturwissenschaftlichen Doktorwürde
(Dr. sc. nat.)
vorgelegt der
Mathematisch-naturwissenschaftlichen Fakultät
der
Universität Zürich
von

Quirin Sebastian Stöckl

aus
Deutschland

Promotionskomitee:

Prof. Dr. Karl-Heinz Ernst (Vorsitz)
Prof. Dr. Kim Baldridge
Prof. Dr. Jay S. Siegel
Prof. Dr. Jürg Osterwalder

Zürich, 2014

Dedicated to my family

Kurzfassung

Fünffach-Symmetrie ist unvereinbar mit allen Translationsordnungen aller 17 Symmetrieformen in der ebenen kristallographischen Gruppe, und es ist daher von Interesse die zweidimensionalen Selbstorganisationen dieser Moleküle zu verstehen. Studien von organischen, schalenförmigen Molekülen (Buckybowls) auf Einkristalloberflächen, insbesondere Cu(111) und Cu(100), wurden durchgeführt, um die grundlegenden Prinzipien der intermolekularen Wechselwirkungen zwischen Molekülen in zweidimensionalen Clustern und Verbünden besser zu verstehen. Um Struktur und Aufbaumechanismen von zweidimensionalen Kristallen zu untersuchen, kamen moderne Methoden zum Einsatz, u.a. Rastertunnelmikroskopie, Beugung langsamer Elektronen, Röntgenphotoelektronenspektroskopie, Ultraviolettphotoelektronenspektroskopie, thermische Desorptionsspektroskopie sowie Infrarot-Reflexions-Absorptions-Spektroskopie. Untersucht, wurden die supramolekularen Anordnungen auf Metalloberflächen acht verschiedener Buckybowls (Fig. 1). Perdeutero-corannulen **2** ($C_{20}D_{10}$) zeigt reversible Phasentransformationen beim Abkühlen. Pentaphenyl-corannulen **5** ($C_{20}H_{30}$) zeigt eine Verzahnung der Phenylgruppen mit streifenähnlicher Ordnung. Mono-indenocorannulen **6** ($C_{26}H_{12}$) zeigt eine Zickzack Phase und $C_{32}H_{12}$-buckybowl **7** Streifenphasen. $C_{38}H_{14}$-buckybowl **8** zeigt eine Rosettenstruktur, Streifen, und eine Zickzack Phase. Frühere Studien von Corannulen **1** ($C_{20}H_{10}$), zeigen reversible Phasentransformationen beim Abkühlen, identisch zu **2**. Ebenfalls bekannte Studien an Pentachloro-corannulen **3** ($C_{20}H_5Cl_5$), welches eine Streifenphase zeigt und Pentamethyl-corannulen **4** ($C_{25}H_{12}$) welches u.a. eine Rotationsphase mit gemittleter hexagonaler Ordnung zeigt, werden zum Vergleich herangezogen. Die Packungsmuster von fünffach symmetrischen Molekülen (**1** bis **5**) zeigen identische Orientierungen welche für starre Pentagon und fünffach Sterne gefunden wurden.

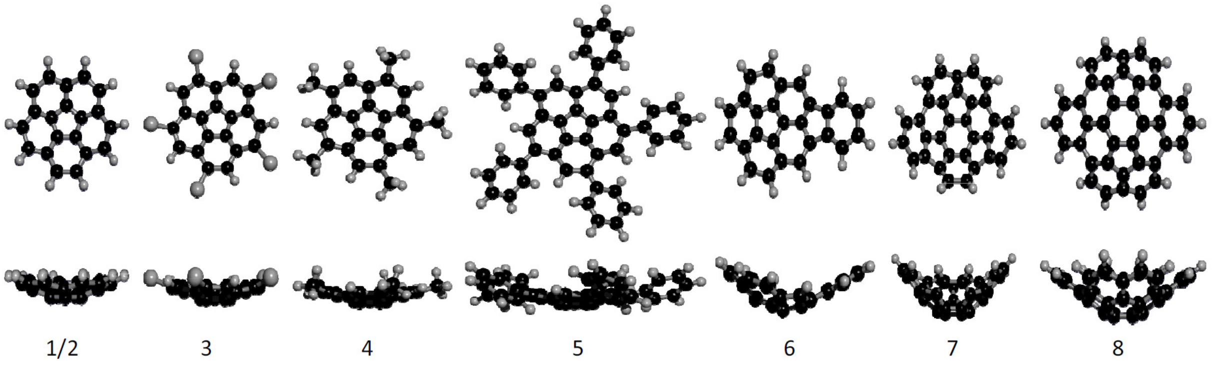

Figure 1.: Drauf- und Seitenansicht der acht untersuchten Buckybowls.

Abstract

Fivefold symmetry is incompatible with the translational order in all 17 plane groups and this system is therefore of fundamental interest for two dimensional crystallization processes. A model study on single crystal surfaces, e.g. Cu(111) and Cu(100), has been carried out to better understand the fundamental principles of intermolecular interactions between corannulene and corannulene derivatives in two-dimensional clusters and lattices, including those consisting of fivefold symmetric bowl-shaped (buckybowl) molecules. In this study, rational molecular design and state of the art surface science methods, e.g. Scanning Tunneling Microscopy, Low Energy Electron Diffraction, X-Ray Photoelectron Spectroscopy, Ultraviolet Photoelectron Spectroscopy, Temperature Programmed Desorption, and Reflection Adsorption Infrared Spectroscopy were applied. The supramolecular arrangement at the surface was addressed with eight different buckybowls (Fig. 2). Perdeutero-corannulene **2** ($C_{20}D_{10}$) exhibits reversible phase transitions upon cooling. Pentaphenyl-corannulene **5** ($C_{20}H_{30}$) displays interdigitation of the phenyl-groups with stripe-like order. Mono-indenocorannulene **6** ($C_{26}H_{12}$) exhibits zig-zag rows and the $C_{32}H_{12}$-buckybowl **7** also shows a stripe-like order. $C_{38}H_{14}$-buckybowl **8** shows rosettes, stripes, azimuthal stripes, and zig-zag phases. The previous studied corannulene **1** ($C_{20}H_{10}$), exhibits reversible phase transitions upon cooling, identical to **2**. Also known studies from pentachloro-corannulene **3** ($C_{20}H_5Cl_5$), which has a stripe-like phase and pentamethyl-corannulene **4** ($C_{25}H_{12}$), which has a rotator phase with average hexagonal order, are compared to the new results. The packings of fivefold symmetric molecules (**1** to **5**) was found to exhibit the same patterns upon adsorption as identified in the closest packings of hard pentagons and five-pointed stars.

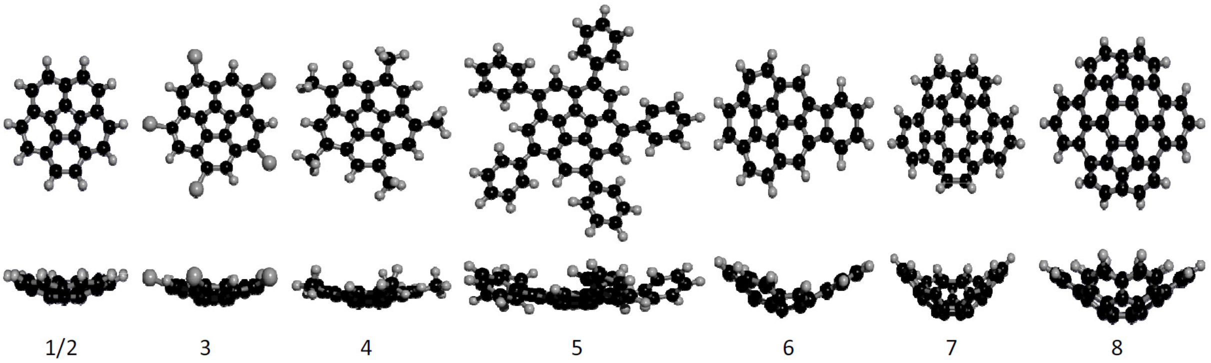

Figure 2.: Top- and side view of the eight buckybowl compounds studied.

Contents

Abbreviations

Scientific Abbreviations

2D	Two-dimensional
CNT	Carbon Nanotube
DFT	Density Functional Theory
DFT-D	Dispersion-enabled Density Functional Theory
DSSC	Dye-Sensitized Solar Cell
EA	Electron Affinity
ESCA	Electron Spectroscopy for Chemical Analysis
fcc	Face-Centered Cubic
FFT	Fast-Fourier-Transformation
FTIR	Fourier Transform Infrared Spectroscopy
FVP	Flash Vacuum Pyrolysis
hcp	Hexagonal-Closed-Packed
HOMO	Highest Occupied Molecular Orbital
IP	Ion Pump
IR	Infrared
LEED	Low Energy Electron Diffraction
LT	Low Temperature
ML	Monolayer
MO	Molecular Orbital
MS	Mass Spectrometer
OLED	Organic Light-Emitting Diode
OTFT	Organic Thin Film Transistors
PES	Photoelectron Spectroscopy
POAV	π-Orbital Axis Vector
QDSC	Quantum Dot Solar Cell
RAIRS	Reflection Adsorption Infrared Spectroscopy
RT	Room Temperature

RX	Reaction Coordinate
STM	Scanning Tunneling Microscopy
SWCNT	Single-Walled Carbon Nanotube
TP	Turbomolecular Pump
TPD	Temperature Programmed Desorption
UHV	Ultrahigh Vacuum
UPS	Ultraviolet Photoelectron Spectroscopy
UV	Ultraviolet
VT-STM	Variable Temperature Scanning Tunneling Microscope
XPS	X-Ray Photoelectron Spectroscopy

Chemical Elements and Compounds

1	Corannulene ($C_{20}H_{10}$)
2	Perdeutero-corannulene ($C_{20}D_{10}$)
3	Pentachloro-corannulene ($Cl_5C_{20}H_5$)
4	Pentamethyl-corannulene ($C_{25}H_{20}$)
5	Pentaphenyl-corannulene ($C_{50}H_{30}$)
6	Mono-indenocorannulene ($C_{26}H_{12}$)
7	$C_{32}H_{12}$-buckybowl
8	$C_{38}H_{14}$-buckybowl

CIGS	$Cu(In,Ga)(S,Se)_2$
dba	Dibenzylideneacetone
DBU	Diazabicycloundecene
DDQ	Dichlorodicyanobenzoquinone
DME	1,2-dimethoxyethane
DMF	*N,N'*-dimethylformamide
dppf	1,1'-bis(diphenylphosphino)ferrocene
dppp	1,3-bis(diphenylphosphino)propane
ITO	Indium tin oxide
PBN	Pyrolytic boron nitride
THF	Tetrahydrofuran

1. Motivation & Introduction

1.1. Why buckybowls?

The discovery of the electrical conductivity of organic molecules in 1977 by Shirakawa *et al.* [1] was the groundbreaking step leading to the application of organic molecules other than in synthetic fibers, plastics, drugs, etc.: In recent years, organic molecules have found their way into the field of organic electronics, for example as cheap host and electrode materials in organic lithium-ion batteries [2, 3] as well as in organic light-emitting diode (*OLED*)-technology [4–7], organic thin film transistors (*OTFT*) [8, 9], organic semiconductors [10, 11], and organic photovoltaics (organic solar cells, Appendix A9) [12–17]. Functionalized aromatic hydrocarbons play a key role in the modification of the surface of new materials systems for molecular electronics. Buckyballs, such as buckminsterfullerene C_{60}, have a great potential as electron acceptor material in organic photovoltaic cells. However, bowl-shaped molecules (buckybowls) such as corannulene may soon find use in organic photovoltaic cells as well. The corannulene **1** molecule (Fig. 1.2 and section 1.2) accepts four electrons (charge density of 0.2 electrons per C-atom) and is therefore a better electron acceptor than C_{60}, which accepts six electrons (charge density of 0.1 electrons per C-atom). Furthermore, **1** is more soluble than C_{60}. The combination of larger charge density and solubility makes corannulene more technically suitable than C_{60} for application as acceptors in organic photovoltaics.
Studies from Kato *et al.* [18] suggest that the monoanion of **1** may become superconducting with calculated transition temperatures T_C in the range of $29.17 \ldots 65.56\ \mathrm{K}$, while C_{60} buckminsterfullerene-based solids have less favorable transition temperatures ranging up to $33\ \mathrm{K}$, with that of C_{60} doped with potassium as low as $18\ \mathrm{K}$ [19–21]. Therefore, corannulenes may also be more suitable than buckyballs for use in superconducting materials.

In yet another possible application, bio-conjugated **1** may lead to new approaches to cure diseases [22]. In particular, host-guest systems containing corannulene [23–25] can be used for micro-encapsulation of drugs [26] and the fabrication of nanomembranes [27].

From a more fundamental point of view, **1** can be used to explore aspects of molecular recognition such as $\pi - \pi$ interactions and/or the influence of concave and convex sides in these interactions [28–31] and self-assembly behavior [32–36]. The intermolecular interactions between bowl-shaped molecules has so far not been explored with regard to the size of the bowls.

Corannulene's fivefold symmetric structure is incompatible with all 17 crystallographic plane groups and is therefore of fundamental interest for those studying two-dimensional (*2D*) crystallization processes for the aforementioned new material systems.

Despite the fact that organic molecules are already found in electronic devices, a better fundamental understanding of the adsorption, intramolecular interactions, and metal-organic interfaces of these new compounds is needed in order to improve and adjust their physical properties. Knowing the relationship between the interface structure and work function of a material is crucial for predicting the electronic properties of new devices. The work described herein addresses the self-assembly behavior, molecular recognition, and electronic properties of (fivefold symmetric) corannulene derivatives and other buckybowls, namely perdeutero-corannulene **2**, pentaphenyl-corannulene **5**, mono-indenocorannulene **6**, $C_{32}H_{12}$-buckybowl **7**, and $C_{38}H_{14}$-buckybowl **8** (Fig. 1.1). For comparison, the results of previous studies of corannulene **1**, pentachloro-corannulene **3**, and pentamethyl-corannulene **4** are shortly summarized in chapter 3.

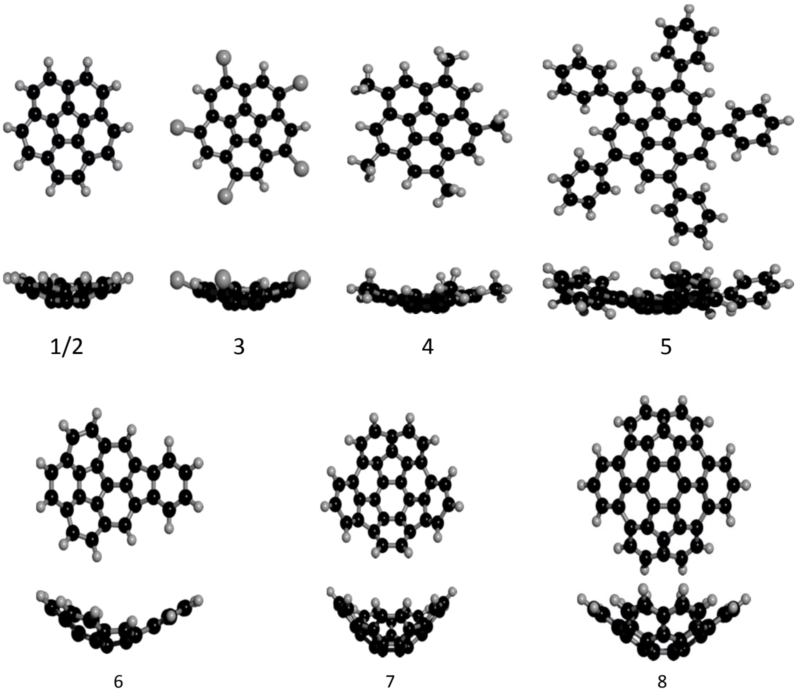

Figure 1.1.: Side- and top-views of buckybowls studied (or discussed) in this thesis.

1.2. Corannulene

The bowl-shaped corannulene ($C_{20}H_{10}$) **1** molecule, often denoted as the smallest fragment of the famous C_{60} buckminsterfullerene, was first synthesized by Barth and Lawton in 1965 [37]. Molecular orbital calculation and the anion and cation radical determination followed one year later [38, 39]. Confirmation of its fivefold symmetric molecular structure came via X-ray diffraction in 1976 [40]. Fifteen years later, the "parent" molecule, C_{60}, was obtained by Kroto *et al.* [41] (Fig. 1.2). Further optimization for improving the yield and purity of the synthesis of **1** [42–47] culminated in the kilogram-scale synthesis [48].

Numerous derivatives of corannulene have been synthesized and their structural, electronic, and chemical properties investigated ($>$ *80* publications). Embedding **1** into larger aromatic ring complexes was also successful, and **1**/metal-complexes have been prepared ($>$ *50* publications).

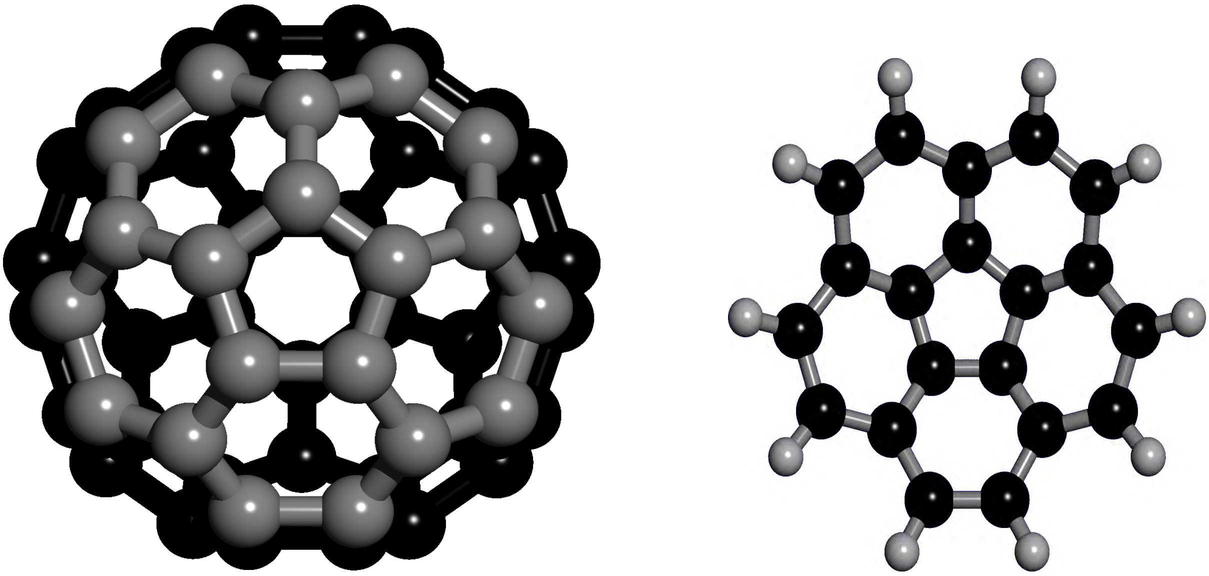

Figure 1.2.: Left: Buckminsterfullerene with corannulene, the smallest curved fragment of C_{60},highlighted in gray. **Right:** Carbon-rim atoms of the fullerene-fragment are mono-hydrogenated to give corannulene.

1.2.1. Properties

Chemical & Physical Properties

Although **1** is not a planar molecule it has many aspects of aromaticity, e.g. all the atoms are arranged in rings in a completely conjugated π system. Specifically, there are resonance forms in which the π-electron distribution (Fig. 1.3) fulfils Hückel´s rule [49–51] of $4n+2$ π-electrons within the two almost coplanar ring systems (the outer aromatic ring having 14 electrons and the inner five-membered ring having six electrons). Aromatic molecules show an enhanced chemical stability compared to their similar non-aromatic derivatives. Destabilized anti-aromatic molecules (i.e., planar monocyclic molecules with $4n$ π-electrons) change their electronic and/or conformational structure to obtain a more stable configuration (e.g. asymmetry of cyclobutadiene). Hirsch *et al.* proposed a new way to determine three-dimensional aromaticity with $2(n+1)^2$ π-electrons [52].

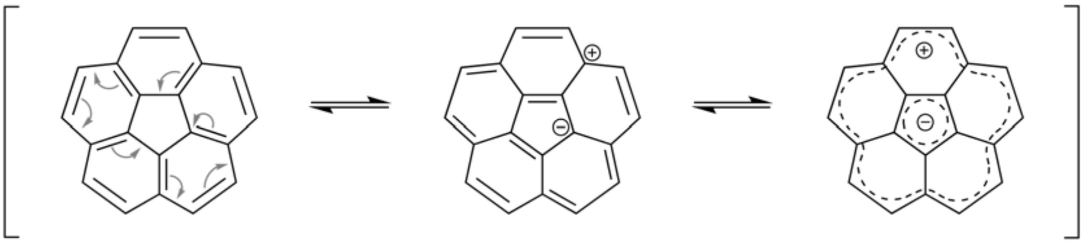

Figure 1.3.: Corannulene and polarized **1**. The inner ring contains 6e⁻ and the outer ring contains 14e⁻, with the two conjugated π electron systems both obeying Hückel's $4n+2$ rule.

Some of corannulene´s thoroughly studied properties are listed in Table 1.1, together with those of its penta-substituted derivative, **4**. At room temperature (*RT*) **1** exhibits rapid bowl-to-bowl inversion with a planar transition state [53], a energy-barrier of inversion of 11.5 ± 0.6 kcal/mol and a bowl-depth of 0.875 Å (Fig. 1.4) [40]. Asymmetric substitutions induce chirality in corannulene. While rapid inversion generates the racemate in the gas-phase, adsorption onto a substrate traps either the left- or right-handed species. A comparison of bowl-depth and bowl-to-bowl inversion barriers of all molecules investigated in this thesis are shown in Table 1.2. A quartic description (Equ. 1.1) can be found for the relation of bowl-depth and the inversion barrier (Fig. 1.6) [54], although it is only valid for simple substituted **1** and mono-indenocorannulene derivatives; as soon as the bowl gets too deep (like for **7** and **8**), the calculated energy inversion barrier is too high (Equ. 1.2 for **8**). These larger bowls favour a wave-like inversion, although this is not possible at *RT* due to their increased inversion barrier. The so-called π-orbital axis vector (*POAV*) is a good definition to measure the curvature and/or the strain in bowl-shaped molecules (Fig. 1.5).

$$E = ax^4 - bx^2 = -11.5 \quad \text{(for corannulene)} \tag{1.1a}$$

$$\frac{dE}{dx} = 4ax^3 - 2bx = 0 \ \rightarrow x = 0.875 \ \Rightarrow \ a = 19.60\,,\ b = 30.03 \tag{1.1b}$$

$$E_{inv} = cx^4 \ \Rightarrow \ E_{inv}(x = x_{Cor}) = cx^4_{Cor} = -11.5 \ \Rightarrow \ c = -11.5/x^4_{Cor} \tag{1.1c}$$

$$E_{inv} = \left(\frac{x_{new}}{x_{Cor}}\right)^4 \cdot -11.5\,\frac{kcal}{mol} = \left(\frac{2.264}{0.875}\right)^4 \cdot 11.5\,\frac{kcal}{mol} = 515.4\,\frac{kcal}{mol} \tag{1.2}$$

Table 1.1.: Summary of ultaviolet absorption$^{(\text{exp.})}$, fluorescence$^{(\text{exp.})}$, electrochemical reduction potential$^{(\text{exp.})}$, ionization potential$^{(\text{calc.})}$, and electron affinities for **1** and **4** [55].

	UV		**Flourescence**		**$E_{1/2}$**	**IP**	**EA** [56]
	λ_{max} [nm]	$\epsilon(\times 10^4)$ [—]	$\lambda_{excitation}$ [nm]	$\lambda_{emission}$ [nm]	[V]	[eV]	[eV]
1	196	7.8	247, 286	421	−2.23	8.5	0.50±0.10
	220	5.4			−2.84	7.7±0.1 [56, 57]	
	251	7.8			−1.87		
	286	4.2			−2.47		
4	200	2.3	261, 297	431	−2.38	7.71	n.r.
	226	1.6			−2.93		
	260	2.3					
	295	1.4					

n.r. = not reported

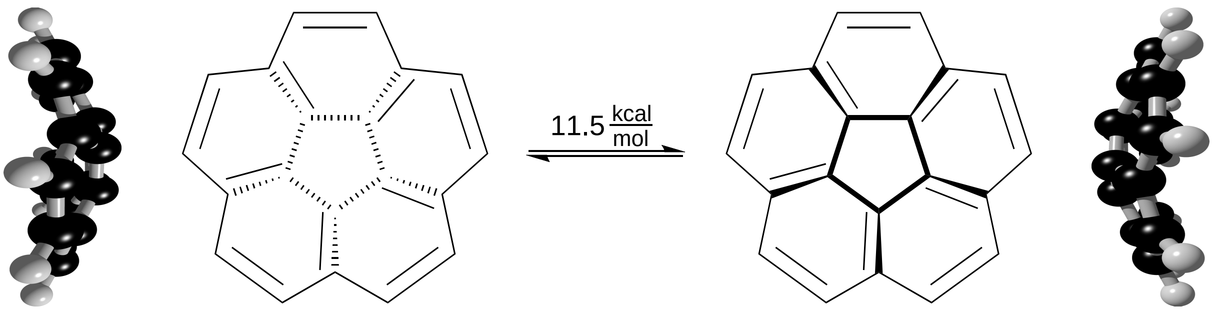

Figure 1.4.: With an activation energy of 11.5 kcal/mol **1** shows a rapid bowl-to-bowl inversion in the gas phase.

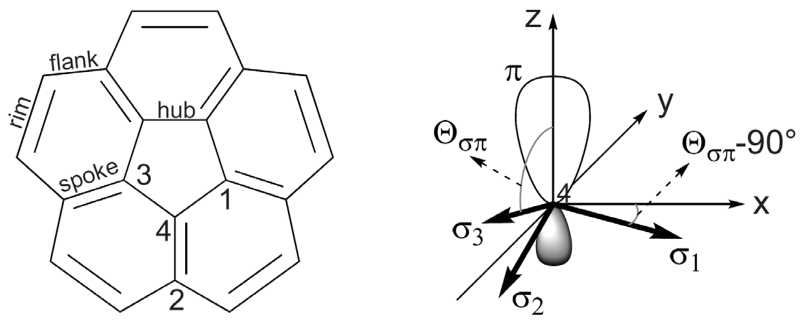

Figure 1.5.: Bond lengths in **1** differ for the hub, spoke, flank, and rim. The five-membered carbon ring surrounded by six-membered carbon rings give rise to a distorted sp^2 hybridized system. Having carbon (4) in the middle, the three σ bonds (sp^2 hybridized orbitals) point towards the carbons (1), (2), and (3). If the π orbital (defining the z-axis) shows the same angle towards every σ bond we can define a π-orbital axis vector (between the x-y plane and the σ bonds) ($\Theta_p = 0$ for graphene, $\Theta_p = 12.4$ for C$_{60}$, and $\Theta_p = 8.9$ for **1**) [58, 59].

Table 1.2.: Comparison of bowl-depth, bowl-to-bowl inversion barrier, and dipole moment of corannulene derivatives; (∼) indicating a wave-like inversion, and (−) a flat inversion.

Compound	Bowl depth [Å]	Bowl-to-bowl inversion barrier [kcal/mol]	*POAV* [°]	Dipolemoment [D]
1	0.875(2) [40]	11.5±0.6 [53]	8.9	2.1 [60, 61]
3	0.843 [62]	n.r.	n.r.	n.r.
4	0.8498 [62, 63]	8.7 [63]	n.r.	n.r.
6	1.065(exp.) [64]	28.8 [65]	8.91 [66]	3.06 [67]
	1.060 (calc.) [64]	29.8 [68]	9.83 [66]	
			11.15 [66]	
7*	2.429 [69]	79.8 (∼) [70]	n.r.	n.r.
		116.3 (−) [70]		
8*	2.264 [70]	124.3 (∼) [70]	n.r.	n.r.
		134.3 (−) [70]		

* The bowl-depth of **7** and **8** was determined to be the distance between two planes representing the bottom and rim of the bowls, respectively. n.r. = not reported

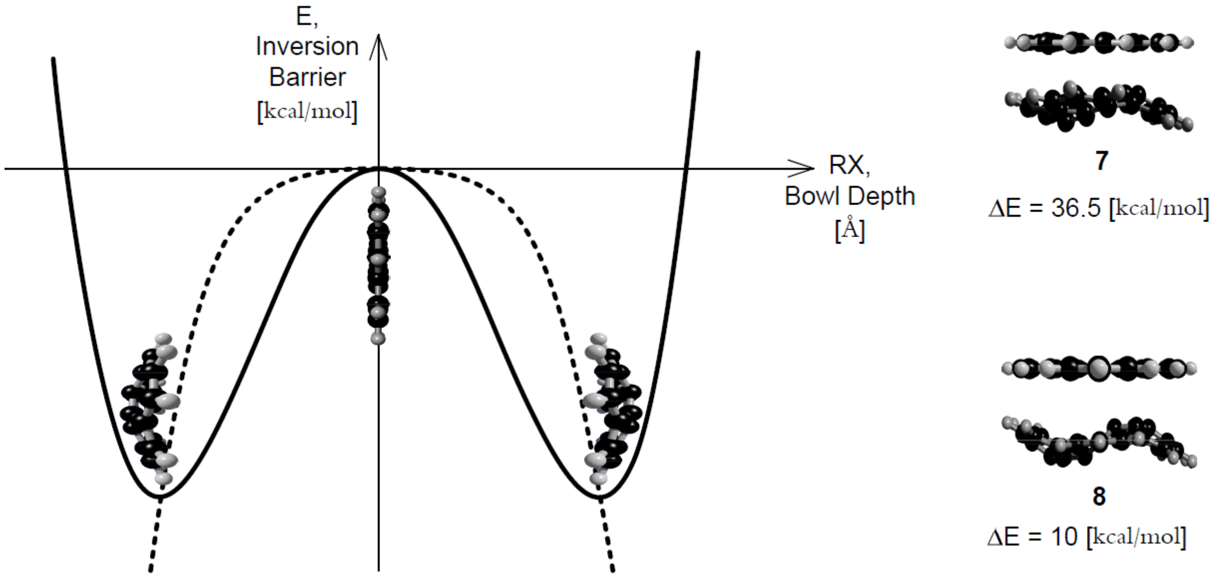

Figure 1.6.: Left: Bowl-to-bowl inversion barrier vs. bowl-depth, and reaction coordinate *RX*; **Right:** Larger, deeper bowls prefer a wave-like inversion instead of a flat transition state. Wave inversion of **7** is favoured by $36.5\,\mathrm{kcal/mol}$ relative to the flat inverstion.

1.2.2. Symmetry Aspects

Symmetry groups in the Euclidean plane can be classified as discrete and non-discrete; the discrete ones further divided into symmetry without and with translational-symmetry. Groups lacking translational symmetry are the cyclic group C_n (with $n = 1, 2, \dots$), which indicate symmetry of rotations of multiples of $360°/n$ (written as C_1, C_2, C_3, C_4, C_5, …, C_n), and the axial-symmetry groups C_{nv} or C_{nh} which contain C_n rotational-symmetry together with n mirror axes through the center (Diedergruppen or the dihedral groups, written as D_1, D_2, …, D_n) (Appendix A3.1). Groups with collinear translational symmetry are the seven so-called Frieze groups (Appendix A3.2). Groups with a minimum of two independent translations give the distinct 17 crystallographic plane groups (Appendix A3.3) [71, 72].

Corannulene's fivefold symmetric structure (Fig. 1.7) is incompatible with all 17 plane crystallographic groups. To explain its arrangement on a surface, one must look deeper into geometrical studies of fivefold symmetric structures, such as pentagons and pentagonal stars, which were already contemplated by A. Dürer and J. Kepler (Fig. 1.8 and Fig. 1.9, respectively) [73, 74].

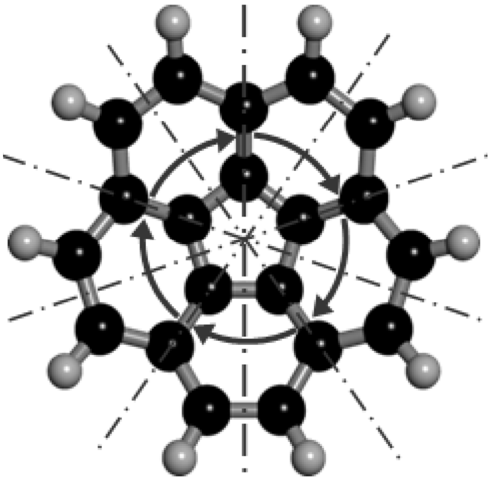

Figure 1.7.: The fivefold symmetry of corannulene

It was thought to be impossible to tile a plane in a fivefold symmetric pattern; however, Sir R. Penrose discovered in 1974 an aperiodic fivefold symmetric tiling with four shapes (pentagons, pentagrams (five-pointed stars), "boats" (3/5 of a star), and rhombi, Fig. 1.10) [75]. Later, he reduced the needed tiles to two: either "darts" and "kites" or two incongruent rhombi. A fivefold icosahedral symmetric quasicrystal was found by D. Shechtman[1] in a rapidly cooled aluminium alloy in 1984 [76, 77]. In 2013 the group of Widdra reported a quasicrystalline structure formation on a Pt(111) surface [78].

---

[1] Nobel Prize in Chemistry 2011 for "the discovery of quasicrystals". www.nobelprize.org

Physical and computational modeling studies have been used to characterize the potential packing of pentagons on a *2D* surface. Hard pentagons on a vibrating table (Fig. 1.11) show random hexagonal order [79], representing the low density rotatory phase that **4** exhibitsin part on Cu(111) [80]. Experiments with pentagons on an blowing air table (Fig. 1.11) led to rows of pentagons oriented in one direction with neighbouring rows oriented into the opposite direction [81], which is the closest possible *2D* packing for pentagons. Monte-Carlo studies for hard pentagons also show the same results [82]. These packings are observed for **3** on Au(11 12 12) and **4** on Cu(111) [80, 83–85].

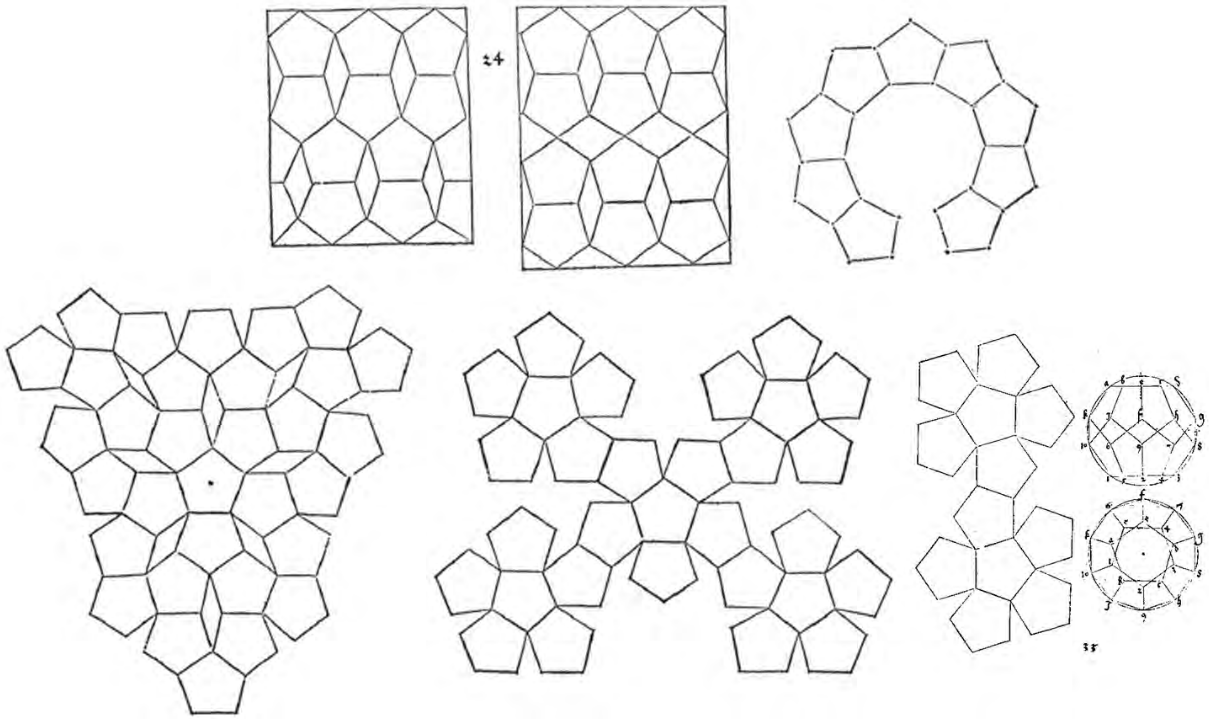

Figure 1.8.: Studies from A. Dürer of pentagonal and star shapes [73].

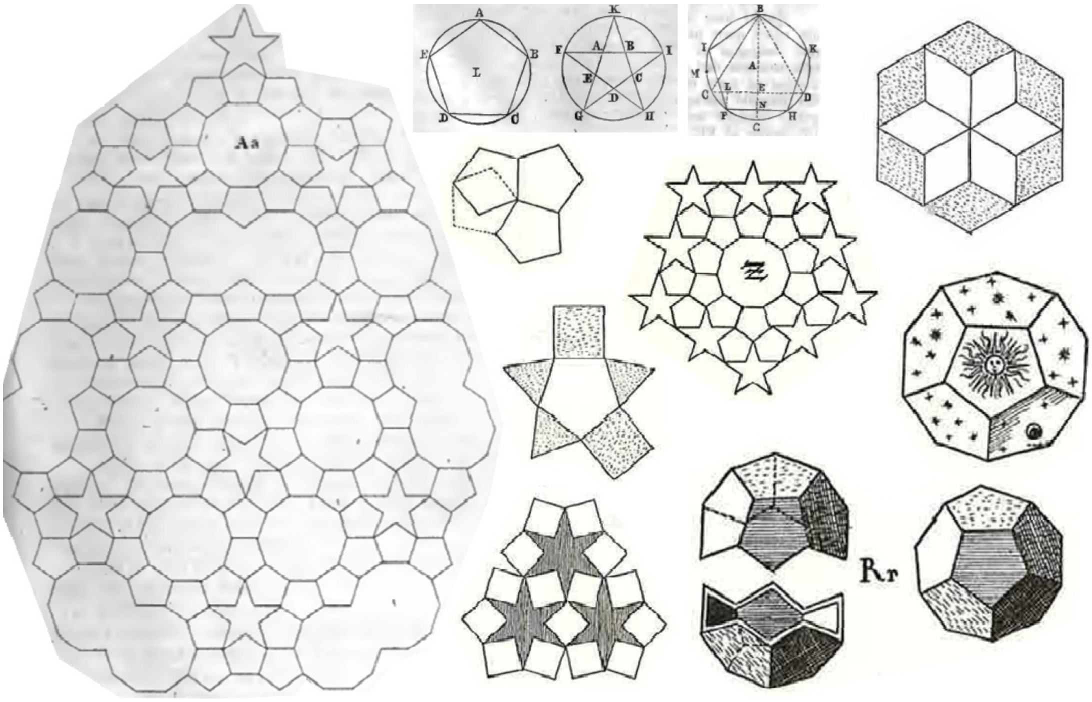

Figure 1.9.: Studies from J. Kepler of pentagonal and star shapes [74].

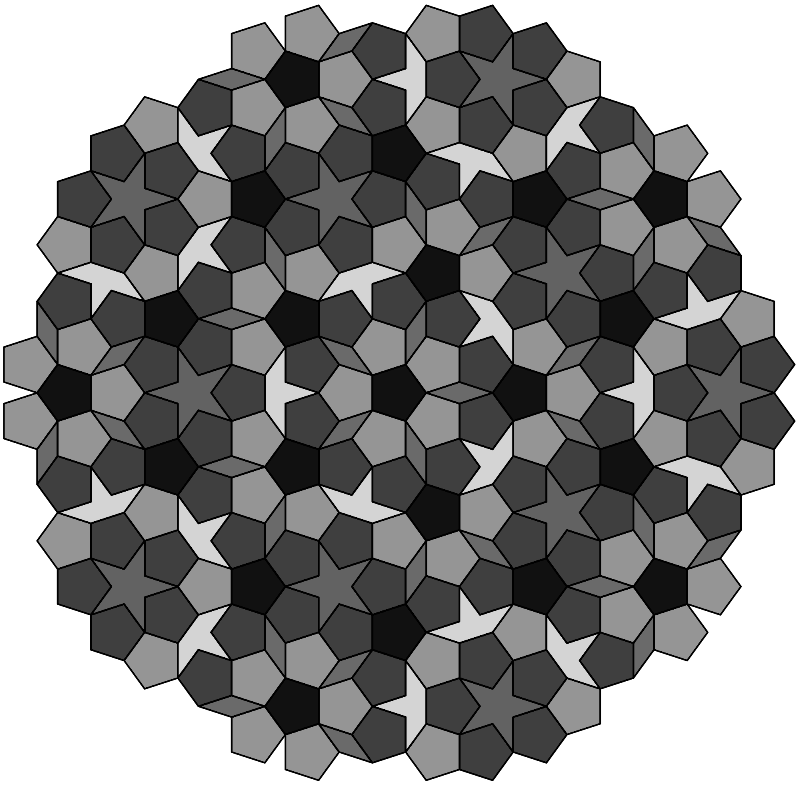

Figure 1.10.: Penrose-tiling: Tiling a plane with four specific tiles resulting in an aperiodic fivefold symmetric tiling of a plane.

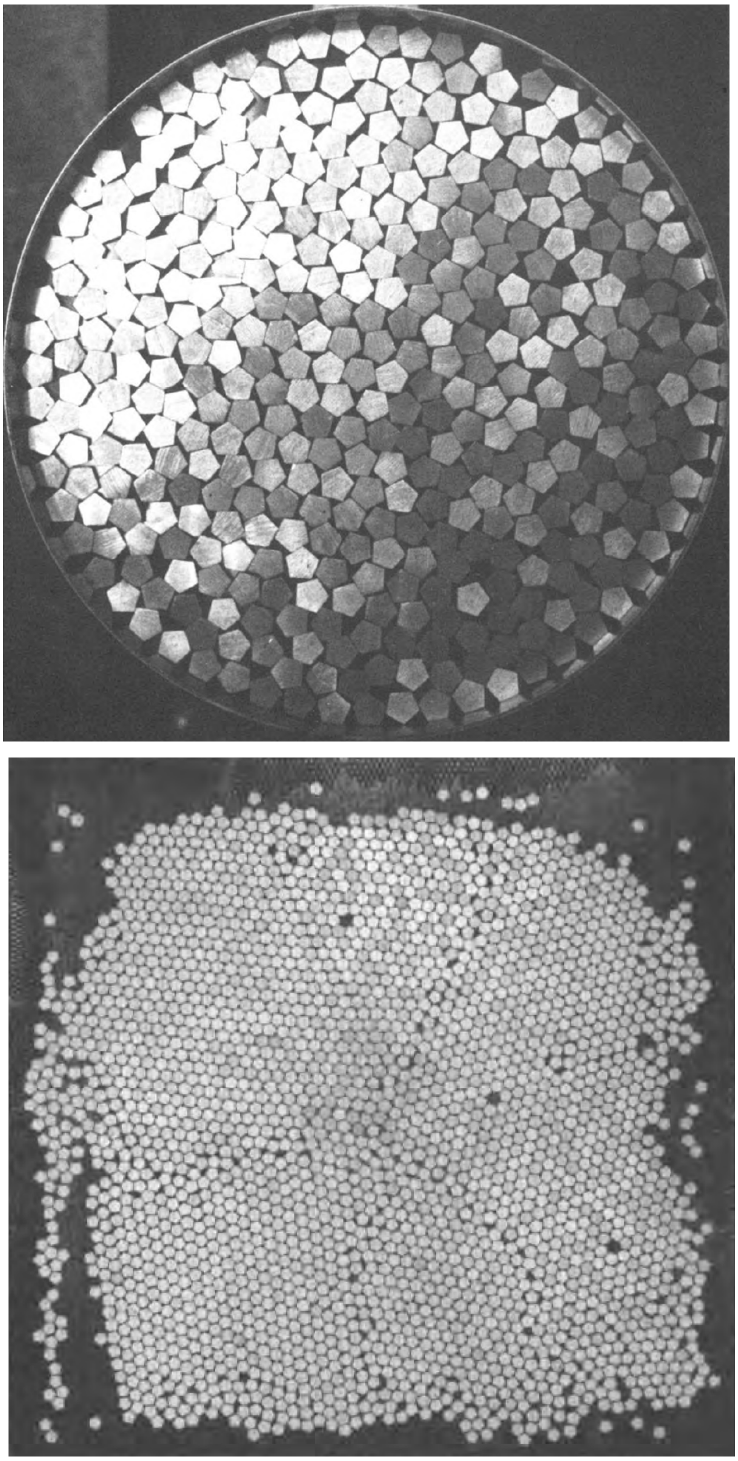

Figure 1.11.: **Upper:** Snapshot of a configuration formed by "annealing" a high-density "liquid" of small aluminium pentagons. This configuration was obtained by gradually increasing the density of pentagons in a vibrating-shake-table apparatus (reprinted with permission from [79], Copyright 1985 by the American Physical Society). **Lower:** An experimental crystal of pentagons on the blowing air table (Reproduced with permission from [81], Copyright 1995 by IOP Publishing. All rights reserved.).

2. Methods & Materials

This chapter introduces the methods used in this thesis, beginning with the instrumentation and giving an overview about the theoretical background.

2.1. Methods

All experiments were performed in the group for Molecular Surface Science, Laboratory for Nanoscale Materials Science at Empa, Swiss Federal Laboratories for Materials Science and Technology.

2.1.1. Ultrahigh vacuum systems

Surface analysis techniques are typically carried out in a vacuum because the electrons and ions that are used to probe the sample would be otherwise scattered by molecules in the gas phase. However, there are efforts to operate these techniques at "high" (standard) pressure. Experiments under ultrahigh vacuum (*UHV*) conditions allows one to control and study the influence of the molecular and atomic ambient on the surface under investigation. A clean, uncontaminated surface can be kept only in *UHV* ($< 1 \cdot 10^{-9}$ mbar) for sufficient time. Even at $1 \cdot 10^{-6}$ mbar a surface gets covered by one monolayer of adsorbed (undesired) species within 1 s (all particles stick upon collision, sticking coefficient 1 (Equ. 2.1)) [86] [87].

$$Z_A = \frac{p}{(2\pi mkT)^{1/2}} \tag{2.1}$$

with the impingement rate Z_A, the pressure p, the mass m, the Boltzman constant k, and the temperatere T.

For the experimental work of this thesis three *UHV* systems were used. The simplest one in terms of system complexity and attached components was a commercial Omicron variable temperature scanning tunneling microscope (*VT-STM*) (Fig. 2.1). The base pressure in this system was $< 5 \cdot 10^{-10}$ mbar.

The *VT-STM* was equipped with standard sample cleaning facilities (sputter gun, temperature-controlled sample holder), a sample manipulator, double evaporation cell (Knudsen cell), the scanning tunneling microscope, and a Prisma quadrupole mass spectrometer (*QMS200*, Pfeiffer Vacuum).

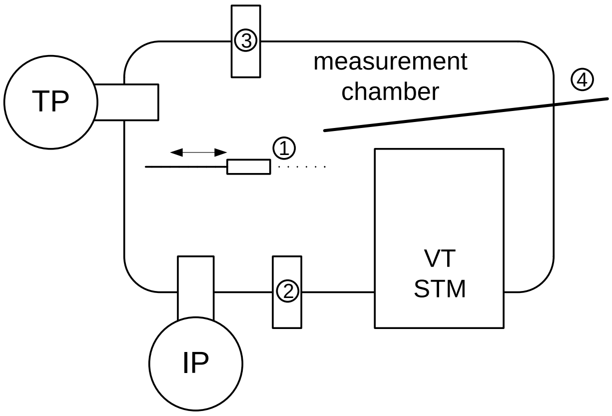

Figure 2.1.: Scheme of the *VT-STM* system (side view): ① sample manipulator, ② sputter gun, ③ evaporation cell, ④ transfer bar for moving the sample from the Manipulator to the *STM* and back. The measurement chamber was pumped via a turbomolecular pump (*TP*) and a ion pump (*IP*).

Some of the work was also done at the Electron Spectroscopy for Chemical Analysis (*ESCA*) system (Fig. 2.2), which was used to perform the photoelectron spectroscopy (*PES*) experiments. The base pressure in this system was below $2 \cdot 10^{-10}$ mbar. The system based on a commercial Physical Electronics ESCA was equipped with an electron energy analyzer (10-360) with AugerScan by RBD Enterprises as operating software, a Perkin Elmer dual anode Mg / Al X-Ray source (04-500) for X-ray photoelectron spectroscopy (*XPS*) measurements, a SPECS UVS 10/35 helium discharge lamp as ultraviolet (*UV*) radiation source for the ultraviolet photoelectron spectroscopy (*UPS*) measurements, a HIDEN quadrupole HAL 511/3F mass spectrometer (*MS*) for the temperature programmed desorption (*TPD*) measurements, and a SpectraLEED from Omicron with a LaB_6 filament for the low energy electron diffraction (*LEED*) measurements.

The third experimental apparatus was the Reflection Adsorption Infrared Spectroscopy (*RAIRS*)-system (Fig. 2.3). The base pressure in that system was $< 5 \cdot 10^{-10}$ mbar. The system was equipped with an *STM* 150 Aarhus from SPECS and a load lock for sample storage. The custom-assembled chamber was equipped with a Fourier transform infrared spectroscopy (*FTIR*) VERTEX 70v from Bruker Optics with separate infrared (*IR*) detector, a hemispherical energy analyzer PHOIBOS 100/150 by SPECS, a dual anode Mg / Al X-Ray source, the *LEED* optics, and an *STM* Aarhus 150 from SPECS.

In the *VT-STM* and *ESCA* systems, a direct current sample heating and water cooled Knudsen-type sublimation cells were used for the deposition of molecules. At the *RAIRS* system the sample was heated via electron beam heating.

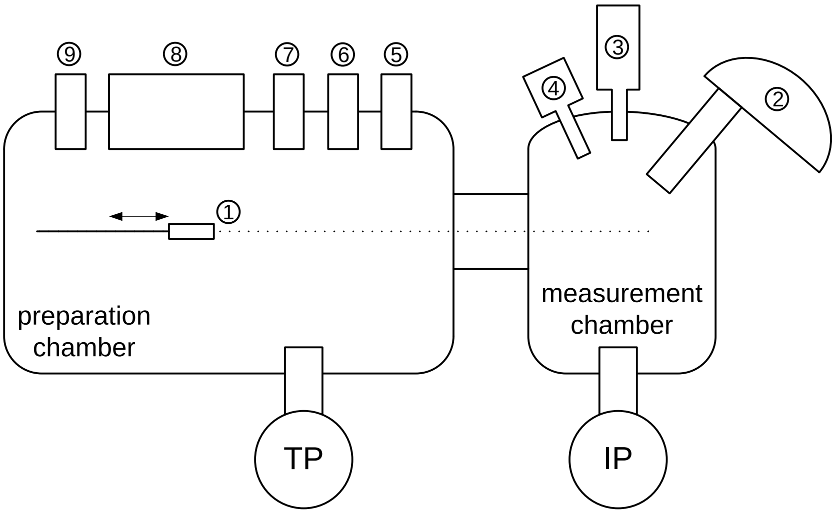

Figure 2.2.: Scheme of the *ESCA* system (side view): ① sample manipulator, ② electron analyzer, ③ X-Ray source, ④ *UV* light source, ⑤ and ⑥ evaporation cells, ⑦ sputter gun, ⑧ LEED optics, ⑨ mass spectrometer. The measurement chamber was pumped via *IP* and the preparation chamber via *TP*.

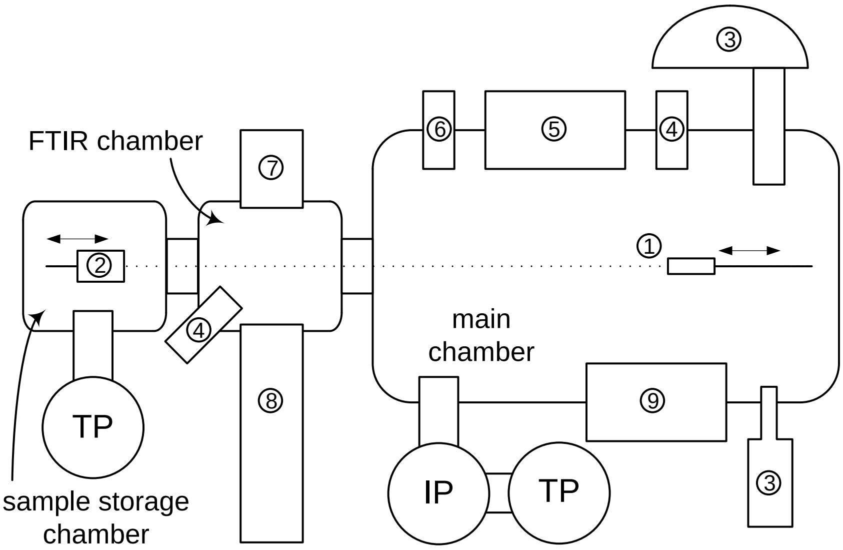

Figure 2.3.: Scheme of the *RAIRS* system (side view): ① sample manipulator, ② moveable sample storage, ③ electron analyzer, ④ evaporation cell, ⑤ Leed optics, ⑥ sputter gun, ⑦ *IR* detector, ⑧ *FTIR*-Interferometer. The measurement and *FTIR* chambers are pumped via *TP* and *IP*, and the sample storage chamber via *TP*.

2.1.2. Electron Spectroscopy for Chemical Analysis

The most widely used surface characterization methods are Electron Spectroscopy for Chemical Analysis (*ESCA*), also referred to as X-ray photoelectron spectroscopy (*XPS*), and ultraviolet photoelectron spectroscopy (*UPS*), which is similar to *XPS* but performed with a ultraviolet light source. *ESCA* is one of the most powerful tools for analyzing a surface-near region of only few nanometers depth. It can give information about all the elements (except H and He) present with a concentration larger than 0.1 atomic percent on the surface. *ESCA* is further described in [88–93].

The principle *ESCA* experiment is shown in Fig. 2.4. Around 1960, K. Siegbahn[1] and others developed this important technique, which is based on the photoelectric effect. The result of the measurement is a chemical analysis of the composition of the tested material.
In *ESCA*, the surface gets irradiated with photons in the X-ray (~ 0.01 nm to ~ 10 nm, corresponding to photon energies ~ 100 keV to ~ 100 eV) or *UV* (~ 10 nm to ~ 400 nm corresponding to photon energies ~ 3 eV to ~ 124 eV) energy range. The irradiated atoms at the surface emit (photo-)electrons after energy transfer from the photons to the core-level electrons. The emitted electrons are then counted and their energies measured. The energies of the emitted photoelectrons are related to the environment of their origin; the number is among others related to the concentration of the irradiated atoms in the sample.

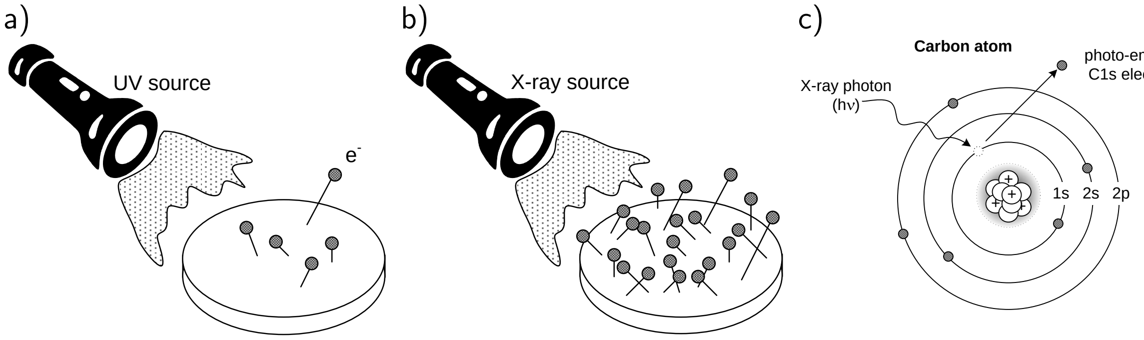

Figure 2.4.: a) and **b)** Sample surface irradiated by a photon source of sufficient high energy will emit electrons. **c)** An X-ray photon transfers enough energy to a core-level electron such that the electron leaves the atom.

The basic physics shown in Fig. 2.4 of this process can be described by Einsteins equation (2.2):

---

[1] Nobel Prize in Physics 1981 for "his contribution to the development of high-resolution electron spectroscopy" www.nobelprize.org

$$E_B = h\nu - E_K \tag{2.2}$$

with the binding energy of the electron to the atom E_B, the kinetic energy of the emitted electron measured in the spectrometer E_K, and the energy of the X-ray source $h\nu$.

The binding energy E_B of an electron in an atom is explained as follows: a negatively charged electron is attracted to the positively charged nucleus; the closer the electron is to the nucleus, the more strongly it is attracted. E_B varies with the atomic number and the electronic environment of the atom; covalently bound atoms alter the electron distribution and thus affect E_B. Weak interactions between atoms, e.g. hydrogen bonds, do not alter the electron distribution sufficiently to change the measured binding energy. The variations in binding energy associated with covalent or ionic bonds between atoms give insight into the chemical environment of the observed species and are called binding energy shifts or chemical shifts. In metals and semiconductors, additional energy (designated as the work function) for removing an electron from the highest occupied energy level (the Fermi level) must be taken into account. Irradiation of solids by X-rays can result in emission of Auger electrons (Fig. 2.5). A characteristic of Auger electrons is that their kinetic energy is independent of the irradiation energy.

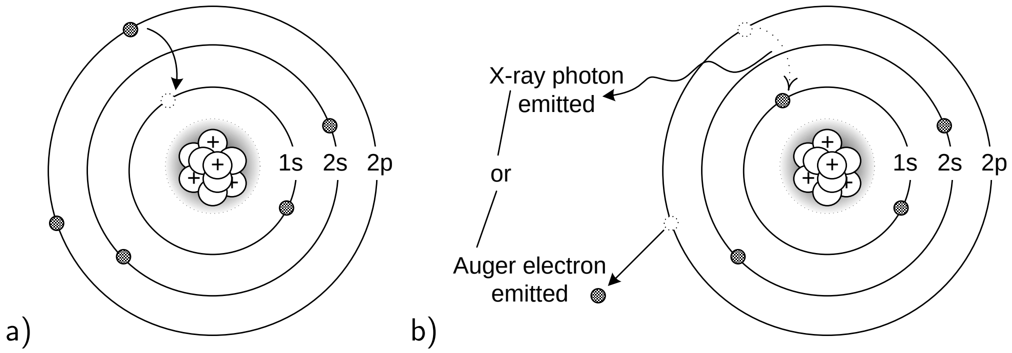

Figure 2.5.: After an X-ray photon confers its energy to a core-level electron, leading to photoemission, **a)** an electron drops from a higher energy level to the vacant core hole. **b)** As the electron drops to the lower energy level, the atom releases excess energy by emitting either an X-ray photon (X-ray fluorescence) or an electron from a higher energy level (Auger electron emission).

In this thesis *XPS*-studies are performed in order to ensure that a sample is clean, and for monolayer (*ML*) coverage determination of the compound under investigation. The measured *XPS* is compared to very precise *XPS* measurements of clean single crystals surfaces collected in the "*Handbook of X-ray photoelectron spectroscopy*" [94]. Common impurities appear as additional peaks in the spectra, such as oxygen appearing at $532\ \mathrm{eV}$ for the O1s binding energy.

With *UPS* the work function ϕ and the work function change $\Delta\phi$ of a sample under investigation can be determined. The work function (change) was determined in the following way (Fig. 2.6): 1) the Fermi level of the measured *UPS* spectra was aligned to $\mathrm{E_b} = 0\,\mathrm{eV}$. 2) A straight line of the slope of the decrease of the secondary electrons was calculated between 40 and 80 percent of the maximal intensity. This procedure was used in order to avoid the influence of a "bump" in the measured spectra, originating from an analyzer effect. 3) The intersection with the with the calculated line and the x-axis was determined. 4) The energy difference of the kinetic energy of the *UV* light source and the binding energy of the secondary electrons (point of intersection) was determined as the work function of the material. Repeating this procedure the work function change of the material plus adsorbate was determined.

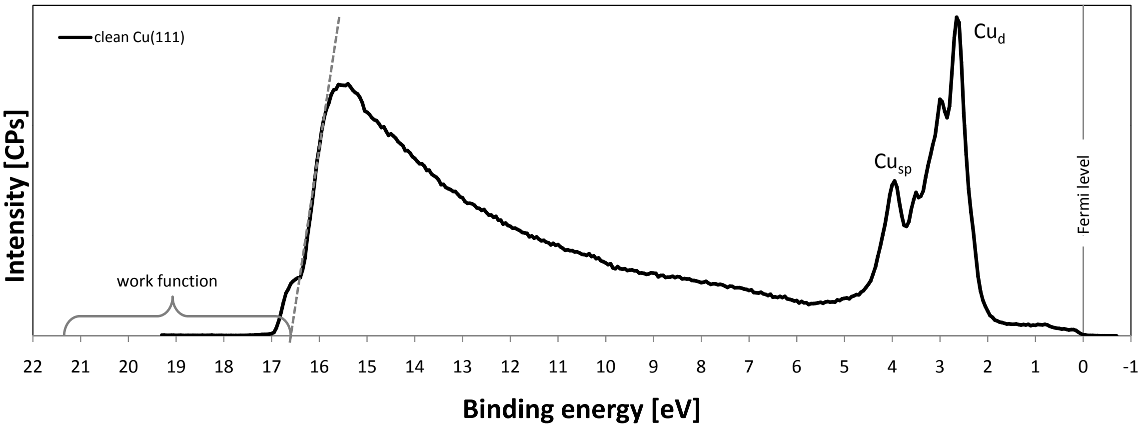

Figure 2.6.: *UPS* of Cu(111) with an electron emission angle of $10°$ showing the copper sp- and d bands and the cut-off of the secondary electrons. Procedure for determine the work function of a material: the measured *UPS* spectra is aligned to the Fermi level; a calculated intersection of the drop-off the secondary electrons with the x-axis is determined and this value subtracted from the kinetic energy of the *UV* light source.

The interfacial dipole moment, is related to the work function change $\Delta\phi$ via the Helmholtz formula (Equ. 2.3):

$$\Delta\phi = \frac{\mu_0\theta_0}{\epsilon\epsilon_0} \tag{2.3}$$

with μ_0 being the initial dipole moment ($1D = 3.34 \cdot 10^{-30}\,Asm$), ϵ_0 the vacuum permittivity ($\epsilon_0 = 8.85 \cdot 10^{-12}\,\frac{As}{Vm}$), θ_0 the initial coverage ($\frac{N}{m^2}$; N being the number of adsorbates), and ϵ the relative dielectric constant ($\epsilon \approx 1$). Since the Helmholtz equation does not take interactions between the molecular dipoles within the adsorbed layer into account, it is accurate only for low coverage of adsorbates on the surface. However, the interfacial dipole moment for low coverages can be estimated.

2.1.3. Low Energy Electron Diffraction

Low energy electron diffraction *LEED* is a long range surface sensitive technique. The average area that can be probed is rather large (up to $1\ \mathrm{mm}^2$) compared to other techniques. This gives important insight into the structural uniformity of layers of molecules adsorbed on surfaces. In the *LEED* optics the electron gun generates and accelerates the electrons towards the surface. For probing metal samples, kinetic energies of the incident electron beam between $10 \ldots 500\ \mathrm{eV}$ (having a mean free path of $4 \ldots 20$ Å in metals) are used. For organic molecules in a thin film, kinetic energies of the electron beam range from $10 \ldots 100\ \mathrm{eV}$, with corresponding wavelengths on the order of $0.1\ \mathrm{nm}$ and thus within the regime of typical interatomic distances [95]. From the sample lattice and adsorbed overlayer molecules, elastically back-scattered electrons are accelerated onto a fluorescent screen, which shows the superposition of the periodicity of the substrate and the periodicity of the adsorbate. This adlayer structure can be related to the layer underneath with a matrix notation described below in ”defining overlayer structures.” In Fig. 2.7 the principle arrangement of the *LEED* optic is shown.

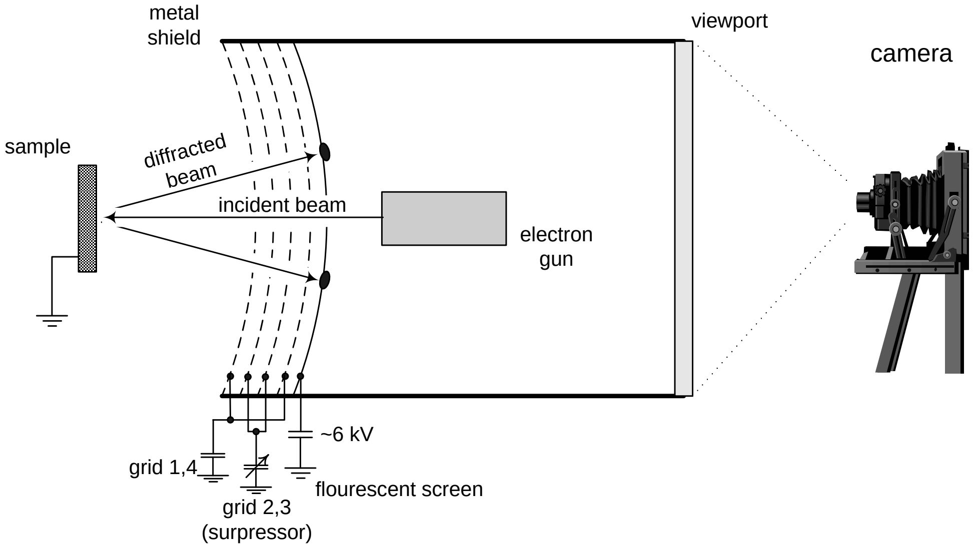

Figure 2.7.: Schematic of *LEED* optics. The electron gun generates an electron beam and accelerates the electrons towards the surface. Elastically back-scattered electrons are accelerated within the grids and focused onto a fluorescent screen.

The *LEED*-images were enhanced by color inversion, gamma correction, and contrast increase with IrfanView 4.25[2]. *LEED* pattern simulations are done with LEEDpat3[3]. The principle of *LEED* and applications are further described in other documents [96–98].

---

[2] `http://www.irfanview.com/`

[3] `http://www.fhi-berlin.mpg.de/KHsoftware/LEEDpat/index.html`

Defining overlayer structures:
Atomic and molecular adlayer structures adsorbed of singe crystal surfaces, e.g. Cu(111), can be described with the so called Wood notation. The overlayer structure with the vectors a_o and b_o, is related by multiples of the substrate unit vectors a_s and b_s in their respectable directions (Fig. 2.8). However, overlayer structures in which the angle between the two vectors are not identical with the substrate angle have to be described as e.g. $(\sqrt{3} \times \sqrt{3})$ R $30°$. This can be circumvented with the matrix notation, in which the relation between the substrate and the overlayer are described with a matrix **M** (Equ. 2.4). The matrix $(m_{11}\ m_{12},\ m_{21}\ m_{22})$ describes the adsorbed adlayer structure in multiples of substrate unit vectors (Equ. 2.5). In order to avoid different descriptions for the same adlayer, Merz *et al.* [99] suggested rules to find a master unit cell.

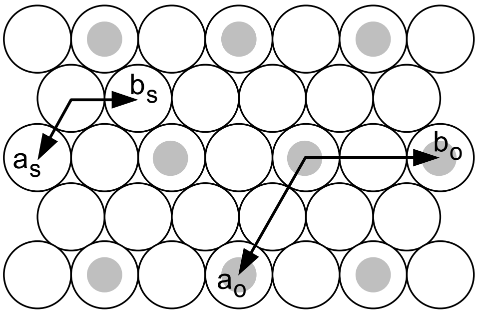

Figure 2.8.: Multiples of the substrate unit vectors (a_s, b_s) define an overlayer structure (a_o, b_o). Empty circles representing the substrate surface atoms, full circles overlayer adatoms or adsorbed molecules. Depicted is a (2 × 2) overlayer unit cell in the Wood notation or a (2 0, 0 2) unit cell with the Matrix notation.

$$\begin{aligned} a_o &= m_{11}a_s + m_{12}b_s \\ b_o &= m_{21}a_s + m_{22}b_s \end{aligned} \tag{2.4}$$

$$\begin{pmatrix} a_0 \\ b_0 \end{pmatrix} = \mathbf{M} \begin{pmatrix} a_s \\ b_s \end{pmatrix} \quad \text{, with} \quad \mathbf{M} = \begin{pmatrix} m_{11} & m_{12} \\ m_{21} & m_{22} \end{pmatrix} \tag{2.5}$$

The overlayer structure from Fig. 2.8 is described by a (2 0, 0 2) smallest possible unit cell (Equ. 2.6). An average area covered by each adsorbate can be determined with the cross product of the two vectors divided by the number of adsorbates within the unit cell (Equ. 2.7).

$$\begin{aligned} a_o &= 2 \cdot a_s + 0 \cdot b_s \\ b_o &= 0 \cdot a_s + 2 \cdot b_s \end{aligned} \quad \text{, with} \quad \mathbf{M} = \begin{pmatrix} 2 & 0 \\ 0 & 2 \end{pmatrix} \tag{2.6}$$

$$\begin{pmatrix} 2 \\ 0 \end{pmatrix} \times \begin{pmatrix} 0 \\ 2 \end{pmatrix} = 4 \tag{2.7}$$

2.1.4. Scanning Tunneling Microscopy

The tunnel effect between two metals was explained in 1961 by John Bardeen using a first order the time-dependent perturbation theory [100]. After the invention of the scanning tunneling microscope *STM* by Gerd Binnig and Heinrich Rohrer[4] [101–105], it quickly turned into one of the most important techniques in surface science.

Principle of measurement

Figure 2.9 shows a schematic *STM* set-up with its main parts - the piezo moving stage (x-y) of the tip and high precision electronics controlling the tunneling voltage and current, which can be related to the tip-sample distance d. A feedback-loop controls the distance (z-piezo) of the tip such that the tunneling current is kept constant. An atomically sharp tip scans line-by-line across the sample surface by variation of the voltage on the x-, y-piezos from about 5 Å away and measures the surface electron density. A lateral resolution of 0.1 Å and a vertical resolution of 0.01 Å can be achieved. One can operate the *STM* in two principle modes (Fig. 2.10): keeping the height of the tip constant or keeping the tunneling current constant. The first operational mode should be avoided if large elevation profile variations of the surface under investigation are present, which may lead to a crash of the *STM*-tip.

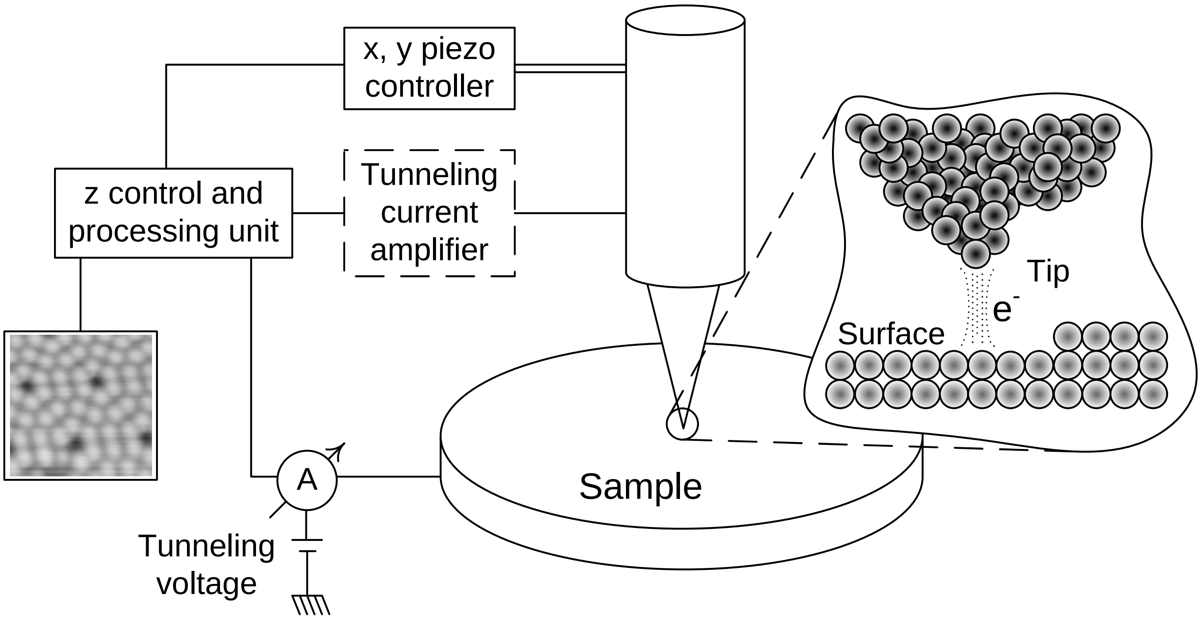

Figure 2.9.: Schematic view of an *STM*: Tunneling voltage V_t is applied between the tip and the surface, resulting in a tunnel current I_t.

---

[4] Nobel Prize in Physics 1986 for "their design of the scanning tunneling microscope." www.nobelprize.org

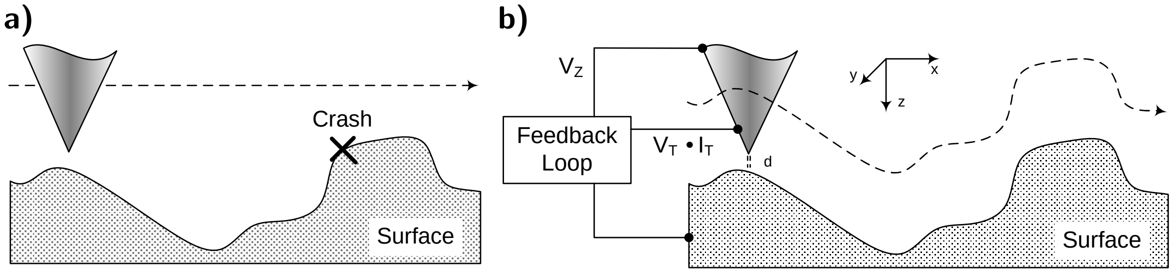

Figure 2.10.: **a)** Constant height mode: The variation of the tunneling current gets measured and the feedback loop of the z-piezo is off. There is a risk of crashing the tip into large structures. **b)** Constant current mode: The feedback loop controls the height of the tip by variation of the voltage for the z-piezo $V_z(V_x, V_y) \rightarrow z(x, y)$.

The basic physical process involved in *STM* can be best explained by simple one-dimensional tunneling (see textbooks like [106]). An electron wave function Ψ has to penetrate a potential barrier (e.g. vacuum gap). The Hamiltonian of the Schrödinger equation has two components (Equ. 2.8) for an electron encountering an infinitely thick potential barrier V_0:

$$\mathcal{H} = \begin{cases} -\frac{\hbar^2}{2m} \cdot \frac{d^2}{dx^2}\,, & x < 0, \text{ outside the barrier} \\ -\frac{\hbar^2}{2m} \cdot \frac{d^2}{dx^2} + V_0\,, & x > 0, \text{ inside the barrier} \end{cases} \tag{2.8}$$

The solution (Equ. 2.9) of these equations are:

$$\Psi(x) = \begin{cases} Ae^{ikx} + Be^{-ikx} & k = \sqrt{\frac{2mE}{\hbar^2}} \text{ outside the barrier} \\ Ce^{ik'x} + De^{-ik'x} & k = \sqrt{\frac{2m(E-V_0)}{\hbar^2}} \text{ inside the barrier} \end{cases} \tag{2.9}$$

The real part of the wave function inside the barrier decays exponentially. The classically forbidden penetration into the barrier is allowed in quantum mechanics (wave function is $\neq 0$, $E < V$). Therefore a finite probability exists to find the electron inside and behind the barrier. If the potential barrier (vacuum gap) is narrow enough there is a probability that the electron tunnels through it (Fig. 2.11). Two metals with a work function ϕ, separated by a certain distance and possessing a sufficient overlap of their Fermi level wave functions, could make quantum mechanical tunneling possible. With an applied potential difference a measurable tunnel current occurs. The order of magnitude of the tunneling current (I_t, Equ. 2.10) is given by the overlap of the two wave functions:

$$I_t \propto e^{-2\kappa d} \tag{2.10}$$

with $\kappa = \sqrt{\frac{2m\phi}{\hbar^2}}$ related to the local work function.

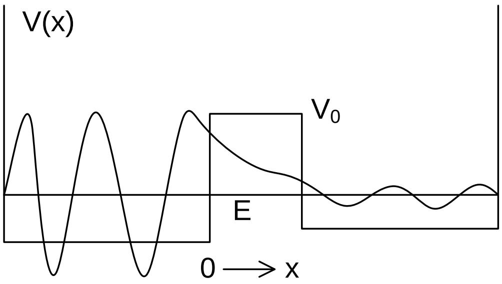

Figure 2.11.: Exponentially decaying wave function while tunneling through a barrier (vacuum gap).

Tunneling requires that there is an unoccupied energy level on the other side of the barrier for the electron to tunnel into. For that restriction, the tunneling current can be related to the density of empty or filled states in the sample. The current due to an applied voltage V depends on two factors: 1) the number of electrons between E_f and eV, and 2) the number among them which have corresponding free states to tunnel into. The more available states the larger the tunneling current. When V is positive, electrons in the tip tunnel into empty states in the sample; for a negative bias, electrons tunnel out of occupied states in the sample into the tip.

The theory of Tersoff and Hamann [107], which neglects the influence of the tip on the measurement provides information about the electronic structure of the sample. The tip is assumed to be a metal atom with a linear electronic density of states and spherically symmetric s-wave functions. On this assumption the tunneling current is expressed in Equ. 2.11.

$$I_t = \frac{32\pi^3}{\hbar}\frac{e^2 V \phi_0^2 D_t(E_f) R_t^2}{\kappa^4} e^{2\kappa R_t} \sum |\psi_\nu(r_0)|\, 2\delta(E_\nu - E_F) \tag{2.11}$$

C. Julian Chen extended this theory by taking complex tip-geometries into account [108, 109]. *STM*-image simulations can be obtained from density functional theory (*DFT*) calculations. The simulation at fixed current is an isosurface of the integrated local density of states. If the chosen energy window contains just a single molecular orbital Ψ, then it is simply an isosurface of $|\Psi|^2$. The value of the isosurface can be chosen to be the tip-sample distance. For further reading on technical details of *STM* please see [110, 111].

The program SCALA PRO 4.1 by OMICRON Vakuumphysik GmbH was used at the *VT-STM* and the "STM SPECS USB" program at the *RAIRS*-system for controlling and data storage. *STM* images are plane subtracted and flattened; if other modifications were made to the raw data image, it is stated in the caption. Image processing was done in WSxM 5.0 Develop 3.1 [112]. Unit cell analysis were done through Fourier transformation of the images (Appendix

A4 for details) in SPIP - The Scanning Probe Image Processor 3.004 by Image Metrologyd. A series of *STM*-images are Fourier transformed and two spots from the Fourier transformed images are choosen to determine the lengths and angles of the unit cell vectors. With this procedure, an average unit cell is created.

2.1.5. Fourier Transform Infrared Spectroscopy

Vibrational spectra from molecules adsorbed on the surface can be obtained via Fourier transform infrared spectroscopy *FTIR*. The vibration band is directly related to the environment of the adsorbed species. Absorption of infrared light by molecules causes a vibrational excitation of specific molecular sites. These vibrational excitation causes a dipole change. Only vibrations perpendicular to the metal surface can be measured by the *FTIR* instrument, since only the component of the light polarized in the plane of incidence is reflected from the surface at large incidence angles and only this light interacts with the vibrations of the adsorbed species which have a dynamic dipole moment perpendicular to the surface also known as the surface selection rules. Dipoles of parallel vibrations cancel with the image dipoles in the substrate. The most commonly used interferometer in *FTIR* is the Michelson type (Fig. 2.12), since it has an inherently increased signal-to-noise ratio (no use of monochromators, all light is detected) and the analysis is done via Fourier transformation [113, 114].

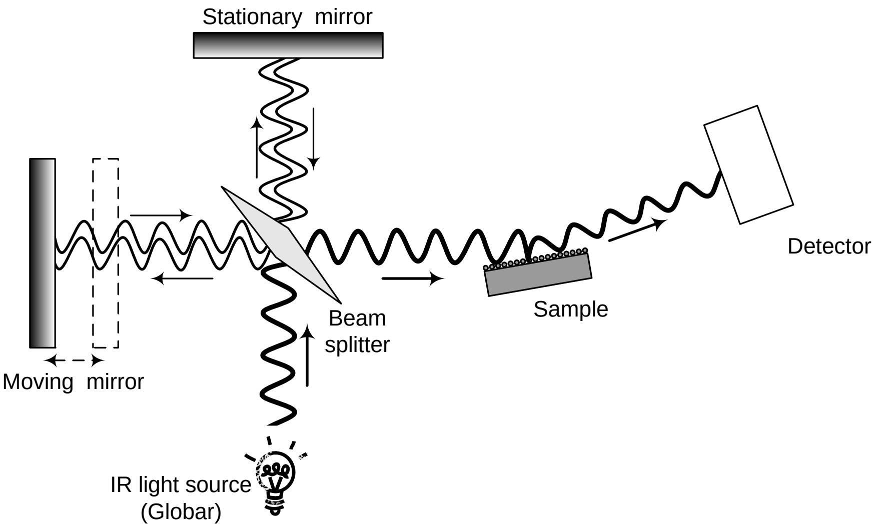

Figure 2.12.: Scheme of an FTIR-system: An infrared beam is split by a beam-splitter and recombined after one beam is modulated by a moving mirror. The recombined beam is directed to the sample, reflected by the sample, and the intensity difference of the absorbed part is recognized by a detector.

For the *FTIR* measurement, a VERTEX 70v instrument with separate *IR* detector from Bruker Optics and their OPUS 6.5 Spectroscopy Software was used to obtain the *RAIRS*. The acquired spectra (after surface modifications) is subtracted from the spectra taken on the clean sample. A baseline correction is then applied to all the spectra, yielding a linear background.

2.2. Material

2.2.1. General

Hat-shaped crystals (Cu(111), Cu(110), Cu(100), Ag(111), and Au(111)) purchased from MaTeck[5] (with a purity > 99.999 mass%, surface roughness < 0.03 µm and an accuracy of the orientation $< 0.1°$) were used in this thesis.
In the *ESCA* and *RAIRS* systems a type-K thermocouple was placed 3 mm into a borehole in the crystal. At the *VT-STM*, the thermocouple was placed on the manipulator nearby the sample-holder and was calibrated with another sample that had a thermocouple attached to it. Temperature calibration data for the *VT-STM* are shown in Appendix A1.

Standard cleaning procedures consisted of two 20 min periods of argon ion sputtering (sample current 3 µA and chamber pressure $1 \cdot 10^{-4}$ mbar) at the *VT-STM* each followed by 2 min of annealing at 600°C. The cleanliness was checked by *XPS*, *UPS*, *STM*, and *LEED*. For other cleaning procedures see Appendix A1. Each procedure had the same cleaning effect and, given an orientation accuracy of $< 0.1°$, terrace widths of > 2000 Å were achieved (see *STM*-images, *LEED*-image, and *XPS* measurement of a clean Cu(111) sample in Fig. 2.13).

The Siegel group at the University of Zurich provided the highly purified compounds of perdeutero-corannulene, pentaphenyl-corannulene, penta(phenylethyne)-corannulene, mono-indenocorannulene, and a corannulene-"graphene-flake" studied in this thesis. The Wu group at the National Cheng Kung University provided highly purified $C_{32}H_{12}$-buckybowl and $C_{38}H_{14}$-buckybowl. The synthesis of the molecules **2**, **5**, **6**, **7**, and **8** is briefly described in Appendix A2.

2.2.2. Other Molecules

Two molecules that have been studied did not form structures on none of the above mentioned surfaces that could be characterized. Probably these compounds did not stay intact during the deposition via sublimation.

---

[5] www.mateck.de

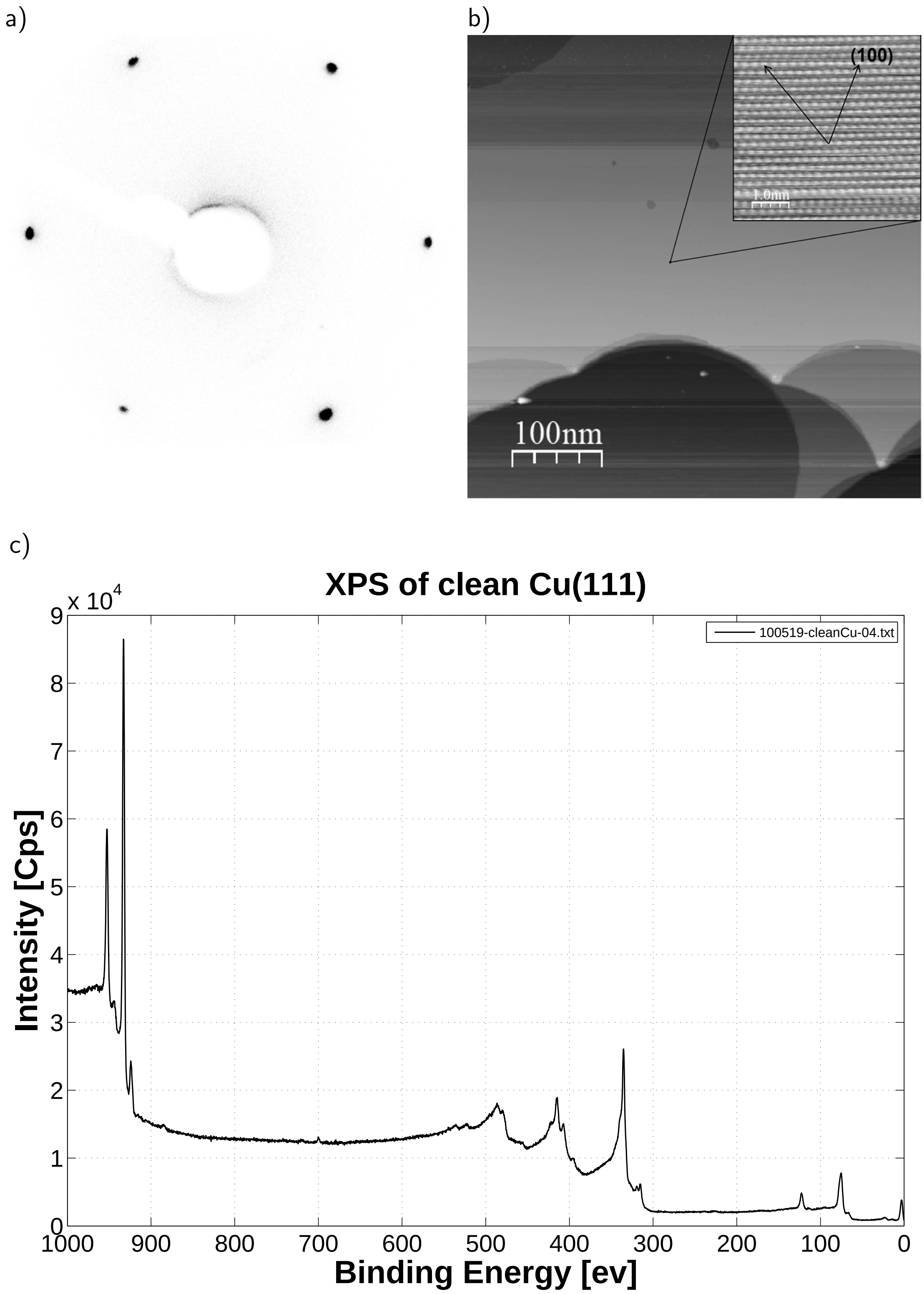

Figure 2.13.: Clean Cu(111): **a)** *LEED*-image at 72 eV, **b)** *STM*-image with atomic resolution (insert: -0.350 V, 0.291 nA) and large terrace (-0.571 V, 1.282 nA), **c)** *XPS*-measurement from $1000\ldots0$ eV binding energy with Cu $2p_{1/2}$, $2p_{3/2}$, $3s$, $3p$ -peaks (NO oxygen and carbon peaks)

Penta(phenylenthynyl)-corannulene (Fig. 2.15) was of interest, because the "arms" of these fivefold symmetric molecule are longer than those of **5** and chirality might be better expressed.

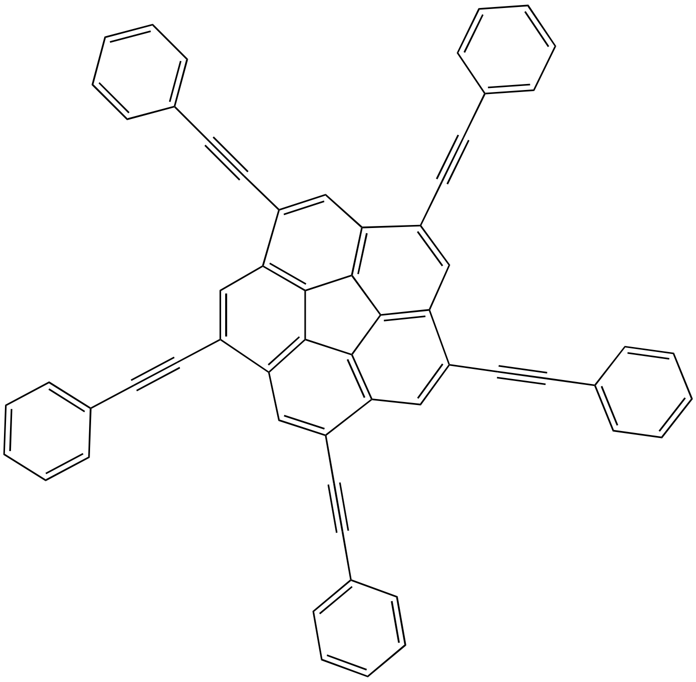

Figure 2.14.: Penta(phenylethynyl)-corannulene ($C_{60}H_{30}$)

To get deeper understanding of the covalent bonded C_{60} buckminsterfullerene onto (more and more studied [126]) graphene, a combined graphene-"flake" and **1** molecule has been synthesized by the Siegel group (Fig. 2.15) [127].

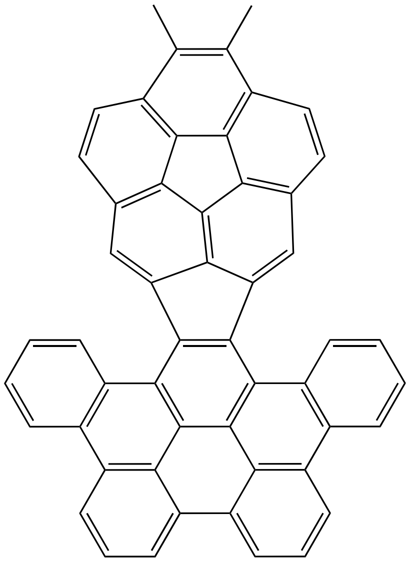

Figure 2.15.: Corannulene-graphene-flake ($C_{52}H_{26}$)

3. Previous studies

To place the results of this thesis work into context, a short summary of previous results of the self-assembly and the electronic properties of corannulene **1**, pentachloro-corannulene **3**, and pentamethyl-corannulene **4** is given.

3.1. Corannulene

Corannulene on Cu(110):

Two mirror domains of **1** with a unit cell of (4 1, −3 2) (Fig. 3.1) have been identified by *STM*. The alignment of the molecule was confirmed with *STM* simulations based on semi-empirical extended Hückel calculations, which indicated that the bowls open away from the surface (Fig. 3.2). From the asymmetric appearance of the molecule in high-resolution *STM*-images it was assumed that the molecule tilts upon adsorption on the surface. X-ray photoelectron diffraction experiments and single-scattering cluster calculations confirmed that the molecule tilts 6° to the surface normal and that the *hub* bond (the bond between the centered five-membered ring and a six-membered ring) is the adsorption site at the molecule. The two mirror domains result from the azimuthal angle of the unit cells with respect to the $[001]$ direction of the Cu(110) surface.

From *UPS* measurements a work function change of $-1.1\ \mathrm{eV}$ was observed for the monolayer coverage. A strong overlap between the highest occupied molecular orbital *HOMO*. . .*HOMO*-3 states of corannulene with the sp and d bands of the copper surface results in a strong interaction. Consequently, **1** is not thermally desorbed from the surface but undergoes decomposition above $500\ \mathrm{K}$ [60].

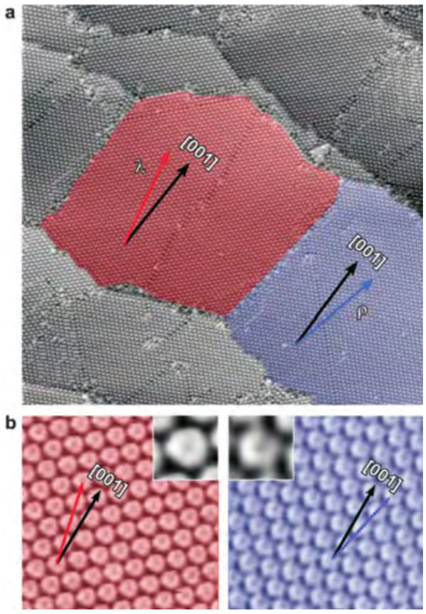

Figure 3.1.: **a)** *STM*-images of **1** reveal enantiomorphous λ (red) and ρ domains (blue); *RT*, 100×100 nm^2, U $= -1.6$ V, I $= 37$ pA. **b)** At higher magnification molecules are imaged as pentagonal doughnuts; 50 K, 9.6×9.6 nm^2, U $= -0.35$ V, I $= 66$ pA. Insets: 1.45×1.45 nm^2, U $= -0.51$ V, I $= 56$ pA (reprinted with permission from [60], Copyright ©2007 by WILEY-VCH Verlag GmbH & Co. KGaA, Weinheim).

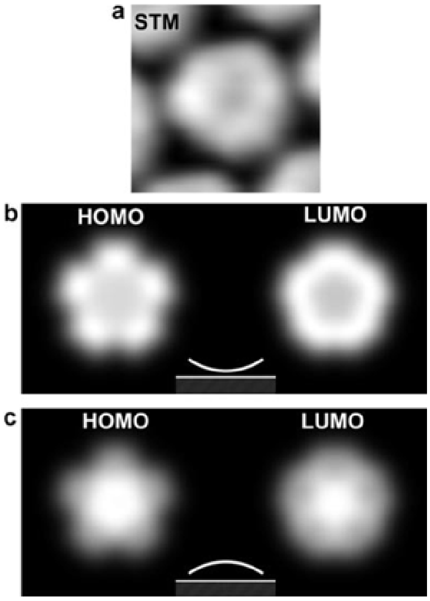

Figure 3.2.: Comparison of a high-resolution *STM*-image (1.45×1.45 nm^2, U $= 0.51$ V, I $= 56$ pA) of a single molecule in the close-packed monolayer with simulated *STM*-images based on extended Hückel calculations. the experimental appearance **(a)** agrees much better with the simulation for the bowl opening pointing away from the surface **(b)** than that with the bowl opening turned towards the surface **(c)** (reprinted with permission from [60], Copyright ©2007 by WILEY-VCH Verlag GmbH & Co. KGaA, Weinheim).

Corannulene on Cu(111):

By changing the surface symmetry of the substrate, namely from the twofold Cu(110) to the threefold Cu(111) surface, the adsorption and *2D* crystallization behavior of **1** also changes. The fivefold symmetric, bowl-shaped molecule crystallizes into a (4 0, 0 4) structure at room temperature. Similarly to its behavior on Cu(110), the molecule tilts upon adsorption to the Cu(111) surface. However, the buckybowl now tilts onto one of its six-membered rings which adsorbs parallel to the surface over an *fcc* or *hcp* threefold hollow sites of the Cu(111) lattice. *DFT* calculations confirmed the tilt that was inferred from the high-resolution low temperature (*LT*)-*STM*-images, which showed a clearly highlighted region of the doughnut-like **1** [128].

By lowering the temperature of the sample, a reversible two-dimensional phase transition is observed. Upon cooling below $250\ \mathrm{K}$, a transformation into a (4 0, 3 7) phase takes place, by which one of the two molecules within the unit cell is rotated by $30°$. This phase is stable upon cooling to $200\ \mathrm{K}$, at which a (4 2, 0 7) *LT* stripe phase is formed. Here a molecule is rotated by $20°$ with respect to the others in the unit cell. For both of the cooled phases, the two molecules within the unit cell are adsorbed on different sites, the hexagonal-closed-packed (*hcp*) and the face-centered-cubic (*fcc*) threefold hollow sites. This phase transition is found to be completely reversible with a small hysteresis (Fig. 3.3) [117]. All three phases were also identified in *LEED*-experiments [85].
The lattice density is increased by $14\ \%$ upon the first phase transition and stays constant for the second phase transition. This increase of local lattice contraction leads to areas with lower molecule density and can be imaged by *STM* as a "frozen 2D gas". Stabilizing of the (4 0, 3 7) phase can be achieved by additional sublimation of **1** molecules into it. Further phase transitions are blocked and can be unblocked by super-heating so that the *RT* phase is again generated [116]. Epitaxial bowl-in-bowl growth of the second layer with the same *LT* phase periodicity takes place exactly above the first layer of **1**, as indicated by *STM*-images (Fig. 3.4) [118]. From Dispersion-enabled Density Functional Theory (*DFT-D*) calculations it was suggested, that the second layer of **1** is adsorbed with the same orientation directly on top of the underlying **1** layer (Fig. 3.8).

Work function change measurements with *UPS* and dipole moment calculations with the Helmholz equation 2.3 for all the phases of corannulene on Cu(111) have been carried out. The calculated dipole moments were $8.6\ \mathrm{Debye}$ with a maximum work function change of $\Delta\phi_{max} = -1.5\,[eV]$ for the *RT* phase, $6.4\ \mathrm{D}$ with $\Delta\phi_{max} = -1.4\,[eV]$ for the (4 0, 3 7) phase, and $6.5\ \mathrm{D}$ with $\Delta\phi_{max} = -1.3\,[eV]$ for the *LT* phase [84].

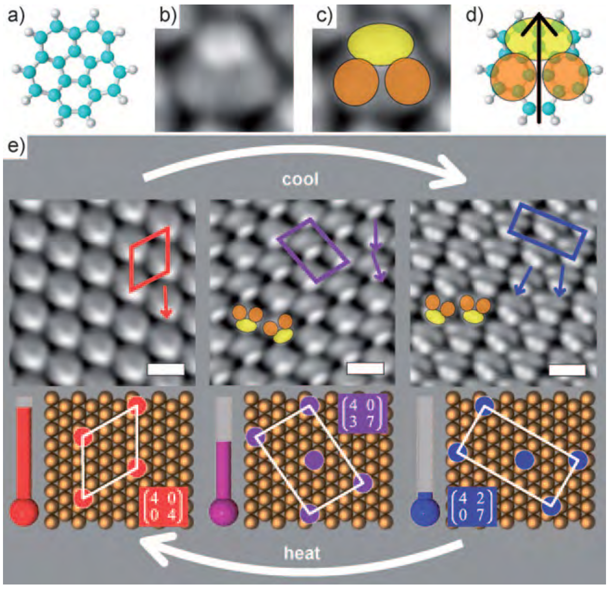

Figure 3.3.: Reversible phase transitions in molecular monolayers. **a)** Ball-and-stick model of corannulene. **b-d)** The correlation of the *STM* contrast at low temperatures with the molecular structure reveals a tilted adsorption geometry. The two top-most hexagonal rings (yellow) are imaged as bright protrusions, and the two middle rings (orange) appear with medium brightness. **e)** Top: *STM*-images of the three observed phases (averaged from 186, 64, and 17 different positions, respectively, from left to right). the unit cells and the molecular azimuthal orientations are indicated. Scale bars: $1\ \mathrm{nm}$. Bottom: The unit cells on the copper grid are shown with their matrix notation. Upon cooling, a (4 0, 0 4) lattice rearranges to give first a (4 0, 3 7) phase and then a (4 2, 0 7) phase. The original phase forms again upon heating (reprinted with permission from [117], Copyright ©2009 by WILEY-VCH Verlag GmbH & Co. KGaA, Weinheim).

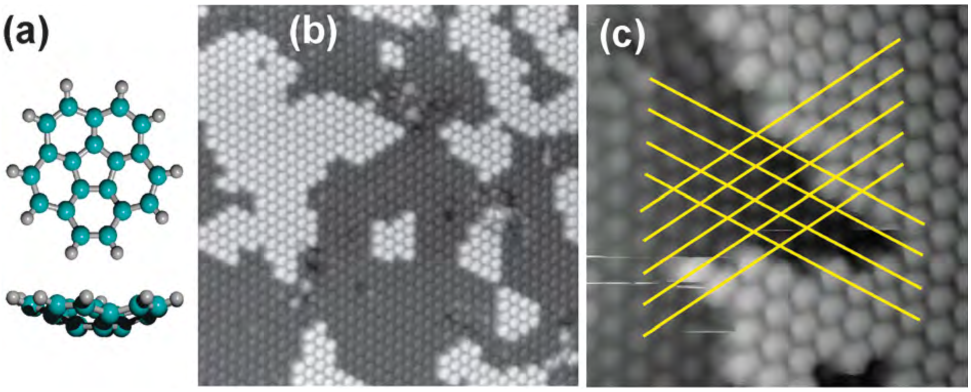

Figure 3.4.: **(a)** Ball-and-stick models for **1**. **(b,c)** *STM*-images of a half-filled 2nd layer of **1** ($28\ \mathrm{nm} \times 28\ \mathrm{nm}$ and $10\ \mathrm{nm} \times 10\ \mathrm{nm}$, $-1.74\ \mathrm{V}$, $24\ \mathrm{pm}$, $50\ \mathrm{K}$). The yellow lines along high-symmetry directions of the ad-lattice reveal "on-top" ad-sites in the second layer with identical lattice periodicity (reprinted with permission from [118], Copyright ©2011 by Royal Society of Chemistry).

3.2. Pentachloro-corannulene

Corannulene adsorbed on a surface avoids expressing its fivefold symmetry by tilting on the surface of both Cu(110) and Cu(111). By introducing bulky substituents at positions 1, 3, 5, 7, and 9 of the **1**-rim, the molecule maintains its fivefold symmetry while the tilt of the molecule is prohibited due to steric hindrance between the adsorbed molecule and the substrate surface. How does the new molecule, pentachloro-corannulene crystallize on the two-dimensional surface of a (111) single crystal? Since the Cl-atoms of **3** caused etching of the Cu(111) single crystal, a Au(111) single crystal was used instead. Because the herringbone reconstruction inherent in the topmost layer of wide Au(111) terraces influences the *2D* crystallization behavior of adsorbed molecules, a stepped Au(11 12 12) with small (111) terrace widths precluding extended herringbone reconstruction was used instead. *STM*-images of the monolayer coverage of **3** shows one of the structures predicted by the Monte-Carlo simulations, namely, the anti-parallel stripe structure (Fig. 3.5), with a suggested (8 0, 0 8) unit cell [80, 85]. In contrast to **1**, the appearance in the *STM*-image does not vary within the molecule. Therefore a parallel adsorption of the molecule can be assumed. Pentachloro-corannulene can be approximated as a hard pentagon and it behaves as such upon adsorption. As mentioned above, closed packed pentagonal structures have been identified in floating-air-table and shaking-table experiments (see section 1.2.2) and have been predicted in Monte-Carlo simulations [82].

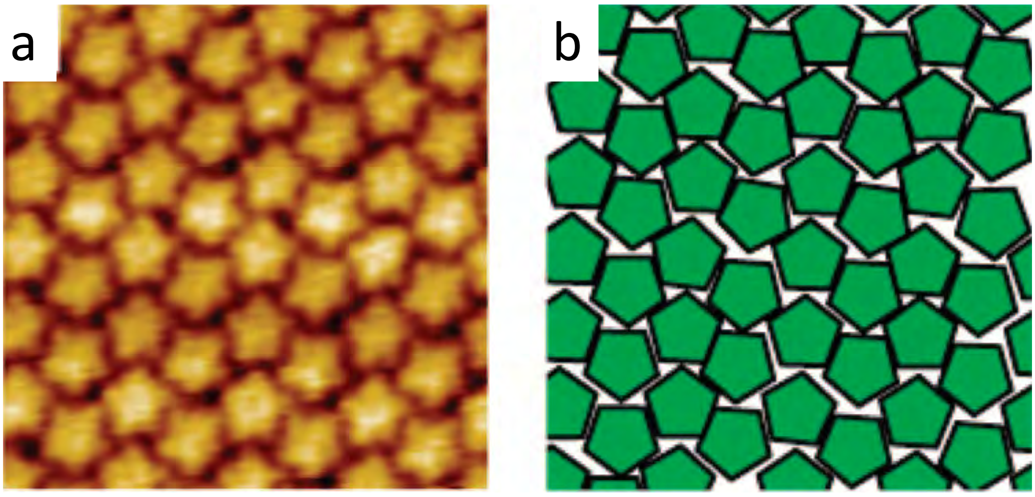

Figure 3.5.: a) *STM*-image ($8 \times 8\,\mathrm{nm}^2$) of **3** on Au(11 12 12) ($\mathrm{U} = -0.7\,\mathrm{V}$, $\mathrm{I} = 35\,\mathrm{pA}$, $\mathrm{T} = 76\,\mathrm{K}$). **b)** The alignment of the molecules as observed in the *STM*-images have been transferred directly into the cartoon shown in the right column (adapted from [80], Copyright ©2009 by American Chemical Society.").

3.3. Pentamethyl-corannulene

From *STM* experiments of **3** it was already seen that 1,3,5,7,9-penta-substituted derivatives of **1** molecules maintain their fivefold symmetry upon adsorption due to the steric hindrance between molecule and surface. By increasing the size of the functional groups, chiral recognition of the molecules may be observable in *STM* as well.

Two phases of pentamethyl-corannulene adsorbed at *RT* after cooling to $50\ \mathrm{K}$ are observed in *STM*. Similar to **3** on Au, an antiparallel stripe phase with a (5 2, 1 8) unit cell belonging to the *p2mg* plane group occurs (Fig. 3.6). This pattern is the closest possible packing for hard pentagons. A rotator phase with an averaged (5 3, 2 3) unit cell having a $\sim 10\ \%$ lower density is also found. A (6 3, -3 3) pattern for a 0.75 monolayer coverage was only observable via *LEED*, while a (11 3, -3 8) structure for the full monolayer could be observed in *STM*-experiments. By cooling the full monolayer the two *LT* phases are generated and vice versa. However, heating of the full monolayer structure to $375\ \mathrm{K}$ and subsequent cooling to *LT* results in a hole phase with a (5 -5, 5 10) unit cell in which molecules are packed in triplet-form, leaving a hole in the structure (Fig. 3.7). The formation of the hole phase could occur due to the maximization of the van der Waals forces between the molecules. Comparison of *DFT* and dispersion-corrected *DFT-D* calculations indicate that van der Waals forces between the molecules are important for allowing dense packing. Heating to *RT* again induces the *RT* phase. In the *RT* phase, one molecule covers 32.33 Cu(111) surface atoms, with three molecules fitting per (11 3, -3 8) unit cell. Also three molecules fit within the (5 -5, 5 10) hole phase, with a coverage of one molecule per 25 Cu(111) surface atoms. Only one molecule is present in the (6 3, -3 3)unit cell of the 0.75 monolayer coverage phase, with one molecules per 27 Cu(111) surface atoms. The two *LT* phases have similar density, with one molecule per 19 Cu(111) surface atoms for the antiparallel (5 2, 1 8) stripe phase and one molecule per 21 Cu(111) surface atoms for the (5 3, 2 3) rotator phase, and two and one molecule per unit cell, respectively [85, 129]. Epitaxial bowl-in-bowl growth of the second layer takes place exactly above the first layer of **4**, according to *STM*-images (Fig. 3.8). From *DFT-D* calculations it was suggested, that the second layer of **4** are rotated in order to place the methyl groups in a lowest energy configuration on top of the underlying **4** layer (Fig. 3.8a, b) [118].

Work function change measurements with *UPS* showed a total work function change of $-1.6\ \mathrm{eV}$, and calculations with the Helmholtz equation 2.3 yielded a dipole moment of $7.4\ \mathrm{D}$ for the *RT* (11 3, -3 8) phase [84].

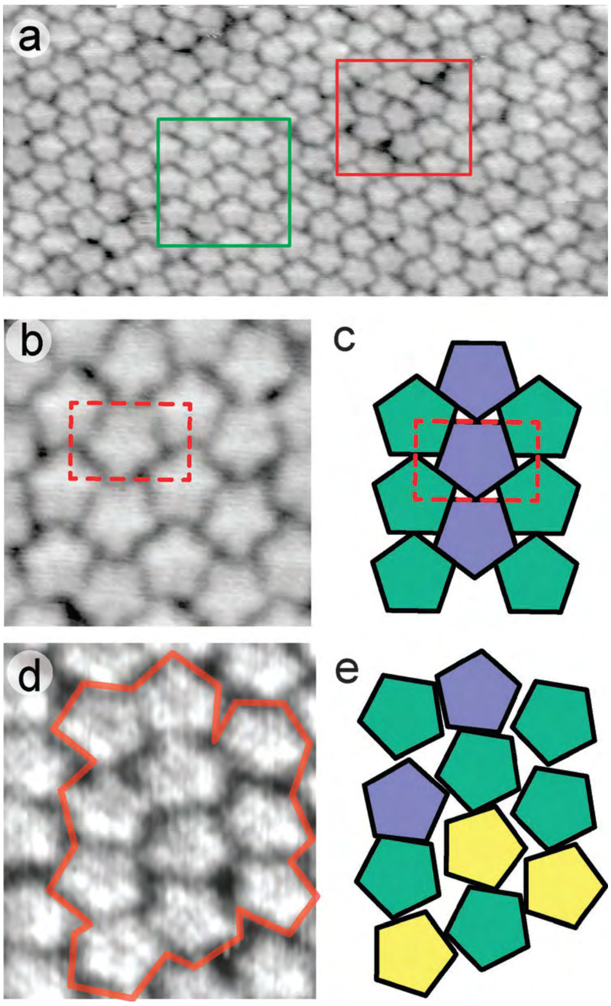

Figure 3.6.: *STM*-images and models for low temperature phases of **4**. **(a)** $20\ \mathrm{nm} \times 20\ \mathrm{nm}$, $\mathrm{U} = -1.452\ \mathrm{V}$, $\mathrm{I} = 428\ \mathrm{pA}$, $46\ \mathrm{K}$. The green rectangle shows a well-ordered area, while the red rectangle indicates a defect area. **(b)** Magnification of the ordered area in **(a)** $5\ \mathrm{nm} \times 5\ \mathrm{nm}$, $\mathrm{U} = -1.452\ \mathrm{V}$, $\mathrm{I} = 428\ \mathrm{pA}$, $46\ \mathrm{K}$. **(c)** Pentagon model for the ordered *LT* phase with antiparallel alignment. **(d)** *STM*-image of a rotator phase ($5.1\ \mathrm{nm} \times 5.7\ \mathrm{nm}$, $\mathrm{U} = -0.929\ \mathrm{V}$, $\mathrm{I} = 420\ \mathrm{pA}$, $46\ \mathrm{K}$). **(e)** Pentagon model for the rotator phase (corresponding molecules are framed in red in **(d)**). The same colors identify identical orientations (reprinted with permission from [129], Copyright ©2012 by Royal Society of Chemistry).

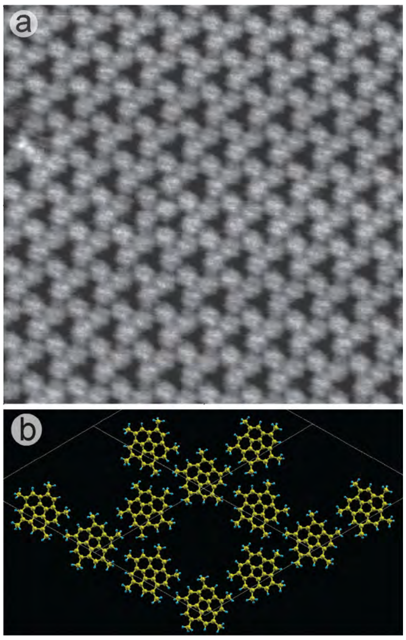

Figure 3.7.: **a)** The hole phase. The *STM*-image ($20\ \mathrm{nm} \times 20\ \mathrm{nm}$, $\mathrm{U} = -1.235\ \mathrm{V}$, $\mathrm{I} = 455\ \mathrm{pA}$) shows that the molecules form triplets as building blocks of the extended phase. **(b)** *DFT-D* modelling confirms the experimetally observed structure (reprinted with permission from [129], Copyright ©2012 by Royal Society of Chemistry).

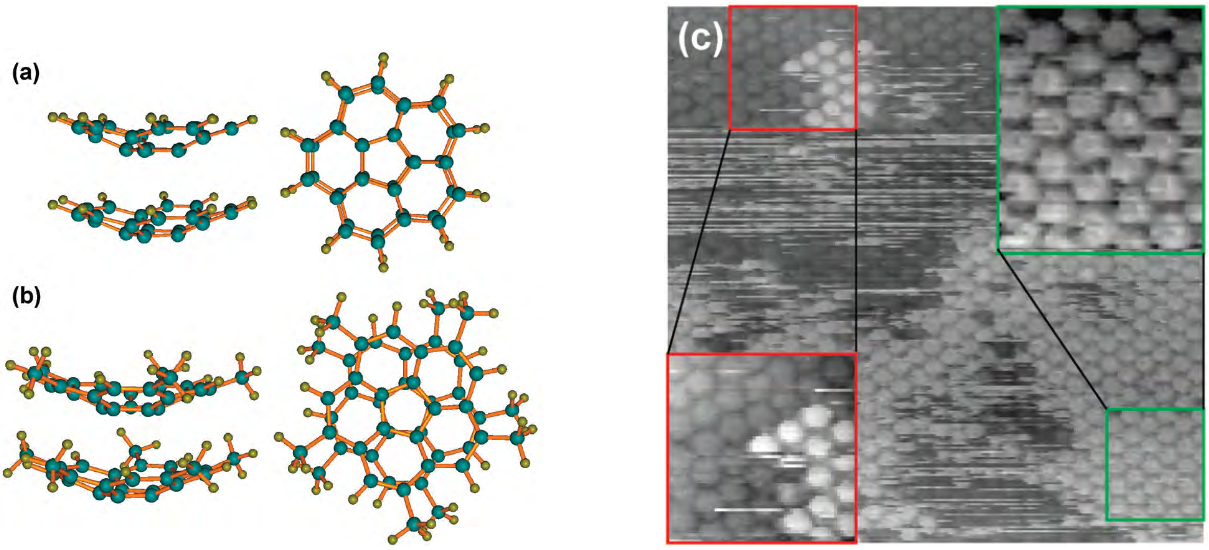

Figure 3.8.: **(a)** and **(b)** top and side view of the lowest energy configuration for pairs of **1** and **4** (adopted from [118], Copyright 2011 by Royal Society of Chemistry). (c) *STM*-image of a half-filled 2nd layer of **4** on **4** ($30\ \mathrm{nm} \times 30\ \mathrm{nm}$, $-1.61\ \mathrm{V}$, $83\ \mathrm{pA}$, $56\ \mathrm{K}$). The insets ($7\ \mathrm{nm} \times 7\ \mathrm{nm}$, red and $12\ \mathrm{nm} \times 12\ \mathrm{nm}$, green) have been directly magnified from the shown areas (adopted from [118], Copyright ©2011 by Royal Society of Chemistry).

3.4. Perdeutero-corannulene

Changing of the rim-substituents from hydrogen to deuterium leaves the electronic properties of the molecule untouched; the vibrations of the molecule on the other hand change. Do the masses of rim-substituents have an influence on the adsorption, self-assembly behavior, phase transitions and second layer growth of corannulene on Cu(111)?
To answer this question, perdeutero-corannulene molecules were investigated with *STM*. A cooled down perdeutero-corannulene monolayer, which was deposited onto the Cu(111) surface at room temperature is shown in the *LT-STM*-image in Fig. 3.9. The unit cell was determined to (4 0, 3 7), which is identical with the unit cell after the first phase transition of **1** on Cu(111) (Fig. 3.9 upper inset). The (4 0, 3 7) phase of **1** does only exist in a certain temperature regime, namely between $200 \dots 250\ \mathrm{K}$. A second phase transition as observed for **1** was not found in *STM*.

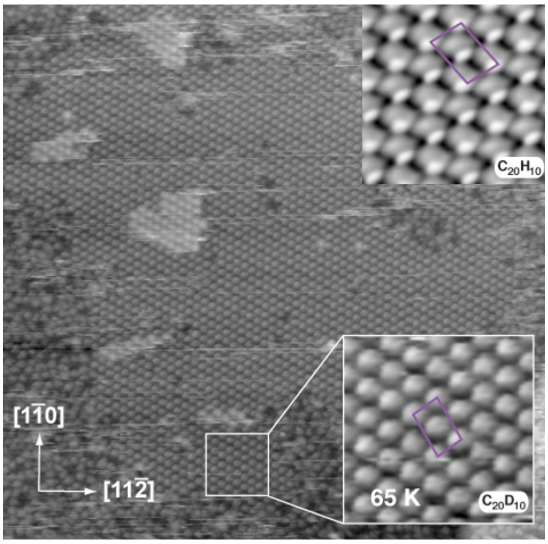

Figure 3.9.: *STM*-image of **2** on Cu(111) after cool down to $65\ \mathrm{K}$ ($60 \times 60\ \mathrm{nm}^2$, $-2\ \mathrm{V}$, $100\ \mathrm{pA}$). The insert on the top-right ($5 \times 5\ \mathrm{nm}^2$) and the magnified area show the (4 0, 3 7) phase of **1** and **2** on Cu(111), respectively.

By switching the rim-substituents from hydrogen to deuterium, a huge influence of isotopes in the phase transition behavior of **1** could be shown. The frequency change of the vibrational modes of **1** and **2** may be the explanation for this behavior. The difference in vibration might influence the mobility of the molecule on the surface and could be responsible that a second phase transition is prevented.

Further studies in order to confirm these preliminary results are described in chapter 4.

4. Perdeutero-corannulene: Isotope-effect?

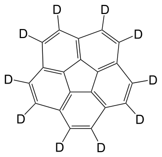

Further studies on the isotope-influence on *2D* crystallization and phase transition of perdeutero-corannulene on Cu(111) have been carried out with *STM*. The, so far not answered questions are: does the second layer adsorption of **2** proceed in the same bowl-in-bowl epitaxial growth as **1**; and what is the temperature of the phase transition?
Monolayer coverage of perdeutero-corannulene was obtained by sublimation at $383\,\mathrm{K}$ for $3.5\,\mathrm{min}$ onto Cu(111) held at room temperature; the same conditions were used for the studies of **1** on Cu(111).

In Fig. 4.1a, the room temperature monolayer is shown. The molecules crystallize after deposition at room temperature into a hexagonal (4 0, 0 4) unit cell. The high-resolution *STM*-image shows a highlighted part on one side of the molecule indicating a tilt upon adsorption. The arrow on top of the models indicating the part of the molecules which is protruding upwards. Figure 4.1b shows the monolayer after the phase transition, upon cooling the sample below a transition temperature of $230\,\mathrm{K}$. This reversible phase transition from the *RT*-phase to a (4 0, 3 7) phase is observed between $210\ldots230\,\mathrm{K}$. In this phase, the stripe-wise appearance in the *STM*-image is identical to that observed for **1**. It can be assumed that one of the two molecules within the (4 0, 3 7) unit cell is azimuthally rotated with an angle of $30°$; as shown in high-resolution *STM*-images of **1**.
Surprisingly and in contradiction to the previous studies, a second phase transition below a transition temperature of $200\,\mathrm{K}$ was observed which is shown in Fig. 4.1c. A reversible rearrangement leads to this stripe-wise structure with a (4 2, 0 7) unit cell, identical with the *LT* phase observed for **1**. Here one of the two molecules within the unit cell is rotated by $20°$.

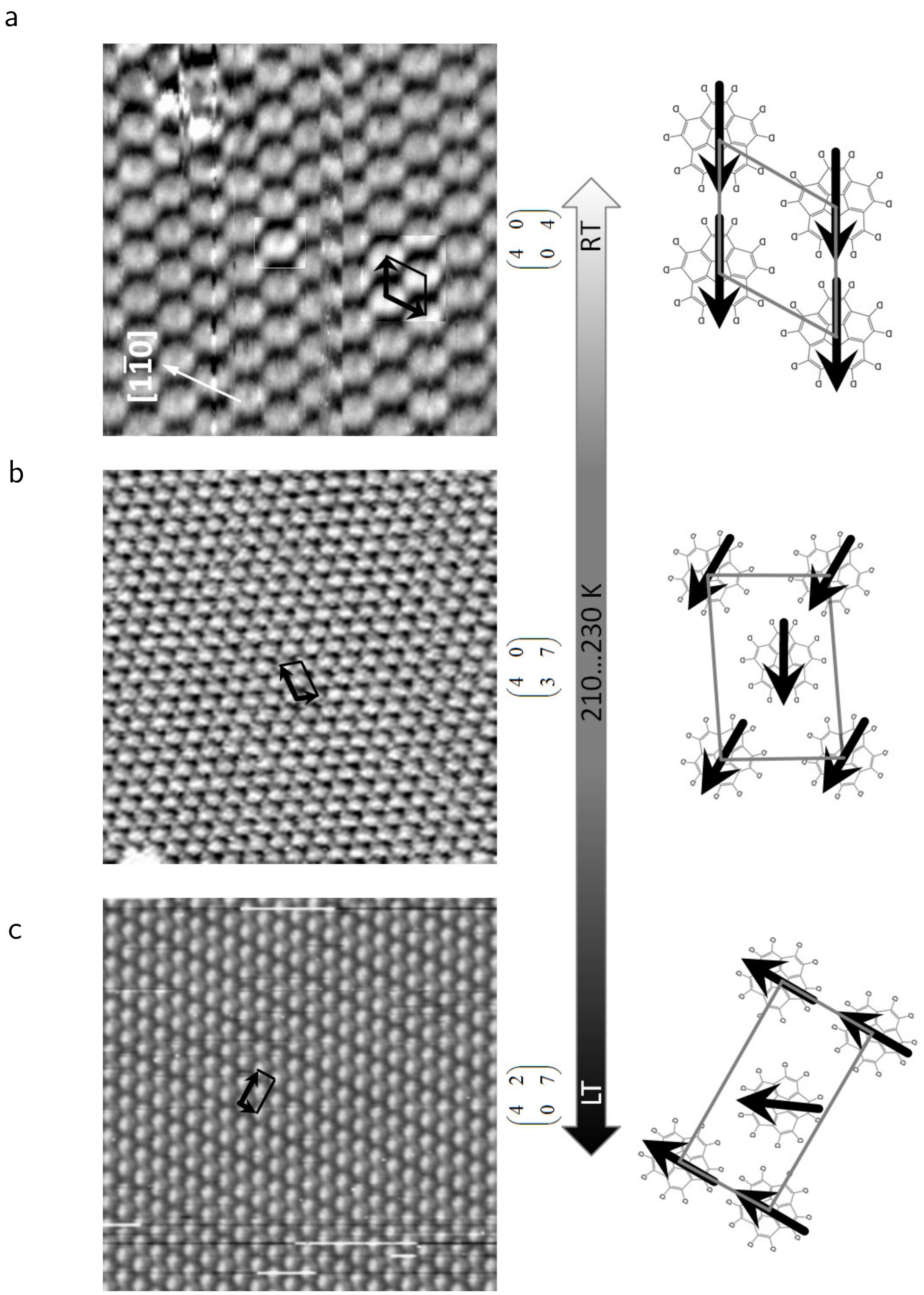

Figure 4.1.: *STM*-images of **2** on Cu(111) at different temperatures with superimposed unit cell vectors and models of each phase (arrows indicating tilt of the molecule, upwards): **a)** hexagonal-phase $10 \times 10\ \mathrm{nm}^2$, $-0.874\ \mathrm{V}$, $228\ \mathrm{pA}$, *RT* (inserts averaged over 63 positions; see Appendix A5 for procedure); **b)** transition-phase $40 \times 40\ \mathrm{nm}^2$, $-0.657\ \mathrm{V}$, $91\ \mathrm{pA}$, $220\ \mathrm{K}$; **c)** stripe-phase $40 \times 40\ \mathrm{nm}^2$, $-0.987\ \mathrm{V}$, $55\ \mathrm{pA}$, $80\ \mathrm{K}$. **a-c)** Upon cooling, the (4 0, 0 4) phase rearranges into a (4 0, 3 7) phase and upon further cooling into a (4 2, 0 7) phase. This whole process is completely reversible.

The surface density of the hexagonal phase, observed at room temperature, is calculated to be one molecule per 16 Cu(111) surface atoms. Both of the other phases are more dense, with one molecule per 14 Cu(111) surface atoms. This $14\ \%$ molecular surface density increase is the result from the rearrangement of the molecules. The contraction during the first phase transition leaves some areas of the surface behind where some of the molecule could not follow the contraction and form a disordered low density phase. Figure 4.2 shows such an area, in which molecules are frozen into a disordered "2D gas" next to the low temperature ($85\ \mathrm{K}$) stripe phase. Disordered low density areas appear already after the first phase transition ($< 230\ \mathrm{K}$), but due to the high mobility of the molecules a further cooling of the sample is necessary in order to obtain a *STM*-image.

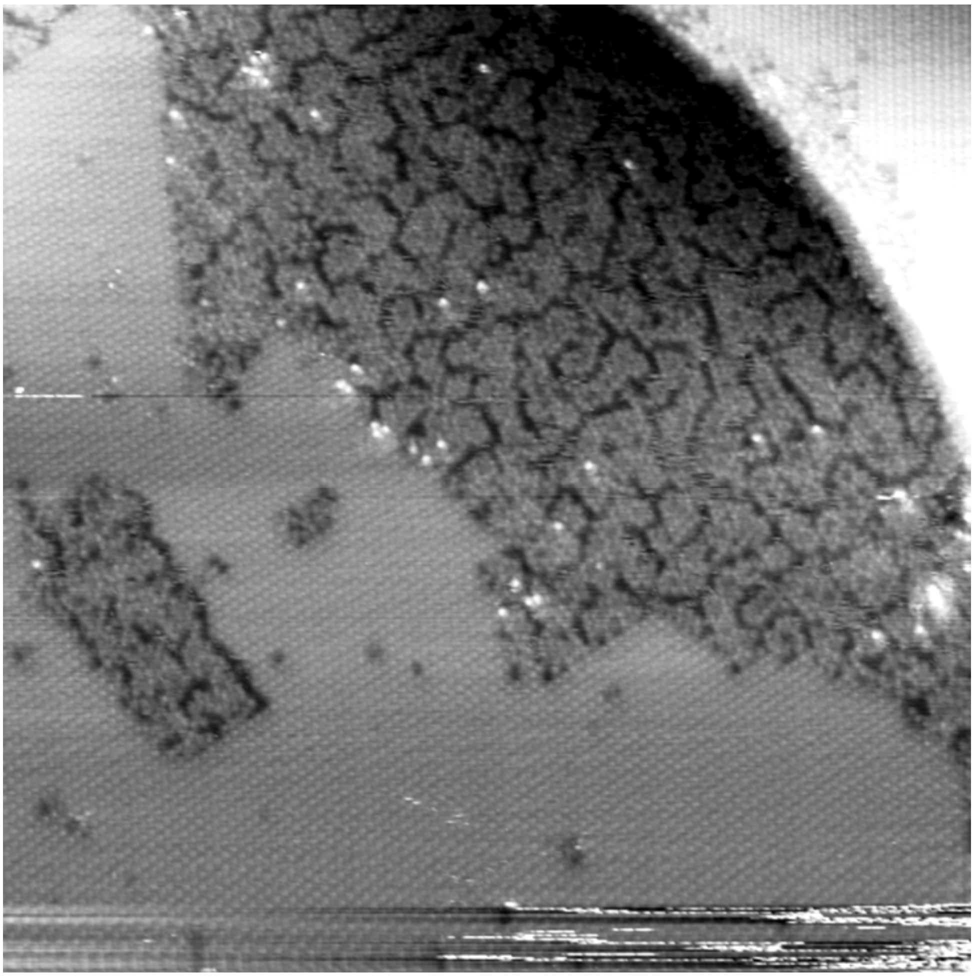

Figure 4.2.: A disordered low density phase of **2** congeals beside the stripe-phase at low temperature (*STM*-image: $100 \times 100\ \mathrm{nm}^2$, $-0.822\ \mathrm{V}$, $25\ \mathrm{pA}$, $85\ \mathrm{K}$).

A *LT*-*STM*-image of an incomplete epitaxial grown second layer of **2** on Cu(111) is shown in Figure 4.3. Perdeutero-corannulene was sublimed at $383\ \mathrm{K}$ for $5\ \mathrm{min}$ onto Cu(111) held at room temperature and subsequently cooled below $80\ \mathrm{K}$. White lines in the figure representing a row of molecules in the layer underneath. The intersections are directly in the middle of a molecule in the second layer, which shows identical lattice periodicity as the layer underneath. This together with the *DFT-D* calculations for bowl-in-bowl **1** (Fig. 3.8) and the second-layer growth of **1** on Cu(111) (Fig. 3.4) gives a strong hint for a bowl-in-bowl stacking-assisted growth.

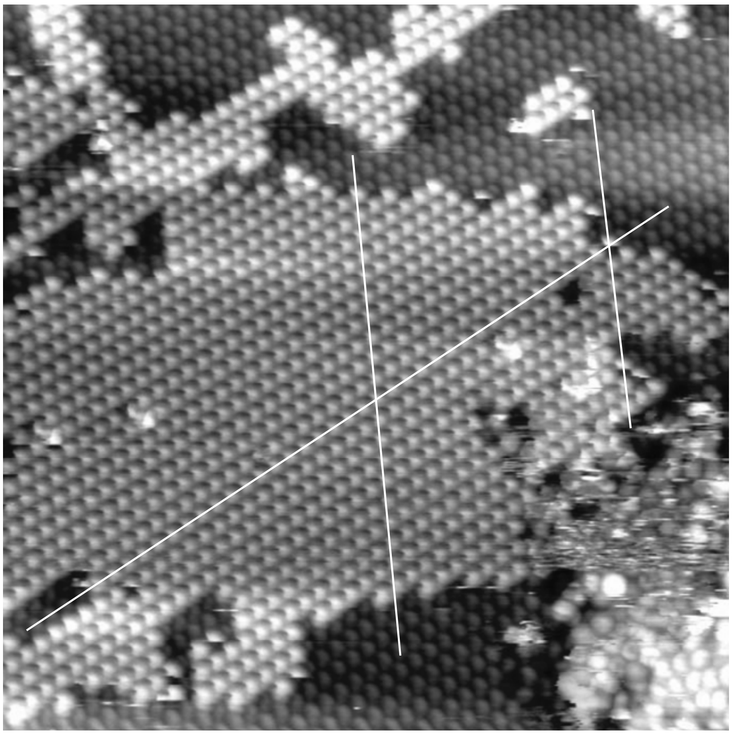

Figure 4.3.: *STM*-image of incomplete filled 2nd layer of **2** on Cu(111) ($40 \times 40\ \mathrm{nm}^2$, $-1.049\ \mathrm{V}$, $24\ \mathrm{pA}$, $80\ \mathrm{K}$). Lines along the periodicity of the layer underneath reveal on bowl-in-bowl growth of the second layer with identical lattice periodicity.

Discussion:

The reversible phase-transition behavior of **2** on Cu(111) has precisely the same unit cells and transition temperatures as corannulene shows on Cu(111) (Chapter 3). The low density islands next to the (4 0, 3 7) phase and *LT* phase are also identical to observations made from **1** on Cu(111). An isotope influence as suggested from previous studies could not be identified. Different isotopes at the rim of the buckybowl do not seem to influence the mobility on the surface or the phase transition, or the influence of the temperature change is too small to be observable with our *STM*. Epitaxial second layer bowl-in-bowl growth is also identical to observations in the second layer growth of corannulene. An open question is: are the second layer molecules precisely on top on each other, as it was calculated for corannulene, or does the deuterium at the rim cause a slight azimuthal rotation?

For further investigation, vibrational analysis of **1** and **2** performed with HyperChem7 using the AMBER force field algorithm could give a hint, why no change was observed (Fig. 4.4). The wavenumber of the first vibrational mode, which is the bowl-inversion mode for the free molecule and the bowl-breathing mode or wiggling mode for the adsorbed molecule, was calculated (Fig. 4.5). The calculated vibrational modes for **1** and **2** are $235.21\ \mathrm{cm}^{-1}$ and $221.1\ \mathrm{cm}^{-1}$, respectively. These wavenumbers correspond to a temperature of $338.41\ \mathrm{K}$ and $318.11\ \mathrm{K}$, respectively, calculated by setting the thermal energy $E_{th} = k_B T$ and the converted wavenumber via the Planck relation $E = h\tilde{\nu}c$ equal (Equ. 4.1):

$$T = \frac{h\tilde{\nu}c}{k_B} \tag{4.1}$$

with h being the Planck constant, $\tilde{\nu}$ the wavenumber, c the speed of light, and k_B the Boltzmann constant. The calculated temperature difference of $\sim 20\ \mathrm{K}$ (for the free molecules) should be observable with *STM*, but this was not the case. The calculated temperature difference of the adsorbed molecules might be too small ($\sim 2\ \mathrm{K}$) to be observable with *STM*.

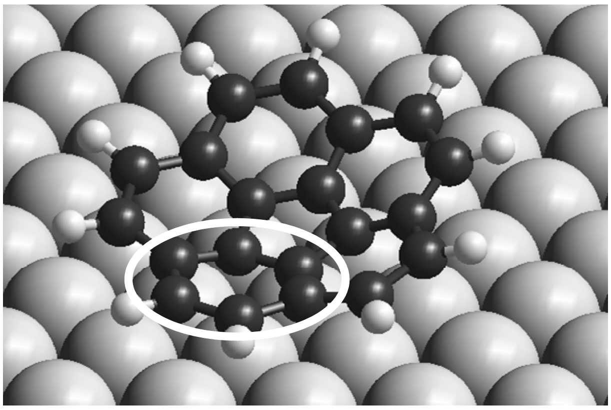

Figure 4.4.: Vibrational and rotational analysis of **1** and **2** on a Cu(111) slab of three atomic layers performed with HyperChem7. The Cu(111) substrate atoms as well as the highlighted C-atoms (parallel to the substrate surface) of the tilted **1** and **2** are fixed in their positions. Calculated first mode vibrations are $34.09\ \mathrm{cm}^{-1}$ and $33.02\ \mathrm{cm}^{-1}$, respectively, corresponding to a temperature of $49,05\ \mathrm{K}$ and $47.61\ \mathrm{K}$, respectively.

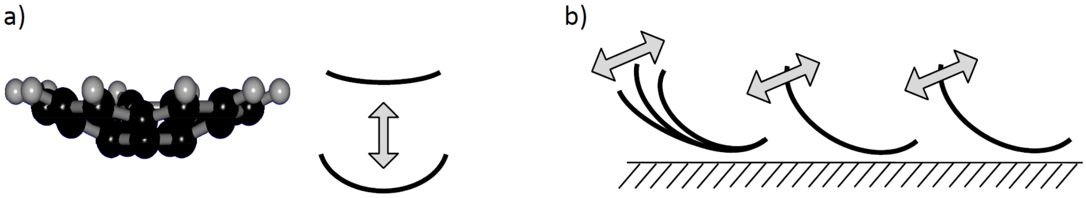

Figure 4.5.: First vibrational modes of **1** and **2**. a) Bowl-inversion or bowl-breathing mode of the free molecule in the gas phase and b) bowl-breathing or wiggling mode of the adsorbed molecule.

Migration of molecules from the room temperature, hexagonal phase into the first transition phase below $230\ \mathrm{K}$ results in a $14\ \%$ molecular surface density increase. This $14\ \%$ increase in surface density of the molecules via the first phase transition could be explained in the same way as it was for **1** on Cu(111). The contraction of the monolayer is thought to be caused by the wriggling motion of the molecules as they hop in a zipper-like migration between *fcc* and *hcp* threefold hollow binding sites [115]. The second phase transition is not accompanied by a further change in the surface density, as the molecules rearrange into the low temperature phase.

5. Pentaphenyl-corannulene: recognition of chirality?

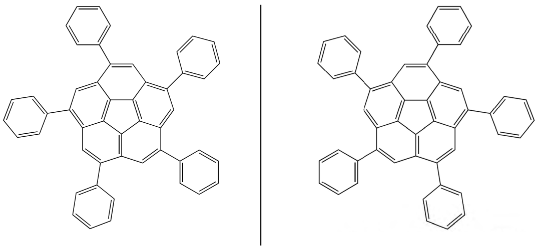

5.1. Self-assembly

A chiral influence on the self-assembly behavior of Cl- of methyl-1,3,5,7,9-penta-substituted corannulene (**3** and **4**) could not be identified. By increasing the size of the substituents to give the pentagonal molecules a more five-pointed star shape, a chiral recognition of the molecules, if it occurs, becomes more likely to be observable in *STM*. Evenly distributed bulky substituents, e.g. the chloride and methyl groups of **3** and **4**, respectively, at the rim of the buckybowl **1** force the molecule to maintain its C_5 symmetry upon adsorption due to the steric hindrance between molecule and surface. The phenyl groups of pentaphenyl-corannulene are expected to have the same effect for the same reason.

Pentaphenyl-corannulene molecules were evaporated from a Knudsen cell held at $460\ \mathrm{K}$ for $30\ \mathrm{min}$ to obtain a monolayer coverage on Cu(111) held at room temperature. All observed phases appeared already at *RT* and did not change during cooling of the crystal substrate to *LT* $(64\ \mathrm{K})$.

Some interesting features are observable in the high resolution *STM*-image (Fig. 5.1). The entire molecule can clearly be depicted, showing its centered **1**-backbone surrounded by its five phenyl-groups (Fig. 5.1a). However, the chirality of the molecule could not be determined. The *LT*-*STM*-image in figure 5.1a shows a phase, in which every second row of molecules is oriented in the same way (azimuthal variation within the rows) and every second molecule within one row is pointing in the same direction. The points of the star-shaped molecules follow a zig-zag motif, with a second glide plane but no mirror plane, thus belonging to the

p2gg crystallographic group. Four different oriented molecules span this (13 7, −1 11)^{M} domain (*M* representing the mirror unit cell according to the rules describes in [99]) unit cell. Determination of the unit cell was done by taking a series of consecutive *STM*-images to compensate drift. The lengths and angles between the unit cell vectors where determined from the Fast-Fourier-Transformation (*FFT*)-*STM*-images.
The averaged *LT*-*STM*-image in figure 5.1b shows another phase found within the monolayer. Here, the molecules show no azimuthal variation within the rows. The antiparallel orientation of the rows of five-pointed star-shaped molecules belong the the *p2mg* crystallographic group. Two different oriented molecules are located within the (7 6, −5 6) unit cell of this phase.
In order to obtain a denser packing in both phases, the phenyl-groups are interlocked with each other forming a cogwheel-like structure. Sometimes not all of the phenyl-groups are visible, possibly due to overlapping of the phenyl-groups with the neighbour molecule.

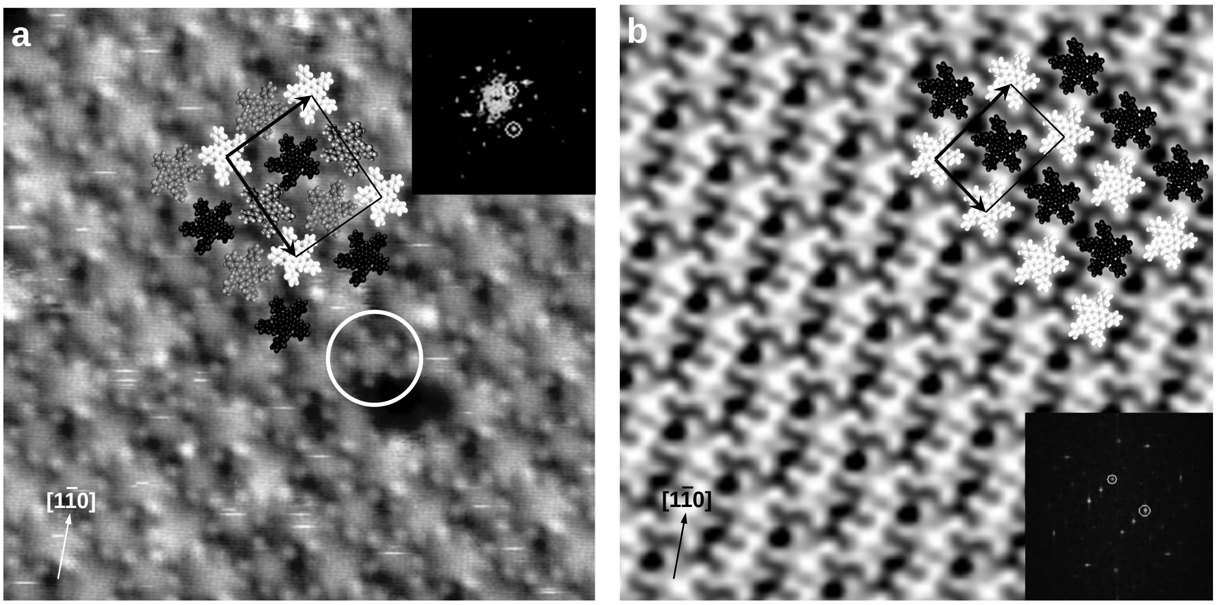

Figure 5.1.: **(a)** Nearby a defect the complete molecule with all five phenyl rings can clearly be identified. Every 2nd row of molecules is oriented in the same way (azimuthal variation within the rows) and every 2nd molecule within one roe is pointing in the same direction ($15 \times 15\,\mathrm{nm}$, $0.743\,\mathrm{V}$, $25\,\mathrm{pA}$, $64\,\mathrm{K}$). **(b)** *STM*-image averaged over 200 positions shows an antiparallel stripe assembly ($13 \times 13\,\mathrm{nm}$, $0.857\,\mathrm{V}$, $56\,\mathrm{pA}$, $64\,\mathrm{K}$). **(a)** and **(b)** reveal the interdigitation of the phenyl-groups and superimposed are models highlighting the structures (models having the same orientation are depicted in the same brightness). The inserts show the *FFT* of the *STM*-image used for unit cell determination.

In Fig. 5.2 two phases within the *ML* are shown: in the upper part, the (13 7, −1 11)^{M} phase, and in the lower part, the (7 6, −5 6) antiparallel-stripe phase. Very narrow phase boundaries appear due to reorientation of molecules (marked in the figure with a line) or coincide with substrate terrace step edges (not shown). From large area *STM*-images, the distribution of the two phases was determined to cover equal area $(50 : 50 \pm 3\ \%)$. In the (13 7, −1 11) unit cells one molecule covers 37.5 and in the (7 6, −5 6) unit cell one molecule covers 36 Cu(111) surface atoms.

The uniform appearance of the molecule in the *STM*-images suggests a parallel adsorption of the corannulene moiety on the substrate surface, also observed for **3** and **4** on Cu(111). Corannulene and derivatives were always found to adsorb bowl-opening up. Dark central spots on the molecules in the *STM*-image (Appendix A6) suggest the same adsorption orientation (bowl-opening up) for pentaphenyl-corannulene.

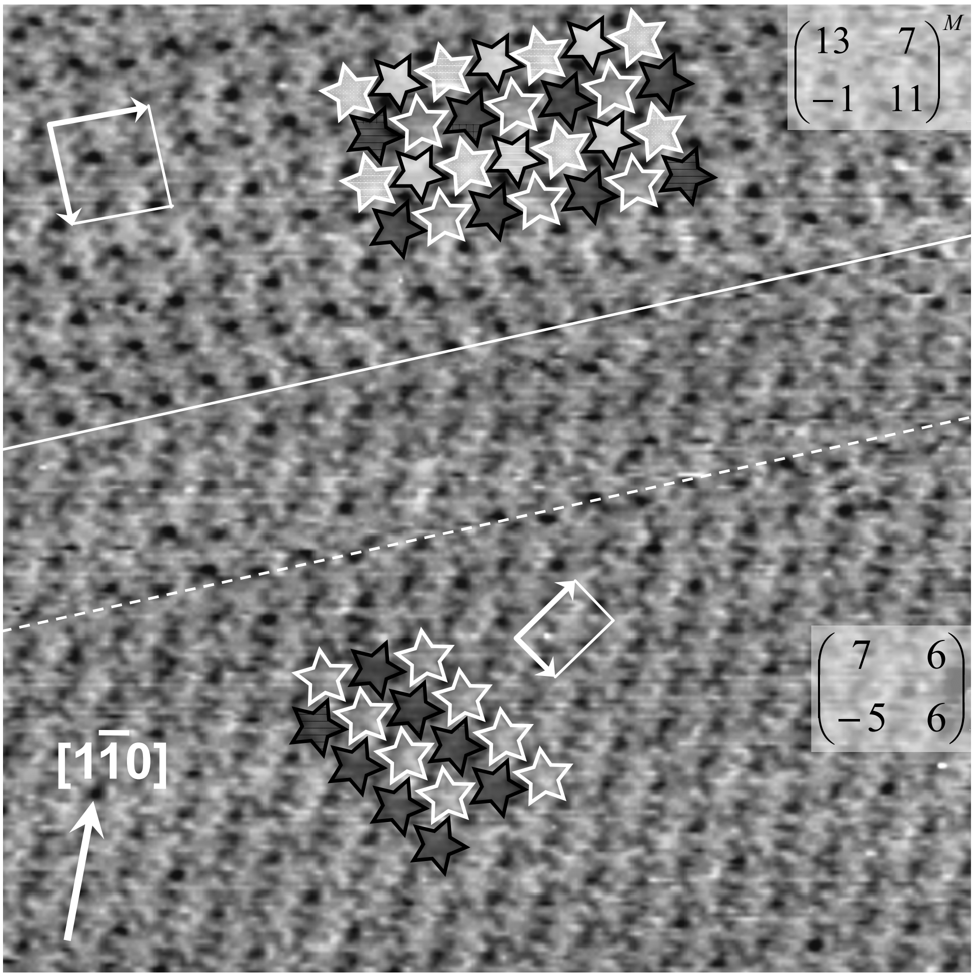

Figure 5.2.: At *ML*-coverage two phases with (13 7, −1 11)$^{\mathrm{M}}$ and (7 6, −5 6) unit cells of pentaphenyl-corannulene coexist. Very narrow phase boundaries are due to reoriented molecules. Superimposed stars highlight the packing motifs and unit cell vectors are depicted. $(55 \times 55\ \mathrm{nm}^2,\ 0.857\ \mathrm{V},\ 56\ \mathrm{pA},$ *RT*).

The *STM*-images do not reveal the handedness of the molecules and therefore hetero- or homochiral domains can not be assigned. However, the chiral recognition between the molecules might be the reason that two phases are observed. One phase might be built up by a racemic mixture of molecules, while the other is built up by a homochiral conglomerate. For both phases, mirror domains are found in the *STM*-images. Models for the two phases with homo- and heterochiral content are depicted in Fig. 5.3. Phases built up from opposite homo- or heterochiral content have similar packing densities.

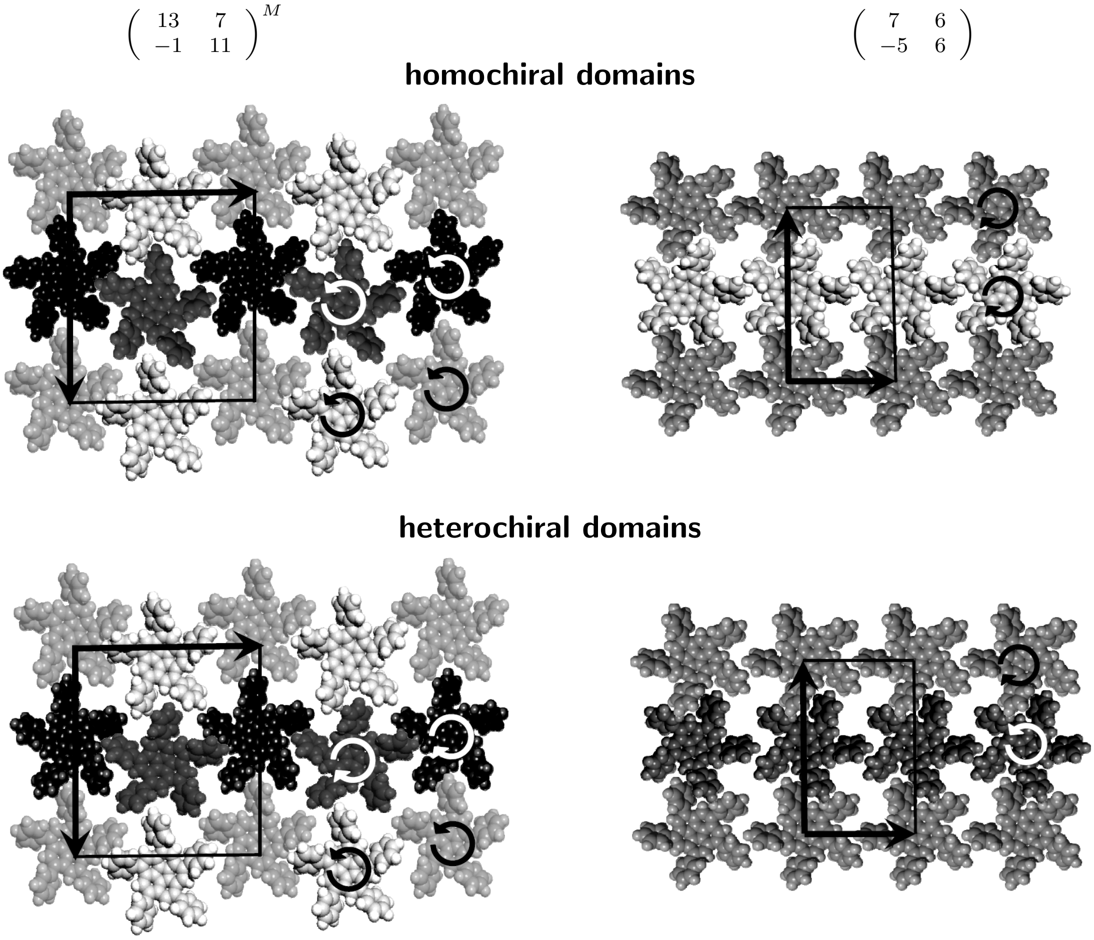

Figure 5.3.: Models for the two phases with homo- and heterochiral content. Different azimuthal orientations are indicated with different brightnesses and contrasts. Superimposed are unit cell vectors and chiral indication.

Four five-pointed star-shaped molecules built up the unit cell of the (13 7, −1 11) phase. Adjacent rows show different orientations of the stars and within a row every second star is oriented in the same way. Two glide planes in the respectable direction and no mirror plane makes this phase belong to the *p2gg* crystallographic group. The structure of the (7 6, −5 6) phase shows a mirror plane along the rows of stars, and a glide plane perpendicular to it, thus the anti-parallel stripe phase belongs to the *p2mg* group (Fig. 5.4). Packings observed for **3** and **4** and those observed for hard pentagons are also in the *p2mg* crystallographic group. Packing fractions for these closest packed phases vary with the opening angle of the stars (0.921 for 180°, pentagons; zero for 72°, stick figure).

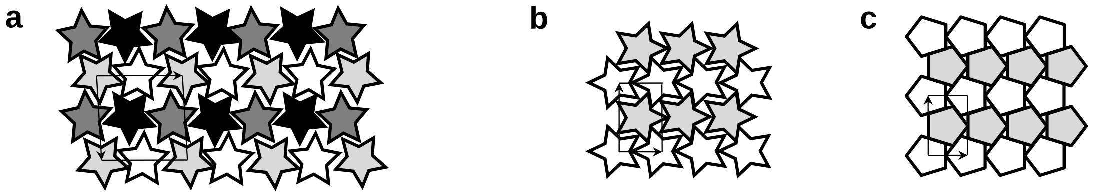

Figure 5.4.: Packing patterns for stars and pentagons. **(a)** The (13 7, −1 11)$^{\mathrm{M}}$ associated with the *p2gg* symmetry group (different orientations are shown with different gray scales). **(b)** The packing of the (7 6, −5 6), the closest packings for stars (packing fraction of 0.82) and **(c)** pentagons, both associated with the *p2mg* symmetry group. Unit cell vectors are superimposed.

Do these phases already appear at low coverage of **5** on the surface? Figure 5.5 shows a *LT*-*STM*-image with approx. 0.5 monolayer coverage. A network or clustering of interdigitated pentaphenyl-corannulene molecules appear already at low coverage; no single molecules are observed. Interaction of the phenyl groups already appears to be the driving force in structure formation, as weak attractive interactions between the molecules form the two phases with increasing coverage.

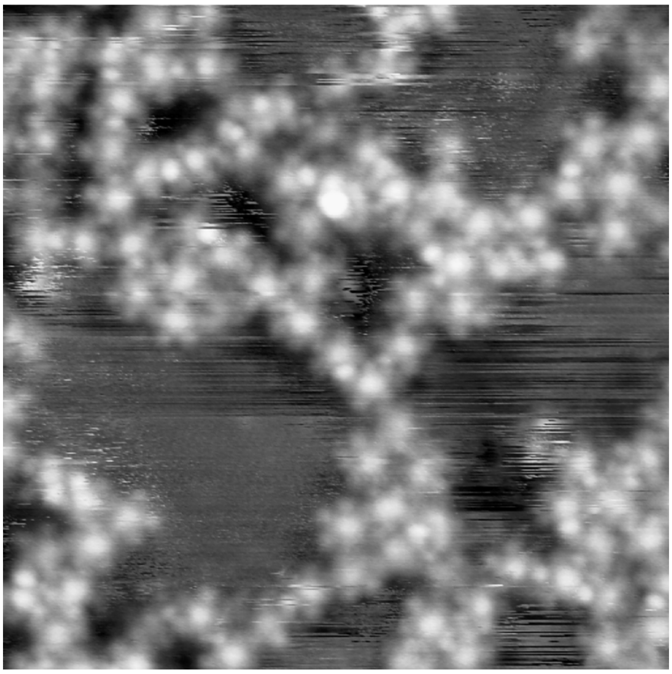

Figure 5.5.: Submonolayer coverage of **5** on Cu(111) shows that interaction of the phenyl groups is already taking place ($20 \times 20\,\mathrm{nm}^2$, $0.789\,\mathrm{V}$, $20\,\mathrm{pA}$, *RT*).

A comparison of *LEED* patterns obtained for a monolayer at different electron beam energies and simulated *LEED* patterns (using LEEDpat3) including rotational and mirror domains for the (7 6, −5 6) and (13 7, −1 11) in order to verify the found unit cells from *STM*, was not successful. The two coexisting domains result in a complicated superposition of *LEED* pattern, making it too difficult for the determination of the unit cells from the *LEED* (see Appendix A7).

FTIR-studies have been carried out to determine the phenyl group orientation towards the surface. The *FTIR*-spectra of **5** shows tilted phenyl groups, C-H, C-C, and C=C vibrational modes of the adsorbed molecule (Fig. 5.6). The vibrations at the wavenumber of $1042\ \mathrm{cm}^{-1}$, $1162\ \mathrm{cm}^{-1}$, $1260\ \mathrm{cm}^{-1}$ are assigned to the C-H in plane bending and stretching vibration of the phenyl group, and the vibrations at $1365\ \mathrm{cm}^{-1}$, $1454\ \mathrm{cm}^{-1}$, and $1600\ \mathrm{cm}^{-1}$ to different phenyl-ring modes and an overtone band at $1715\ \mathrm{cm}^{-1}$. Three C-H stretching vibrational bands appear between $2800\ \mathrm{cm}^{-1}$ and $3000\ \mathrm{cm}^{-1}$ [130–132]. The fact, that a vibrational spectra is observed in the *FTIR* experiments at all, indicates a more or less perpendicular vibration to the surface.

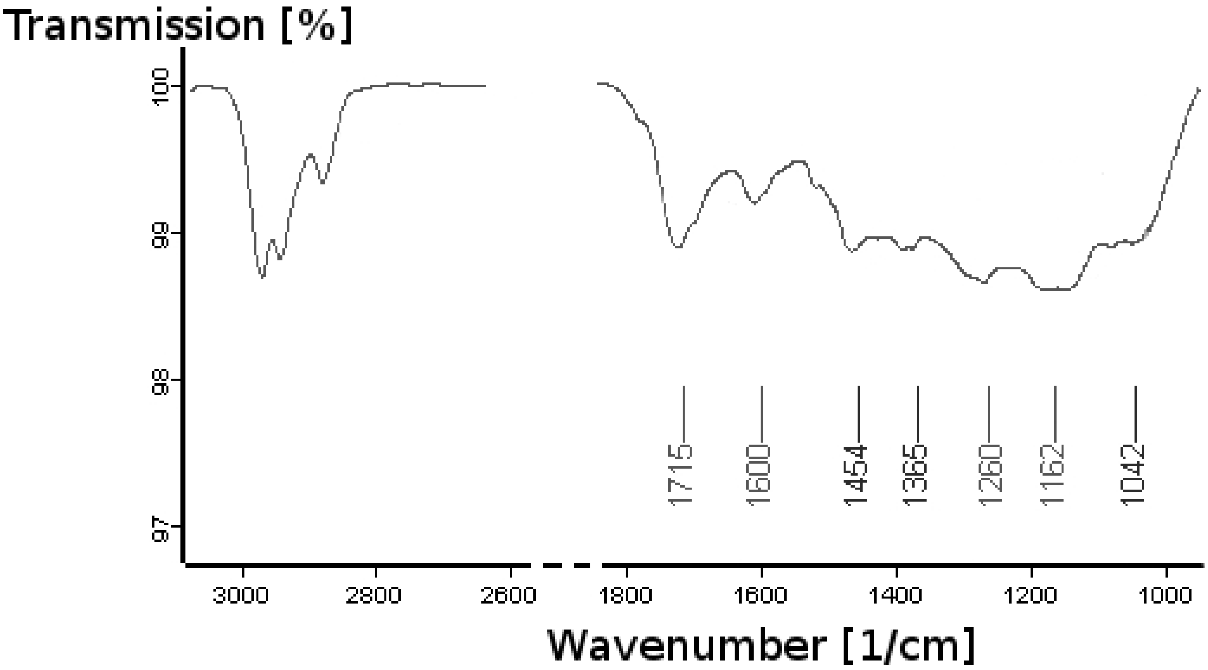

Figure 5.6.: *FTIR*-spectra during step wise sublimation of **5** onto Cu(111). Spectra taken at 1 *ML* coverage and 240 °C in order to have a stronger appearance of the vibrational structure. C-H stretching vibrations appear at $3000 \ldots 2800\ \mathrm{cm}^{-1}$, overtone and phenyl ring modes at $1715 \ldots 1365\ \mathrm{cm}^{-1}$, and C-H bending in-plane bending modes at $1260 \ldots 1042\ \mathrm{cm}^{-1}$.

In order to verify the thermal stability of the adsorbed overlayer structures, *TPD*-experiments have been carried out. They revealed a dehydrogenation of the adsorbed molecules at $563\ \mathrm{K}$ (Appendix A8), but no other changes could be observed. Experiments trying to detect mass $78\ \mathrm{amu}$ (which would correspond to benzene expulsion) showed no desorption peak at all. Detection of the whole molecule, which would correspond to (multilayer) desorption of **5**, was not possible because the mass is too large to be detected in our mass spectrometer.

5.2. Electronic properties

A *UPS* study shows the evolution of molecular orbitals of **5** on Cu(111) (Fig. 5.9). The angle between the *UV* source (He I, $21.2\ \mathrm{eV}$) and the substrate normal was $10°$ (light incidence angles), the angle between the substrate normal and the analyzer $80°$ (electron emission angle), and the angle between the *UV* source and the analyzer $90°$. Work function measurements were done with the sample biased at $-9\ \mathrm{V}$.

Figure 5.9 shows the valence band of clean Cu(111) as well as those of pentaphenyl-corannulene in 1 *ML*, 2 *ML*, and 3 *ML* coverage. An evolving overlap of the molecular orbitals of **5** and the copper sp band is the result of multilayer growth. An overlap with the copper d band could not be observed. Molecular orbital (*MO*) calculations of the free molecule were performed with HyperChem7 on *ab initio* level of theory, including MP2 correlation with a 3-21G basis set (listed in Table 5.1) and correlated to the valence band spectra. The evolving peak around the Cu sp band at $\sim 4\ \mathrm{eV}$ be assigned as the *HOMO*...*HOMO*-3, the peak at $6 \ldots 7.5\ \mathrm{eV}$ as the *HOMO*-4...*HOMO*-13, and the peak around $8 \ldots 9\ \mathrm{eV}$ as the *HOMO*-14...*HOMO*-16. The spectra shows no charge transfer from the substrate into **5** as new states would appear close to the Fermi level. Multilayer growth shows no shift in the local maxima of the observed spectra. The evolving band structure of **5** on Cu(111) is clearly different from those obtained in *UPS* studies performed with corannulene on Cu(110) [60]. In the case of **1** on Cu(110) the highest occupied molecular orbital *HOMO*...*HOMO*-3 overlap with the Cu d and sp band. The case of **1** on Cu(111) is similar but a little bit more broadened [84, 85].

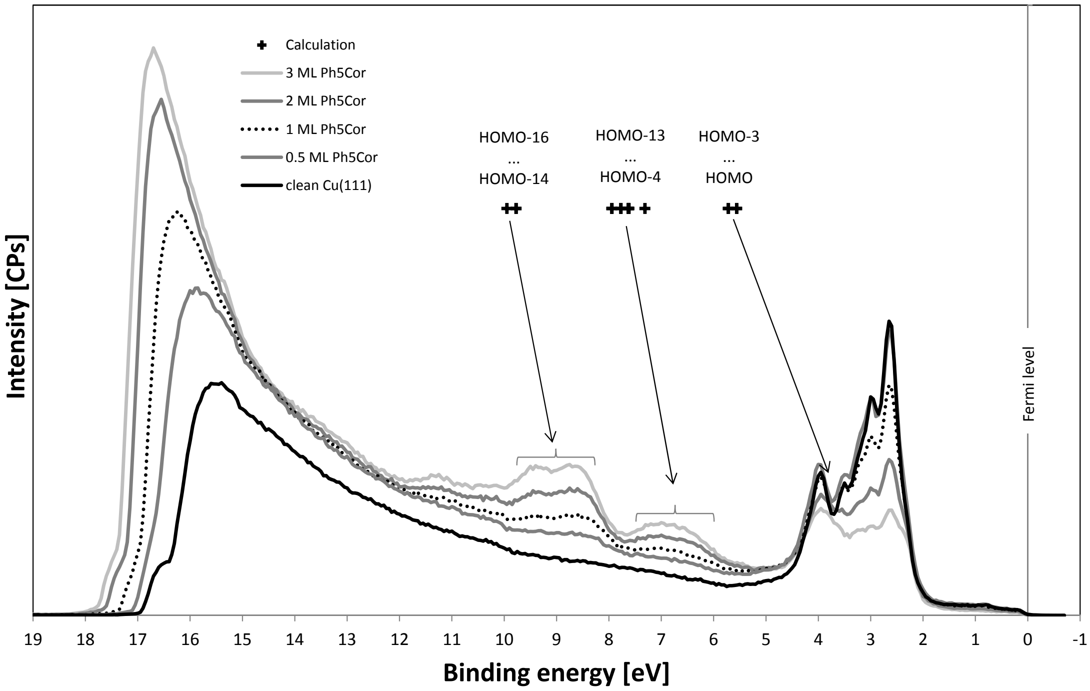

Figure 5.7.: Evolution of the bands of **5** adsorption on Cu(111). The absolute molecular orbital energies from *ab initio* calculations (including MP2 correlation) can be assigned to an overlapping band evolving at the Cu sp band (*HOMO*...*HOMO*-3). The peak evolving at $6\ldots7.5\,\mathrm{eV}$ assigned as the *HOMO*-4...*HOMO*-13, and the peak around $8\ldots9\,\mathrm{eV}$ as the *HOMO*-14...*HOMO*-16.

Table 5.1.: Molecular orbital calculation for **5** at *ab initio* level of theory, including MP2 correlation and 3-21G basis set (performed with HyperChem7).

Orbital **Symmetry** **Orbital eigenvalue** [eV]	**Isosurface MO**		**Orbital** **Symmetry** **Orbital eigenvalue** [eV]
LUMO+1 E1 3.937	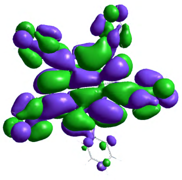	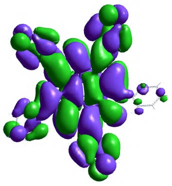	LUMO E1 3.937
HOMO E2 −5.560	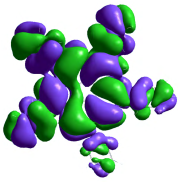	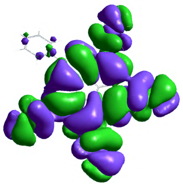	HOMO−1 E2 −5.560

Continued on next page

Table 5.1 – *Continued from previous page*

HOMO−2 E1 −5.719	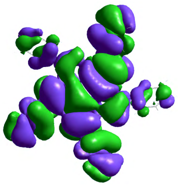	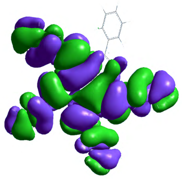	HOMO−3 E1 −5.719
HOMO−4 A −7.312	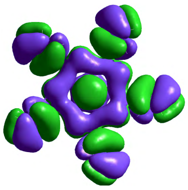	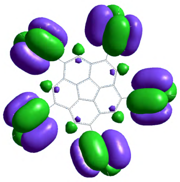	HOMO−5 A −7.617
HOMO−6 E1 −7.623	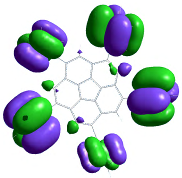	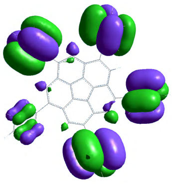	HOMO−7 E1 −7.623
HOMO−8 E2 −7.631	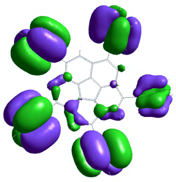	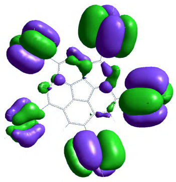	HOMO−9 E2 −7.631
HOMO−10 E2 −7.772	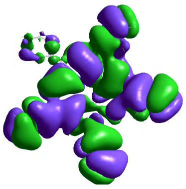	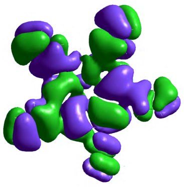	HOMO−11 E2 −7.772
HOMO−12 E1 −7.944	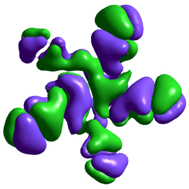	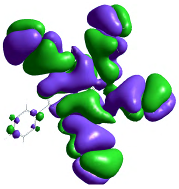	HOMO-13 E1 −7.944
HOMO−14 E2 −9.773	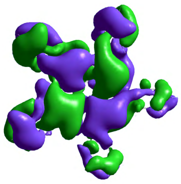	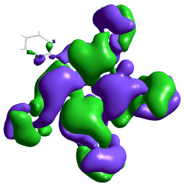	HOMO−15 E2 −9.773
HOMO−16 A −9.949	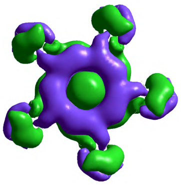		

Fig. 5.8 shows the work function change, starting from the clean Cu(111) substrate surface up to 3 *ML* coverage. The work function was determined with the procedure described in section 2.1.2, and the work function change via the subtraction of the work function of the clean substrate and the work function of the substrate with adsorbed **5**. The results of the determination of the work function changes are plotted in figure 5.9 as work function decrease versus the increase in coverage (lines are fit to guide the eye).
In the (7 6, −5 6) phase the area per molecule is $A = 1.016\,nm^2$ ($\sim$ 1 molecule/36 Cu-atoms), gives a monolayer coverage of $\theta_{1ML} = 9.84 \cdot 10^{17}\,\frac{molecules}{m^2}$. The interfacial dipole moment calculated with the Helmholtz equation (Equ. 2.3) at 0.25 monolayer and a work function change of $\Delta\phi = 0.316\,eV$ is $\mu = 3.4\,D$. The maximum work function change is -1.16 eV which has been determined at three *ML* coverage. At one monolayer coverage the work function change has been determined to -0.75 eV.

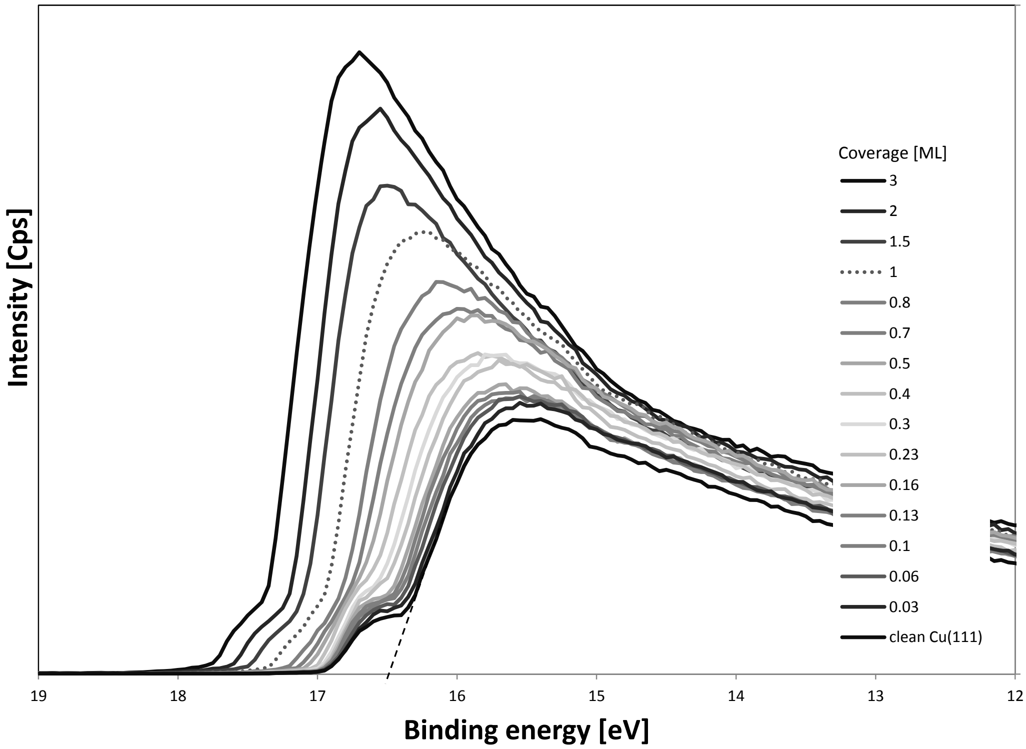

Figure 5.8.: Evolution of the work function change upon adsorption of **5** on Cu(111). Spectra recorded with an electron emission angle of 10°. The dotted line indicates the *ML*-coverage.

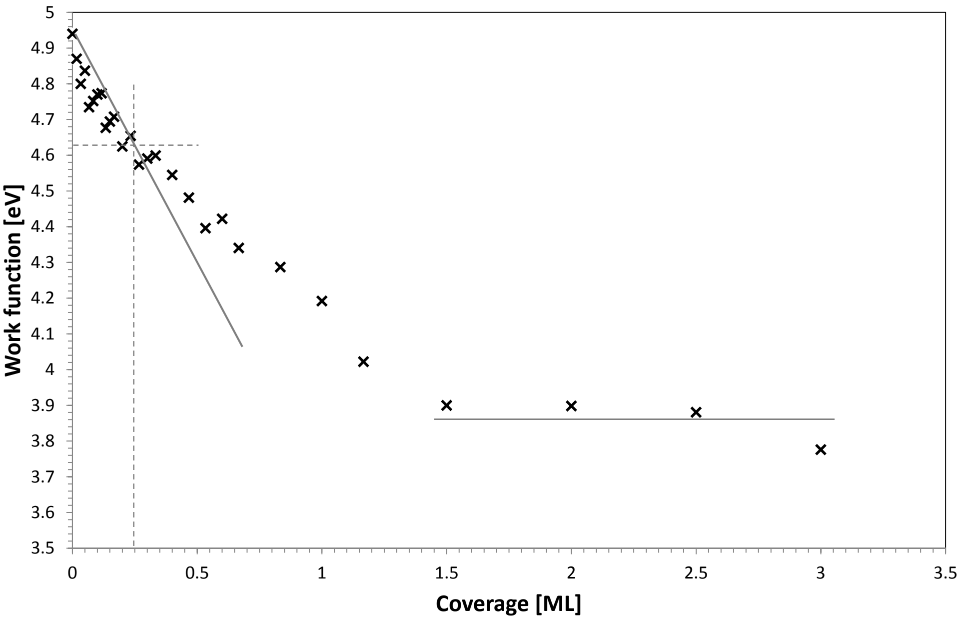

Figure 5.9.: Work function ϕ values of **5** adsorption on Cu(111). Work function change shows a linear adsorption for small coverage, from one monolayer on a small change of $-0.36\ \mathrm{eV}$ is observed, the maximum work function change is $-1.16\ \mathrm{eV}$. The error of the work function determination is smaller than $1\ \%$. Lines are drawn to guide the eye. The determined dipole moment at 0.25 *ML* coverage is $3.4\ \mathrm{D}$.

5.3. Summary

Self-assembly:

Two long-range ordered phases (7 6, −5 6) and (13 7, −1 11) coexist at *RT* and do not change during cooling, with a surface density of one molecule per 37.5 and 36 Cu(111) surface atoms, respectively. Hetero- and homochiral content in these self-assembled structures might be the reason, that two phases are observed. A mechanical model (hard stars) demonstrates that the (7 6, −5 6) molecular arrangement is most likely the densest possible packing of the fivefold symmetric star-shaped pentaphenyl-corannulene. The rigid star model for the striped phase (Fig. 5.4b) represents a rectangular structure with *p2mg* plane group symmetry. The interdigitation of the phenyl groups of the molecules starts already at low coverages.

Although the observed *FTIR*-spectra is quite complicated it confirms the assumption that the phenyl groups are tilted towards an more upright orientation on the surface. Pentaphenyl-corannulene shows a parallel (bowl-opening perpendicular to the surface) adsorption mode with tilted phenyl groups. Hydrogen decomposition of **5** appears at a temperature of $563\ \mathrm{K}$. No other decomposition fragments of **5** could be observed.

Two-dimensional crystallization patterns, which were predicted for hard pentagons [79, 82], were observed in *STM* for **3** and **4** on various metal surfaces.

Electronic properties:

The molecular orbitals seem to be aligned to their respective work function since the local maxima of the electronic valence band structure shows no shift with increase of coverage. No charge transfer into the LUMO of the adsorbed molecules is observed, which would have been identified by an intensity change around the Fermi level. Adsorption of molecules lead to an decrease of the work function with increasing coverage. A work function change of $-0.75\ \mathrm{eV}$ for one monolayer coverage and a total work function change of $1.16\ \mathrm{eV}$ for multilayer growth were observed. The interface dipole moment was determined from the initial linear work function decrease with the Helmholtz equation to $3.4\ \mathrm{D}$. The interface dipole moment is significantly lower than those observed for **1** and **4** on Cu(111) varying between $6.5\ \mathrm{D}$ and $8.8\ \mathrm{D}$ for the monolayer coverage of their different phases. The work function change is also approximately just as half as large as **1** and **4** with values between $-1.3\ \mathrm{eV}$ and $-1.6\ \mathrm{eV}$.

6. Mono-indenocorannulene: C_{1v} symmetric bowl self-assembly

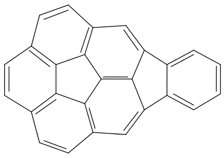

With the addition of a benzene ring to corannulene to form mono-indenocorannulene, the C_5 symmetry breaks down to a simple C_{1v} mirror symmetry. To investigate the influence of this symmetry breakdown on the two-dimensional crystallization behavior, the self-assembly of these molecules was studied. Two different copper surfaces have been investigated, one with threefold symmetry (Cu(111)) and one with fourfold symmetry (Cu(100)). Mono-indenocorannulene was evaporated from a Knudsen cell held at $423\,\mathrm{K}$ for $13\,\mathrm{min}$ to obtain a monolayer on the Cu(111) and Cu(100) single crystal surfaces held at room temperature.

6.1. Mono-indenocorannulene on Cu(111)

Low temperature *STM* images reveal the binding site of mono-indenocorannulene (Fig. 6.1). A clearly highlighted side of the corannulene molecule is known to indicate a tilted adsorption. This can be also seen in high-resolution *LT*-*STM*-images of **6** on Cu(111). The fivefold symmetric **1** backbone is clearly protruding upwards, as indicated by a highlighted appearance of one of the six-membered rings of the corannulene backbone, while the benzo moiety appears darker, similar to the other two six-membered rings adjacent to it. This indicates a more parallel alignment site of the benzene moiety to the copper surface. In combination with preliminary molecular model calculations and previous known binding sites, e.g. the one of the six-membered rings of corannulene is placed on top of fcc threefold hollow sites os the Cu(111) substrate, the benzo moiety of **6** are also placed on top of the threefold hollow sites of the Cu(111) surface (Fig. 6.1c).

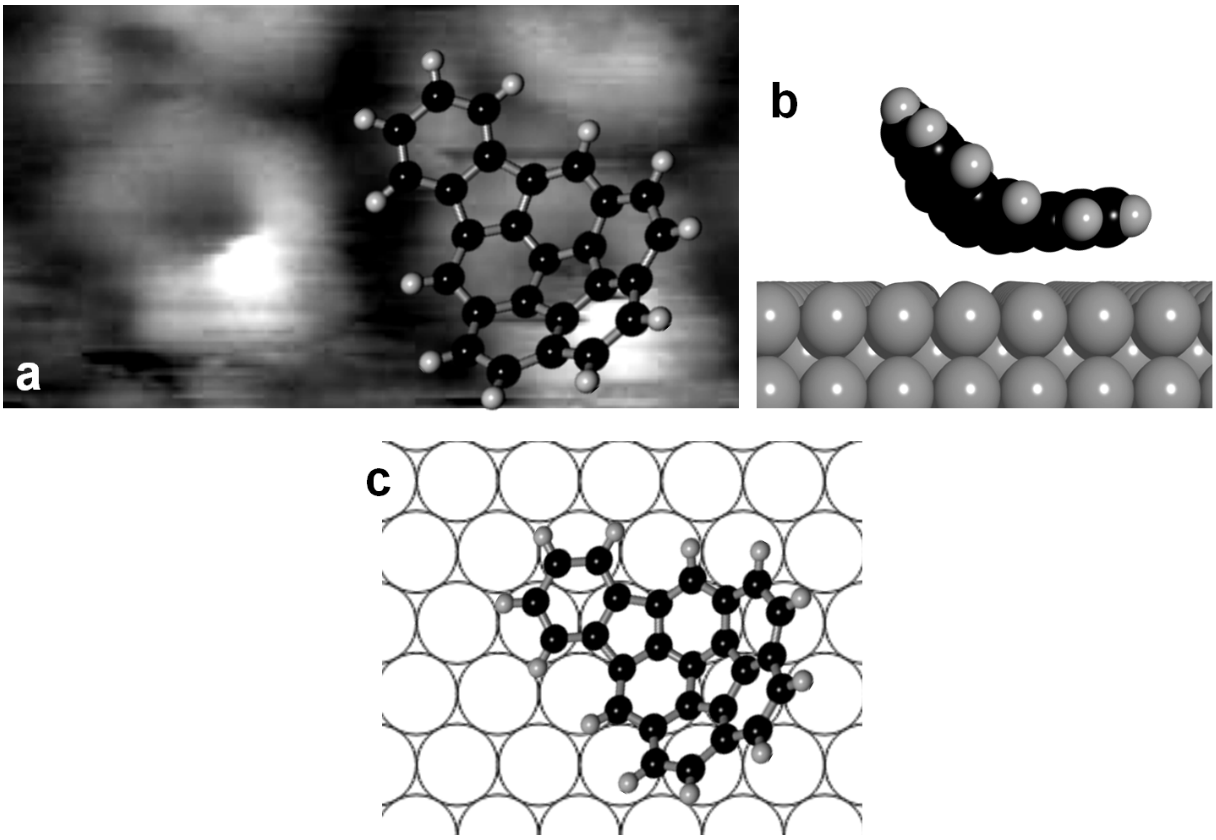

Figure 6.1.: Binding site of mono-indenocorannulene on Cu(111). **(a)** High-resolution *STM*-image of **6** on Cu(111) ($2.7 \times 1.3\ \mathrm{nm}^2$, $-1.162\ \mathrm{V}$, $253\ \mathrm{pA}$, $58\ \mathrm{K}$). **(b)** Structure model of adsorbate of tilted **6** on Cu(111). **(c)**: Model illustrating the preferred binding site with the additional six-membered ring adsorbed in the threefold hollow sites of the Cu(111) surface.

Figure 6.2 shows rotational and mirror domains at monolayer coverage with a mirror angle of $\sim 22^\circ$ between the two domains. The observed phase appears already at room temperature and is also stable during cooling down to low temperature ($64 \ldots 105\ \mathrm{K}$). Domains are built up by zig-zag rows of molecules forming a unit cell of (5 1, 2 7). The unit cell covers 33 Cu(111) surface atoms, one mono-indenocorannulene molecule covers 16.5 surface atoms. Annealing of the sample did not result in formation of larger domains.

The orientation of the molecules within the zig-zag rows is shown in Fig. 6.3. One of the two molecules of the unit cell is azimuthally rotated by $\sim 10^\circ$ (Fig. 6.3b). Models of the (5 1, 2 7) phase (Fig. 6.3c) show the zig-zag appearance molecules. The benzo moiety is assumed to be adsorbed on top of threefold hollow sites parallel to the Cu(111) surface. The zig-zag phase belong to the p1 crystallographic plane group.

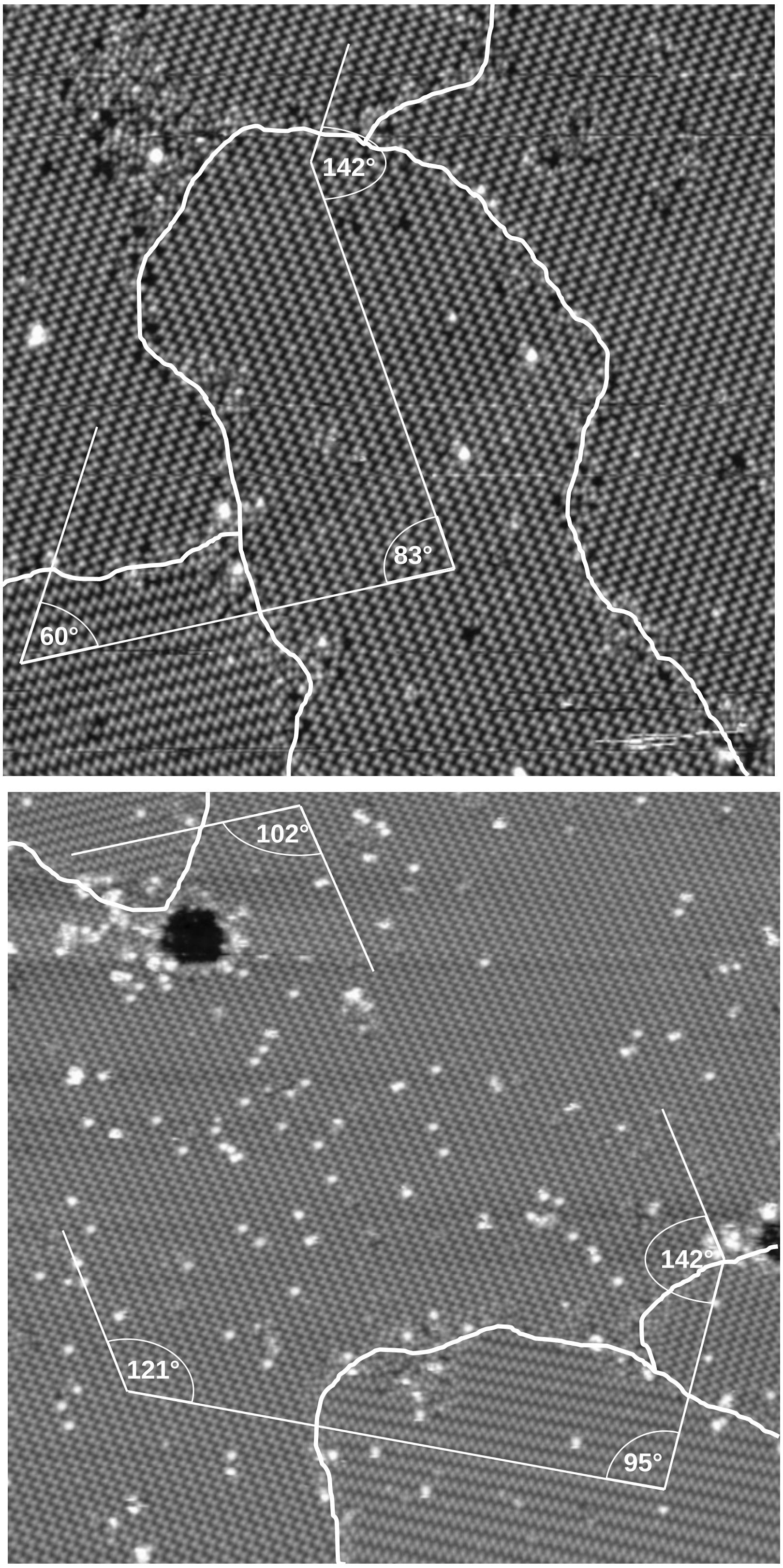

Figure 6.2.: *STM*-images of rotational and mirror domains of mono-indenocorannulene (mirror angle $\sim 22°$). **Upper:** Two rotational and one mirror domain ($80 \times 80\,\mathrm{nm}^2$, $-1.185\,\mathrm{V}$, $129\,\mathrm{pA}$, $63\,\mathrm{K}$). **Lower:** One rotational and three mirror domains ($100 \times 100\,\mathrm{nm}^2$, $-1.185\,\mathrm{V}$, $149\,\mathrm{pA}$, $63\,\mathrm{K}$)

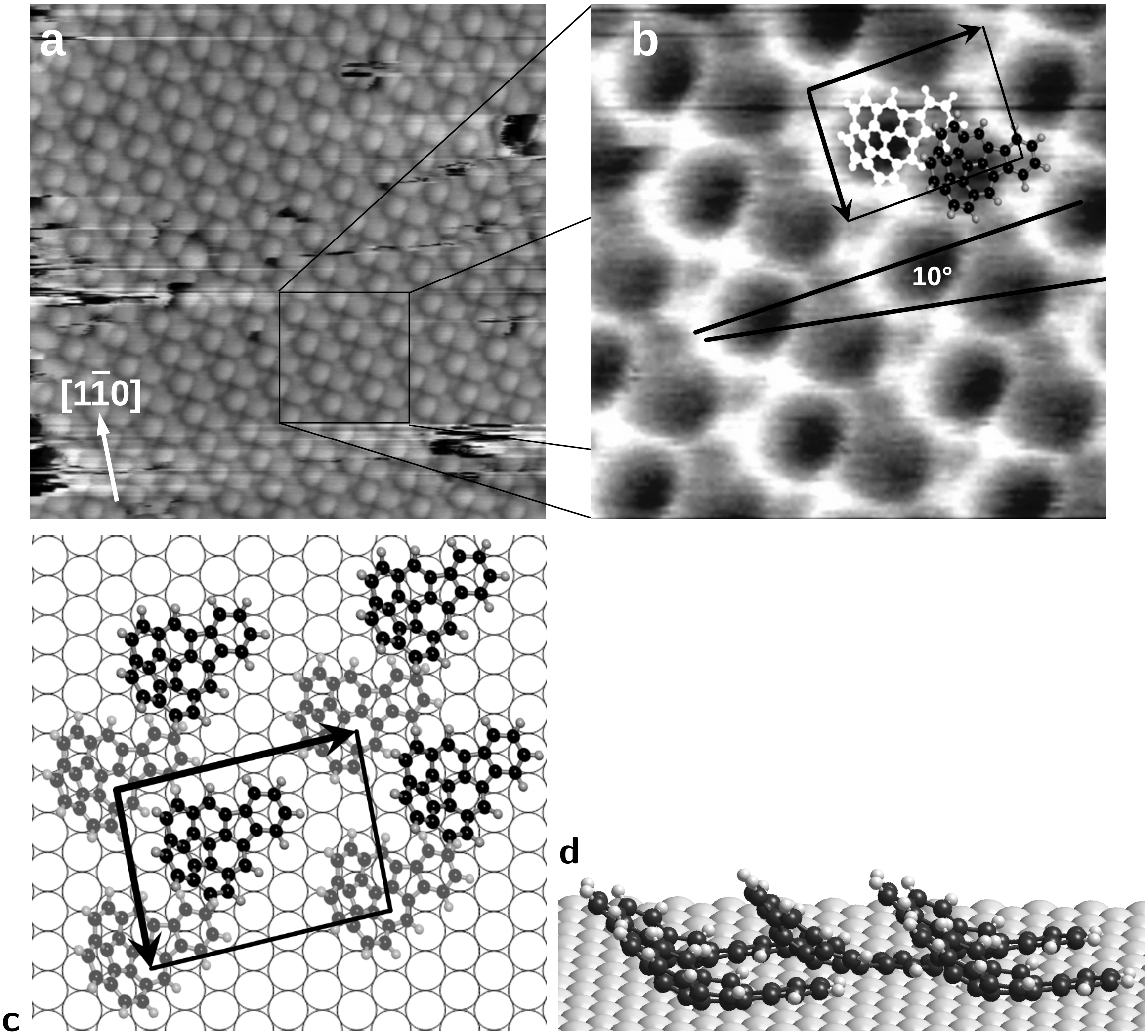

Figure 6.3.: *STM*-images of the zig-zag phase and structure model. **a)** Overview *STM*-image ($20 \times 20\,\mathrm{nm}^2$, $-2.617\,\mathrm{V}$, $47\,\mathrm{pA}$, $70\,\mathrm{K}$) of the (5 1, 2 7) phase. **b)** *STM*-image zoomed-in to $5 \times 5\,\mathrm{nm}^2$ with color inversion for better visibility and containing a superimposed unit cell. **c)**: A model illustrating the (5 1, 2 7) zig-zag phase, gray molecules are rotated by 10° relative to the black molecules and **d)** side view.

A low density (5 0, 4 8) phase is formed at ∼0.8 *ML* coverage, in which one molecule covers 20 Cu(111) surface atoms (Fig. 6.4a). Every molecule in every other row is rotated by 30°; therefore, the low density unit cell belongs to the p1 crystallographic plane group. Figure 6.4b shows a model fitting the *STM*-image illustrating the binding site reveals that the atoms of the benzene moiety is adsorbed on top of the threefold Cu(111) hollow sites. It also confirms the rotation in every second row, as this is compatible with the symmetry of the surface lattice, if only the top layer is considered. Every second row of molecules are adsorbed with their mirror plane parallel to the $\langle 110 \rangle$ direction of the surface. The molecules within the next row are azimuthally rotated by 30°.

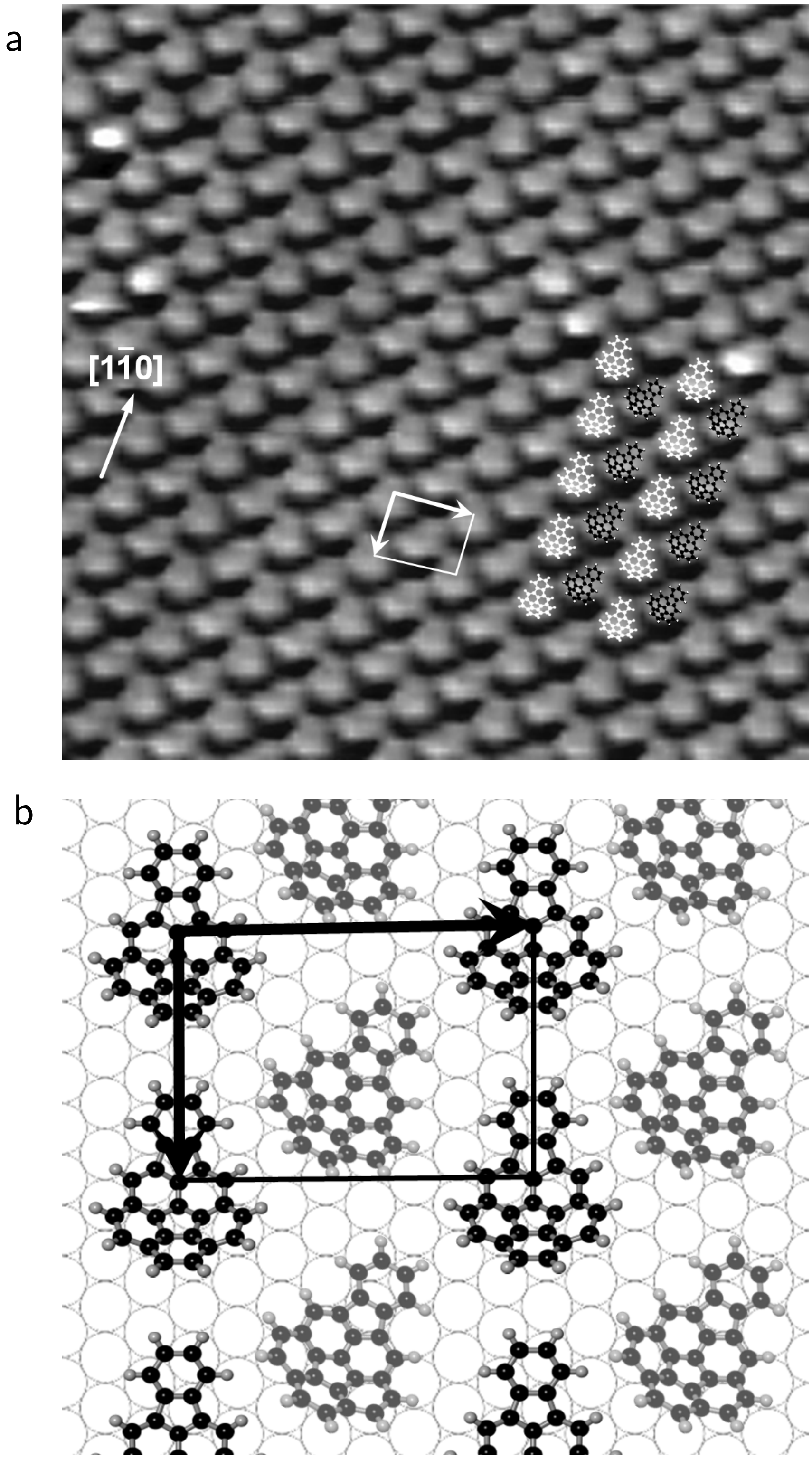

Figure 6.4.: **a)**: Low density (5 0, 4 8) phase with azimuthal (30°) tilted **6** molecules in every 2nd row $(15 \times 15\,\mathrm{nm}^2,\ -1.071\,\mathrm{V},\ 179\,\mathrm{pA},\ 85\,\mathrm{K})$. **b)**: A model of the low density phase superpositioned on a Cu(111) surface lattice (gray molecules rotated 30° relative to the black molecules). All molecules are place with the benzo groups on top of threefold hollow sites.

Figure 6.5 shows the an island of second layer molecules. The second layer shows a different appearance, but still has the same unit cell as determined for the monolayer. White and black lines imposing the periodicity of the second layer onto the layer underneath; white ellipses the molecules of the second layer. Bowl-in-bowl growth of the second layer seems not to be the favored mechanism. The phase shift from the first to the second layer can be caused if the multilayer growth starts from the empty spaces in between the zig-zag rows. The insert in Fig. shows a model of superimposed molecules on top of the empty spaces from the layer underneath with assumed bowl opening down molecules in the second layer (highlighted indeno-part of the molecule in the *STM*-image).

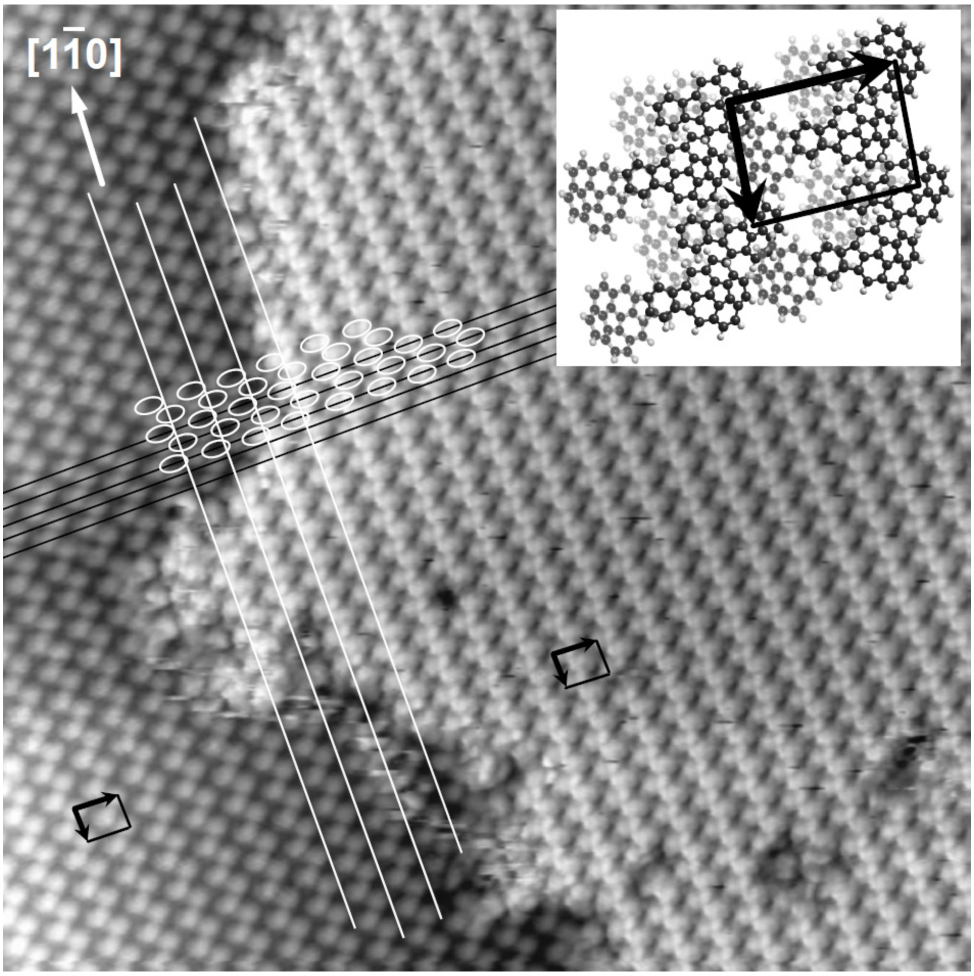

Figure 6.5.: *STM*-image of second layer **6** on Cu(111): $40 \times 40\ \mathrm{nm}^2$, $-2.513\ \mathrm{V}$, $42\ \mathrm{pA}$, $77\ \mathrm{K}$. Second layer growth begins from the empty spaces in between the zig-zag rows: white ellipses represent the molecules of the second layer, white and black lines impose the periodicity of the second onto the first layer. Superimposed unit cells are identical in both layers. The insert shows a proposed model.

6.2. Mono-indenocorannulene on Cu(100)

Figure 6.6 shows a monolayer of **6** on Cu(100). Island of rotational domains with a unit cell structure of (4 0, −1 4) appear at *RT* and are also stable during cooling to low temperature ($64 \ldots 115\,\mathrm{K}$). In this phase, one molecule covers 16 Cu(100) surface atoms. The quality of the *STM*-images do not allow to propose a preferred orientation of the molecule. However, simple MM+ force field molecular mechanics calculations performed with HyperChem7 suggest an binding site such that the bond along the mirror plane, in between two six-membered rings of the **1**-backbone (the "spoke"-bond which is along the mirror plane), is on top of a fourfold hollow site of the Cu(100) surface lattice along the $\langle 100 \rangle$ direction an parallel aligned to the surface. For the calculation, two atomic copper substrate layers are fixed and a random oriented **6** close by are relaxed to find the minimal energetic position (Fig. 6.7). Top, side, and front view from the single **6** on a Cu(100) slap are shown in figure 6.9. Figure 6.10 shows the top, side, and front view from a single molecule on a Cu(111) slap.

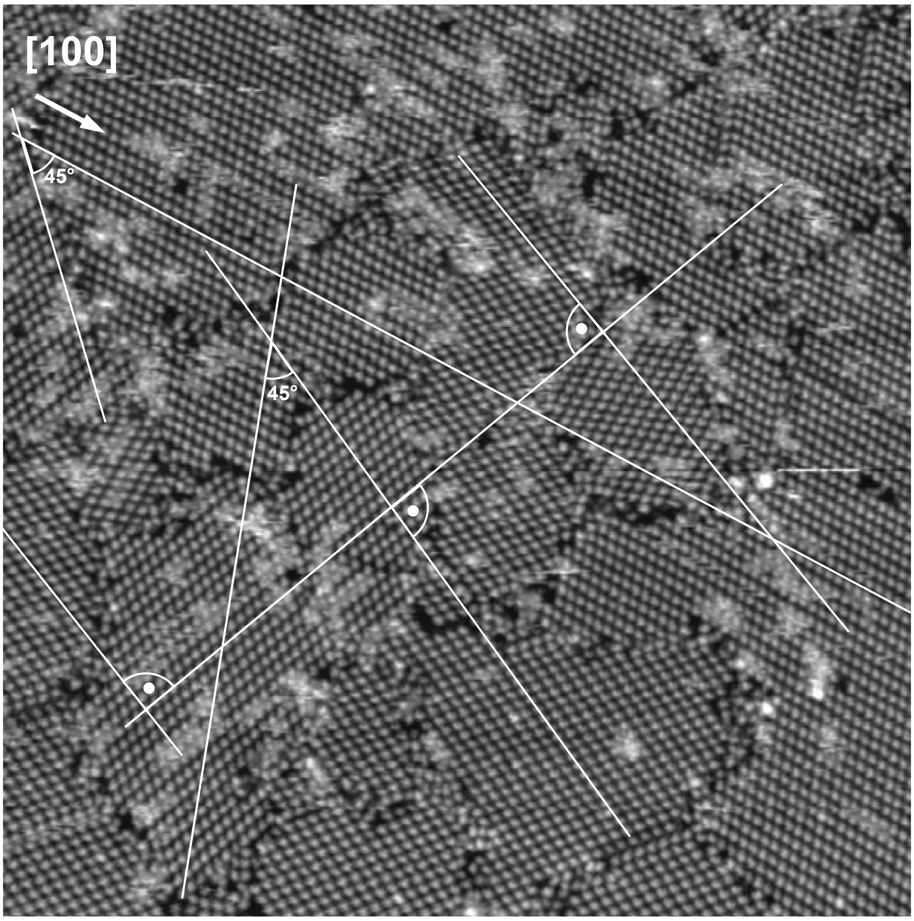

Figure 6.6.: *STM*-image of rotational and mirror domains with a unit cell of (4 0, −1 4) in the monolayer of **6** on Cu(100) ($80 \times 80\,\mathrm{nm}^2$, $-2.513\,\mathrm{V}$, $68\,\mathrm{pA}$, $115\,\mathrm{K}$).

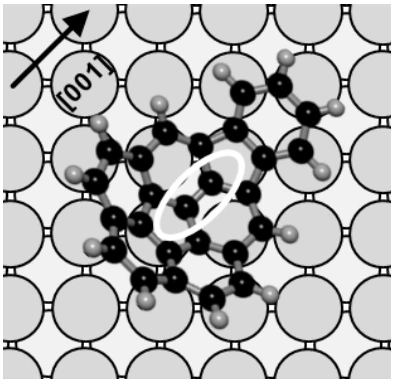

Figure 6.7.: Calculated binding site of mono-indenocorannulene on Cu(100). The bond of the **1**-backbone along the mirror plane ("spoke") adsorbed on a fourfold hollow site of the Cu(100) lattice.

Considering the binding site from the force field calculations (Fig. 6.7), a structure model of the (4 0, −1 4) phase with each molecule adsorbed on top of fourfold hollow sites can be drawn in agreement with the *STM*-image. Figure 6.8 shows a possible arrangement of self-assembled molecules, where the (mirror) symmetry of the molecule is oriented along one of the $\langle 100 \rangle$ symmetry directions of the Cu substrate. The bond in the mirror plane of the **1** moiety is adsorbed on top of a fourfold hollow site.

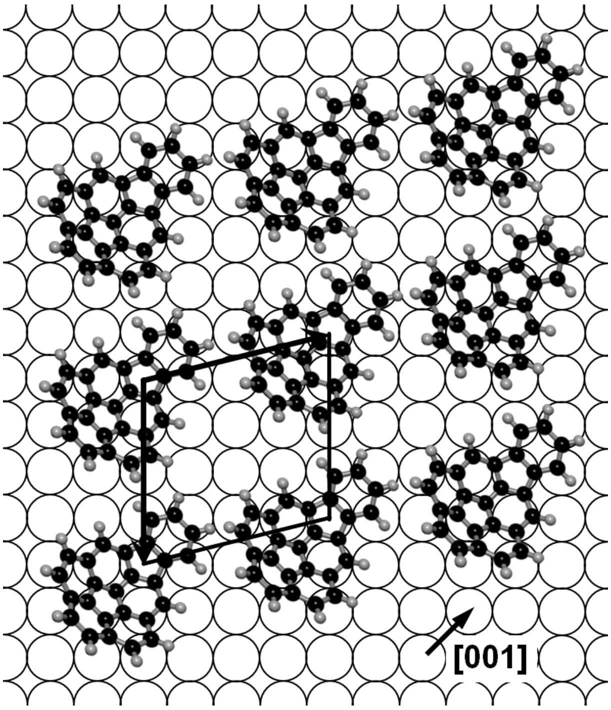

Figure 6.8.: A model of the (4 0, −1 4) domain of mono-indenocorannulene on Cu(100) with superimposed unit cell vectors and placing of the the molecular mirror plane of **6** along the $[001]$ direction of the Cu substrate, according to the calculation.

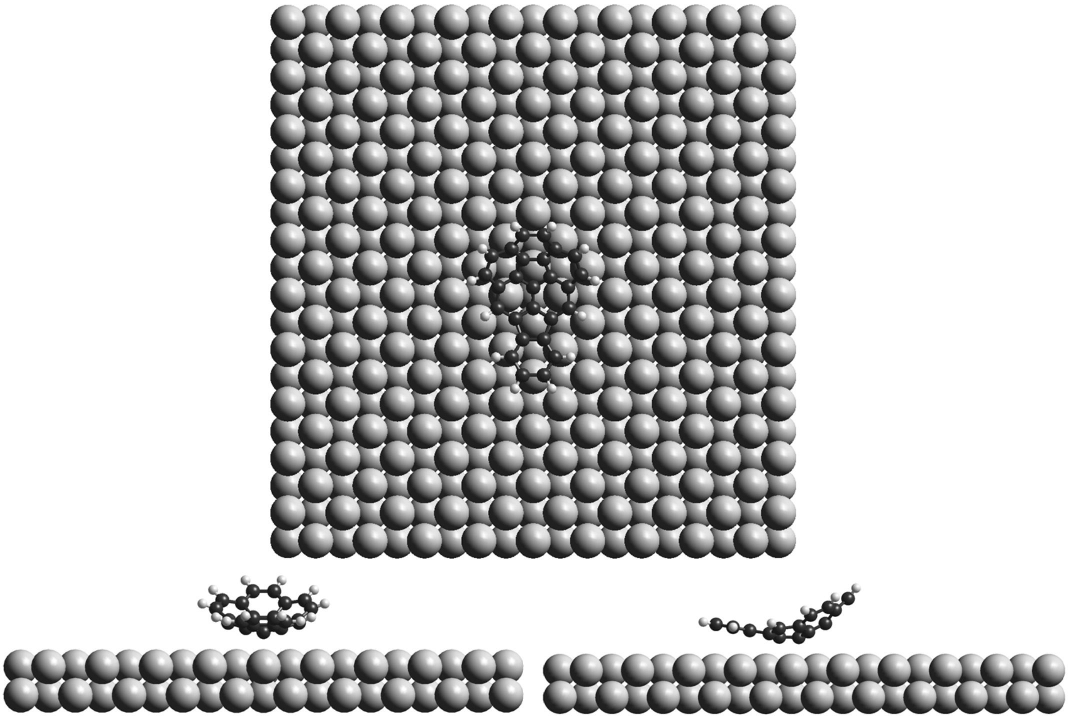

Figure 6.9.: Top, side, and front view of MM+ force field molecular mechanics calculations performed with HyperChem7 of **6** on Cu(100).

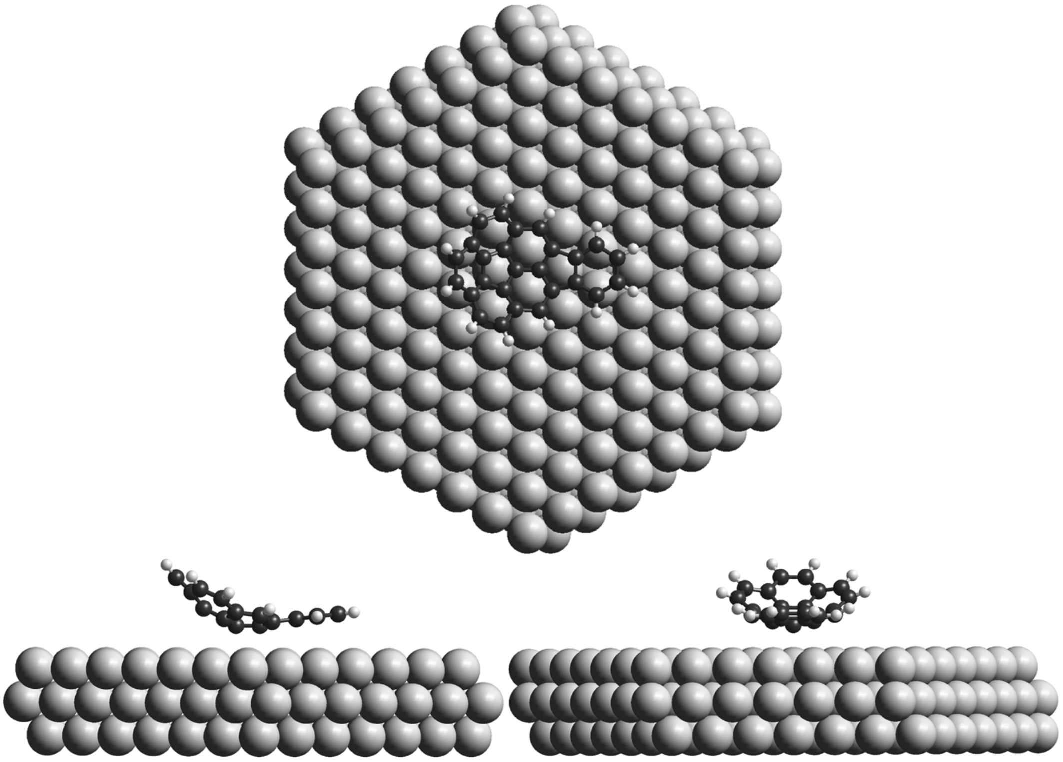

Figure 6.10.: Top, side, and front view of MM+ force field molecular mechanics calculations performed with HyperChem7 of **6** on Cu(111).

Summary:

The reduced symmetry of the **6** molecule relative to corannulene has a profound influence on its *2D* self-assembly crystallization behavior on Cu(111). Mono-indenocorannulene tilts upon adsorption on a Cu(111) surface and is thought to bind with its benzo moiety on top of a threefold hollow site; adsorption of the fivefold symmetric **1**-backbone is suppressed. The resulting zig-zag rows with a unit cell of (5 1,2 7) and the low density phase with a unit cell of (5 0, 4 8) belong to the *p1* crystallographic plane group.
On Cu(100) the binding site of the molecule is different, since the fourfold symmetry only fits to the "spoke"-bond which lies in the mirror plane of the molecule. Therefore **6** seems to adsorb in a parallel state on the Cu(100) substrate. Only one phase with rotational and mirror domains could be observed in the *STM*-experiments. The unit cell of that domain is (4 0, -1 4), which also belongs to the *p1* crystallographic plane group.

Conclusion:

The relative orientation of mono-indenocorannulene on Cu(111) was assumed from the calculated binding site of corannulene and the appearance in the high-resolution *LT*-*STM*-images. From these images the additional benzene moiety of the molecule seems to be parallel to the substrate surface and the azimuthal angle of 30° of the low density phase fits that of the Cu(111) surface symmetry. The six-membered ring is in its minimum potential energy state if adsorbed on top of the threefold hollow sites of the surface. The fourfold surface symmetry of Cu(100) does not fit to any of the ring geometries in the adsorbed molecule. Only the overall mirror symmetry of the molecule is compatible with the geometry of the surface, so the symmetry could therefore be aligned with one of the directions of the Cu(100) surface atoms, as seen in *STM*-images and as suggested from the force field calculations.

7. $C_{32}H_{12}$-buckybowl: self-assembly of a larger C_v symmetric bowl

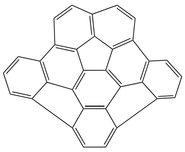

Increasing the bowl-depth of **1** by adding three fused benzo groups at the rim of **1** could induce a bigger tilt of the molecule upon adsorption, which might lead to an increased carbon density on the surface. Although the size of the C_{1v} symmetric **7** bowl is larger than **1**, the density of adsorbed molecules might be higher due to bowl-in-bowl stacking. The effect of the enlarged geometry and reduced symmetry of the molecule on the crystallization behavior in the two dimensional space was investigated with *STM*. $C_{32}H_{12}$-buckybowl molecules were sublimed from a Knudsen cell held at $493\ \mathrm{K}$ onto Cu(111) single crystal surfaces held at room temperature.

In low coverage (~0.7 *ML*) *LT*-*STM*-images (Fig. 7.1) single adsorbed molecules have a C-like appearance, indicating a substantial tilt of the molecule on the surface. This geometry fits best, if the middle six-membered ring of the additional benzo groups is suggested as binding site. Dimers are found in a convex-convex configuration. Densest packed bowl-in-bowl stacked rows appear to be favored only in short range assemblies and could not be observed in larger areas. Larger row assemblies are found to be more stable in a stripe phase with rotations between the next row of molecules (island in the lower part of the image) and are further described below.

Three observed phases of **7** appeared at *RT* and were also stable at *LT* ($\sim 60\ \mathrm{K}$). Figure 7.2a shows a distorted hexagonal arrangement of molecules with a (4 0, -1 4) unit cell. In this phase, every bowl is facing in the same direction; and one molecule covers 16 Cu(111) surface atoms. This phase was found only at low coverage (~0.8 *ML*). The crystallographic group is *p1*. The binding site of the molecule is thought to be the middle benzo group in addition to the corannulene molecule, adsorbed on top of threefold hollow sites of the Cu(111) surface lattice.

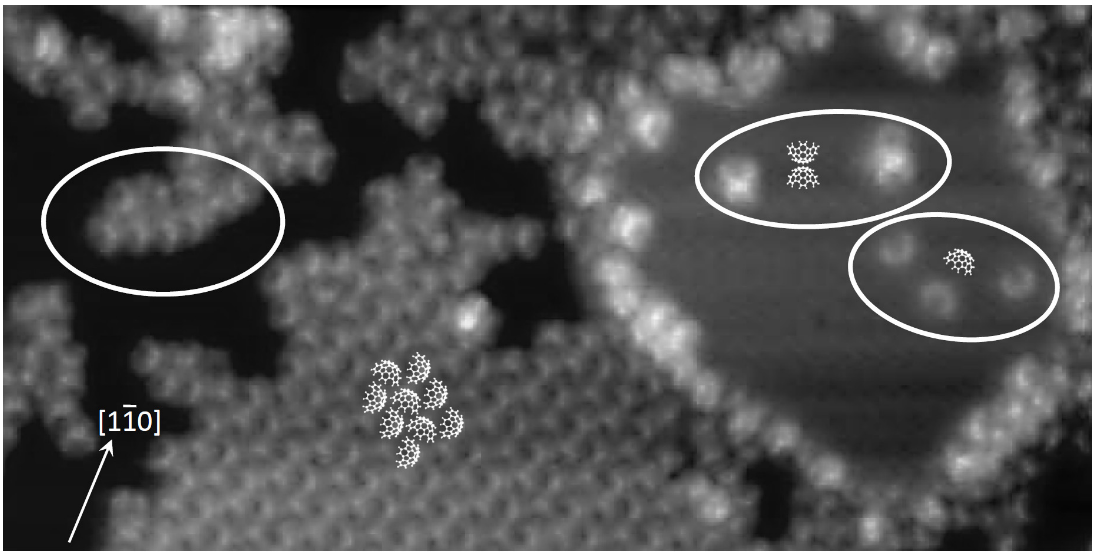

Figure 7.1.: Single adsorption of **7** on Cu(111) indicates an extreme tilt (C-like appearance) and bowl stacking over short-range. A stripe-phase is visible in the middle part of the *STM*-image ($40 \times 20\ \mathrm{nm}^2$, $0.671\ \mathrm{V}$, $0.079\ \mathrm{nA}$, $65\ \mathrm{K}$).

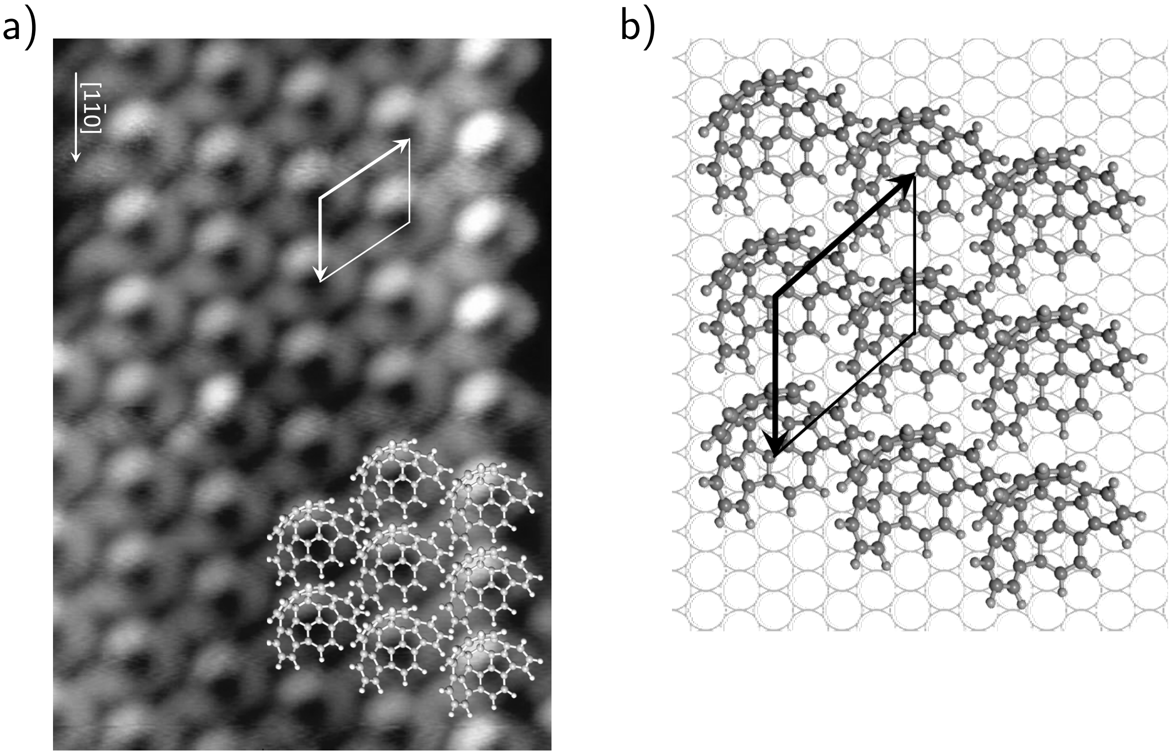

Figure 7.2.: **a)**: *STM*-image of $C_{32}H_{12}$-buckybowl on Cu(111) superimposed with a molecular model structure and highlighted (4 0, −1 4) unit cell ($7 \times 10\ \mathrm{nm}^2$, $-2.565\ \mathrm{V}$, $0.041\ \mathrm{nA}$, $56\ \mathrm{K}$). **b)**: A model of the quasi-hexagonal unit cell, with every bowl pointing in the same direction.

Another phase is shown in the *LT*-*STM*-image in figure 7.3a. Here, in every second row the molecules are showing the same orientation. The molecules of the neighbour rows are azimuthally rotated by $\sim 60°$. All molecules show a clearly highlighted region, and a C-like appearance as observed for single molecule adsorption. The unit cell of this phase was determined to (4 0, 3 7), belonging to the *pg* crystallographic group. A model of the stripe phase, fitting the *STM*-image is shown in figure 7.3b. The binding site of every molecule in the model are the middle additional benzo groups on top of the threefold hollow sites of the substrate. The azimuthal angle of $60°$ is in agreement with the surface geometry. One molecule is covering 14 Cu(111) surface atoms, which is the same molecular density as observed for **1** and **2** after the first phase transition.

In figure 7.4, the *LT*-*STM*-image shows full monolayer coverage. Rotational domains with stripe-wise appearance dominate in this *STM*-image, white lines are drawn to highlight the orientations, which are rotated by $60°$. Next to the stripe phases, disordered molecules are congealed.

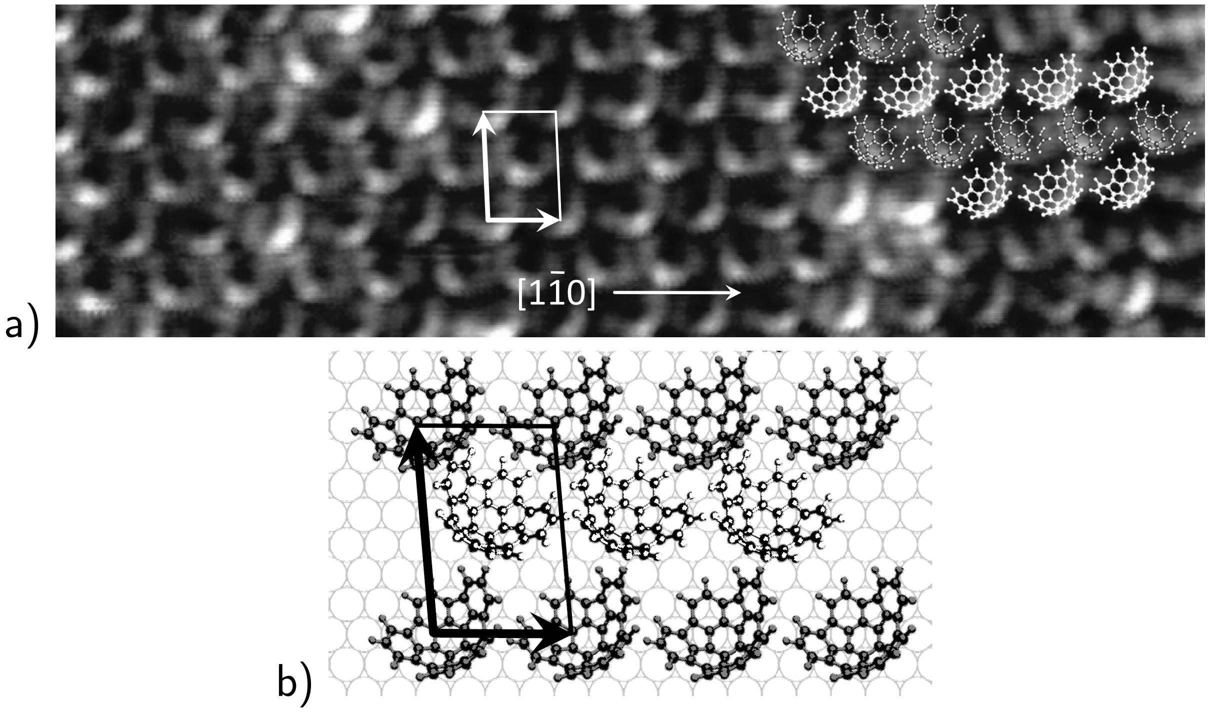

Figure 7.3.: **a)** *LT*-*STM*-image of the stripe phase of $C_{32}H_{12}$-buckybowl on Cu(111) in islands at monolayer coverage. Superimposed are molecular models and the (4 0, 3 7) unit cell vectors. White models are azimuthally rotated by $\sim 60°$ to the gray models ($10 \times 7\,\mathrm{nm}^2$, $-1.162\,\mathrm{V}$, $0.137\,\mathrm{nA}$, $57\,\mathrm{K}$). **b)** A model of the stripe-phase, showing the superimposed unit cell vectors, every other row has the same orientation of the molecules within each row. The middle additional benzo groups of each molecule are placed on top of the threefold hollow sites of the substrate.

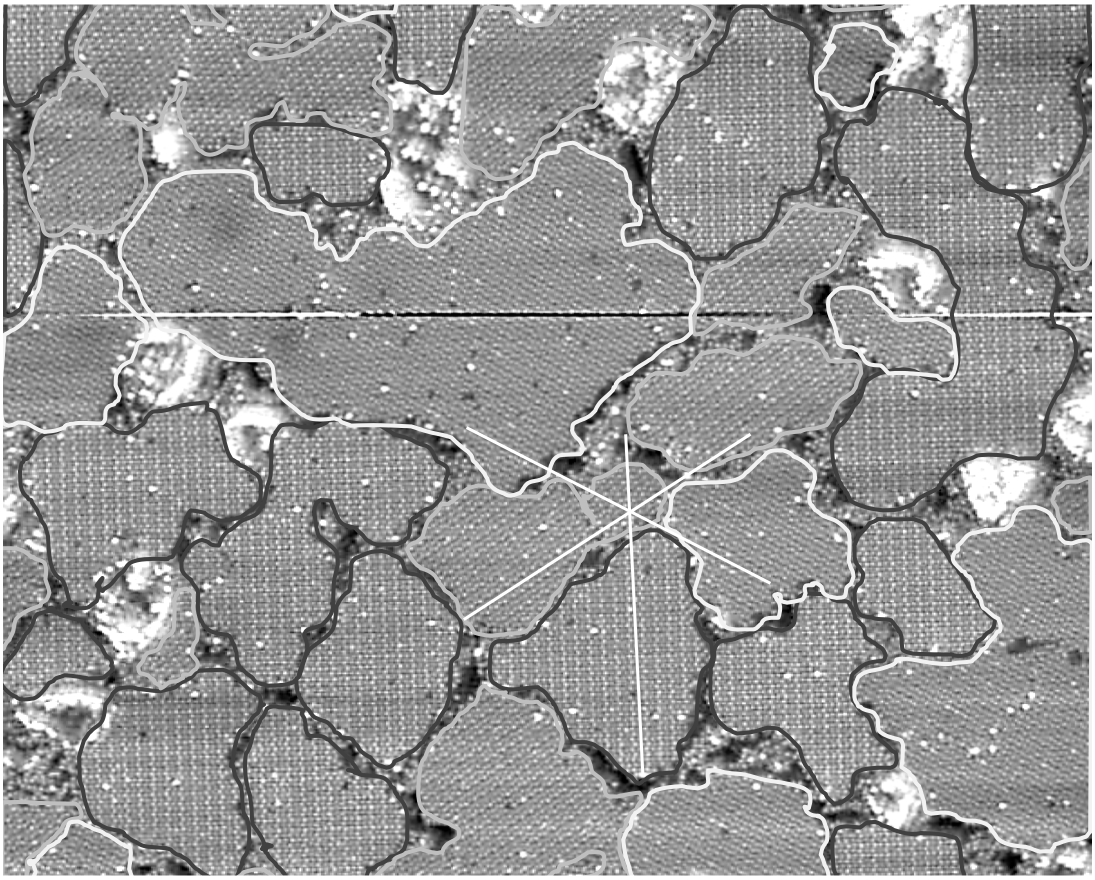

Figure 7.4.: *STM*-image at full monolayer coverage of **7** on Cu(111). Rotational domains of the stripe phase showing a 60° rotational angle ($200 \times 160\,\mathrm{nm}^2$, $1.162\,\mathrm{V}$, $0.137\,\mathrm{nA}$, $57\,\mathrm{K}$). More details on the stripe phase in Fig. 7.3

A third phase was found to coexist beside the stripe phase. Figure 7.5a shows a high-resolution *LT*-*STM*-image of one double-row of molecules with bowls pointing in opposite directions, or in other words having convex-convex bowl stacking. By stacking more of these double-rows beside each other, an anti-stripe phase forms. The appearance of every molecule is again similar to that of the single molecule, indicating the same binding site. A modeled anti-stripe phase fitting the *STM*-image, is illustrated in figure 7.5b. The unit cell of this phase was determined to (4 2, 0 7), with the same density as the stripe phase with one molecule per 14 Cu(111) surface atoms. The crystallographic group of the anti-stipe phase is *pg*, the same as the stripe phase.

Figure 7.6 shows the *LT*-*STM*-image with ∼0.9 *ML* coverage of **7** on Cu(111). Rotational domains (by 60°) of the anti-stripe phase coexist next to island of the stripe phase. Arrows indicate a stripe row embedded within the anti-stripe region.

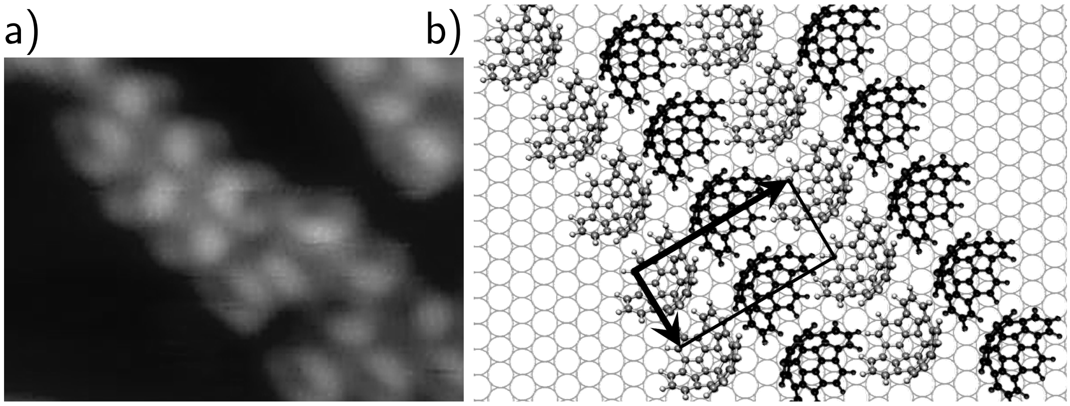

Figure 7.5.: **a)** High-resolution *STM*-image of one double-row of the anti-stripe phase of $C_{32}H_{12}$-buckybowl on Cu(111) (6.5×5.2 nm^2, 0.671 V, 0.079 nA, 65 K). **b)** A model of the (4 2, 0 7) anti-stripe phase. Black and gray models pointing in the opposite direction and are adsorbed with the atoms of the middle six-membered ring on top of threefold hollow sites.

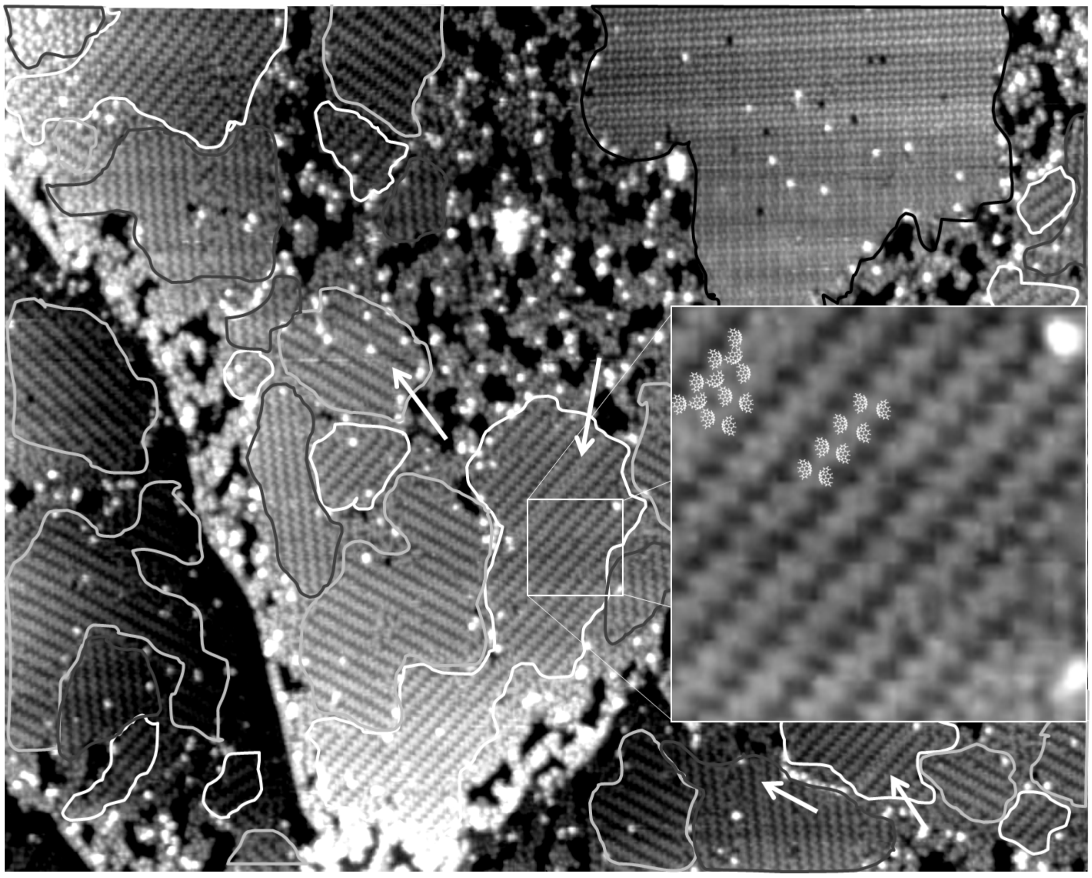

Figure 7.6.: *STM*-image of 0.9 *ML* coverage of **7** on Cu(111) (200×160 nm^2, 1.162 V, 0.137 nA, 57 K). White and gray highlighted areas indicate anti-stripe phases, with rotational angles of 60°. Black highlighted areas indicate stripe phases. White arrows indicate a stripe row within the anti-stripe domain. Insert: zoomed-in region with superimposed models wh

Summary:
A substantial tilt is observed for adsorbed **7**, which forms three different phases. A phase with every bowl opening in the same direction (observed for low coverages at room and low temperature), a stripe phase with an azimuthal angle of 60°, and an anti-stripe phase with bowl opening in the opposite direction (convex-convex orientation) were observed. The rotational angle of 60° within the stripe-phase is consistent with surface symmetry. Only rotational (no mirror) domains could be observed in the *STM*-experiments, which is consistent with the proposed model. The closest possible packing of bowls - the bowl-in-bowl stacking - only leads to very short range structures.
The (4 0, -1 4) phase belongs to the *p1* crystallographic group and the two stripe phases (stripe and anti-stripe) to the *pg* crystallographic group. The stripe phases, with one molecule per 14 Cu(111) surface atoms, have a closer packing than the hexagonal phase, which has one molecule per 16 Cu(111) surface atoms. The molecular surface density of the stripe phases is the same as **1** shows after the first phase transition on Cu(111). However, the related carbon density in the monolayer is much higher for $C_{32}H_{12}$-buckybowl, with 2.29 carbon atoms per Cu surface atom, compared to 1.43 carbon atoms per Cu surface atom for **1** and **2**. Annealing of the sample did not lead to any preferred phases or orientations.

8. $C_{38}H_{14}$-buckybowl: increasing bowl-size with C_{2v} symmetry

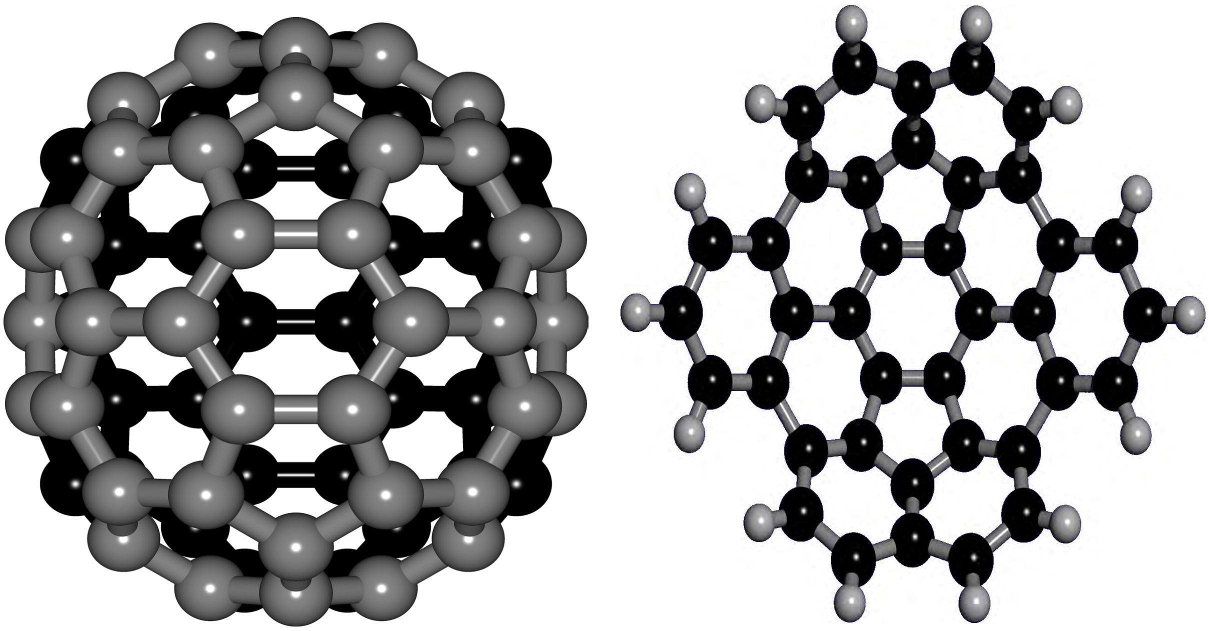

Figure 8.1.: Left: Buckminsterfullerene C_{70} with the highlighted **8** part. **Right**: Carbon-rim atoms of the fullerene-fragment are mono-hydrogenated to give $C_{38}H_{14}$-buckybowl.

As corannulene can be seen as a fragment of C_{60} buckminsterfullerene, so can $C_{38}H_{14}$-buckybowl be seen as a fragment of C_{70} fullerene. This hydrogenated fragment shows C_{2v} symmetry, with two "overlapping" C_5 symmetric **1**-backbones (Fig. 8.1) and a centered six-membered ring. The central six-membered ring should be a preferred binding site due to the symmetry of **8**. Larger bowls adsorbed on the surface might be able to host larger-sized or greater numbers of curved aromatic compounds, which could give rise to new layered structures of organic electronics. The *2D* crystallization of **8** has therefore been investigated with *STM*. $C_{38}H_{14}$-buckybowl molecules were evaporated from a Knudsen cell held at $583\ \mathrm{K}$ for $\sim 5\ \mathrm{min}$ onto the Cu(111) single crystal surface held at room temperature.

In figure 8.2, room temperature *STM*-images of monolayer coverage of **8** on Cu(111) are shown. With the unit cell averaging procedure, as applied for all other investigated molecules, a hexagonal phase with a (5 0, 0 5) unit cell was determined (Fig 8.2a). The Fourier transformation (insert 8.2a) shows the spots which have been taken to determine the unit cell. At room temperatures one molecule covers 25 Cu(111) surface atoms. The inverse *FFT* (insert Fig. 8.2b) show a ring-like appearance of the molecules, indicating that no tilt of the molecules upon adsorption at *RT* is present and all molecules are bowl opening straight up. A ring appearance in the *STM*-image, instead of an elliptic appearance of the molecule could be the result from vibrations of the molecule which averages the height of rim atoms of the molecule above the substrate surface.

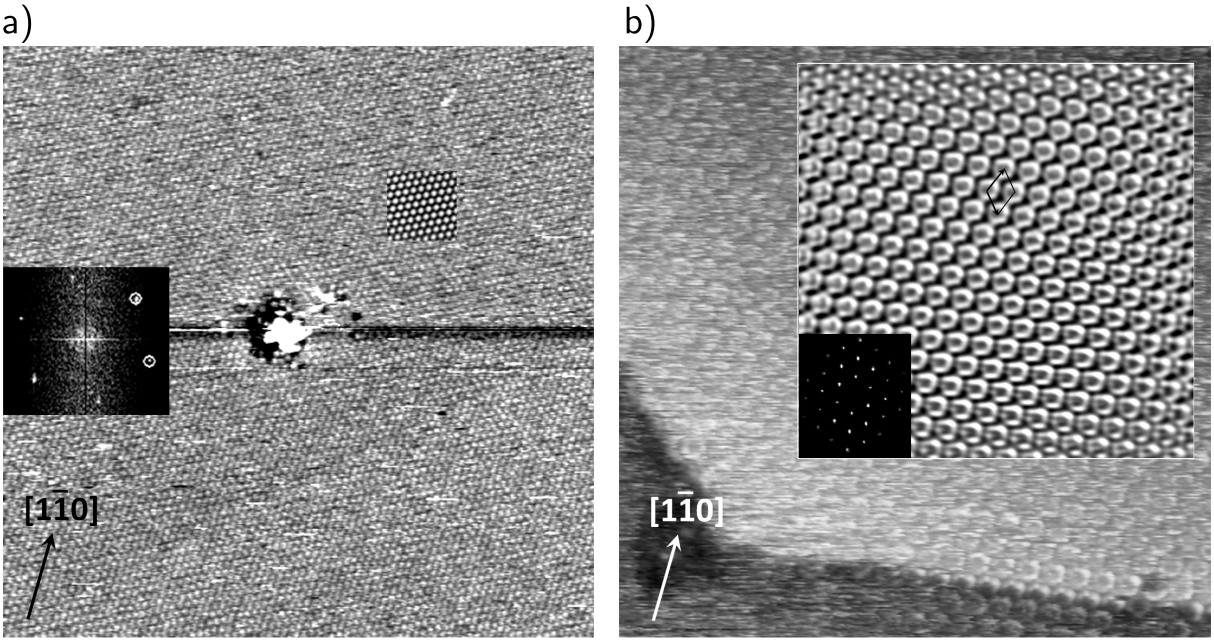

Figure 8.2.: *RT*-*STM*-images of $C_{38}H_{14}$-buckybowl on Cu(111) with a (5 0, 0 5) unit cell. **a)** $100 \times 100\ \mathrm{nm}^2$, $1.970\ \mathrm{V}$, $149\ \mathrm{pA}$; insert $11.7 \times 11.7\ \mathrm{nm}^2$ averaged over 4204 positions. **b)** $30 \times 30\ \mathrm{nm}^2$, $-0.248\ \mathrm{V}$, $946\ \mathrm{pA}$; lower-left insert: Fourier transformation of the upper-right terrace with highlighted spots which have been used for determine the unit cell vectors. upper-right insert: inverse *FFT*-image ($20 \times 20\ \mathrm{nm}^2$ determined from that region by the *FFT*-spots indicated) revealing the bowl opening straight up adsorption; the whole molecule shows a ring appearance.

However, by taking a series of images into account only an averaged unit cell can be determined. The STM image, and also the *FFT* unit cell determination, appears to indicate a (5 0, 0 5) unit cell. Drawn models (Fig. 8.3) in order to fit a (5 0, 0 5) periodicity on the other hand indicate that adjacent molecules must be rotated 120° from each other in order to minimize steric hindrance of the rim atoms. This azimuthal rotation of neighboring molecules, which could not be identified by the Fourier transformation, can also be found in some regions in the

STM-image (Fig. 8.4, lines indicate the orientation of the molecules). Determined from the drawn models, the actual unit cell would be (10 5, −5 5), belonging to the *p3* crystallographic group. If all the molecules were adsorbed in the same direction, an elongated unit cell would have to form; however, this was not observed and may be the result from the averaging procedure.

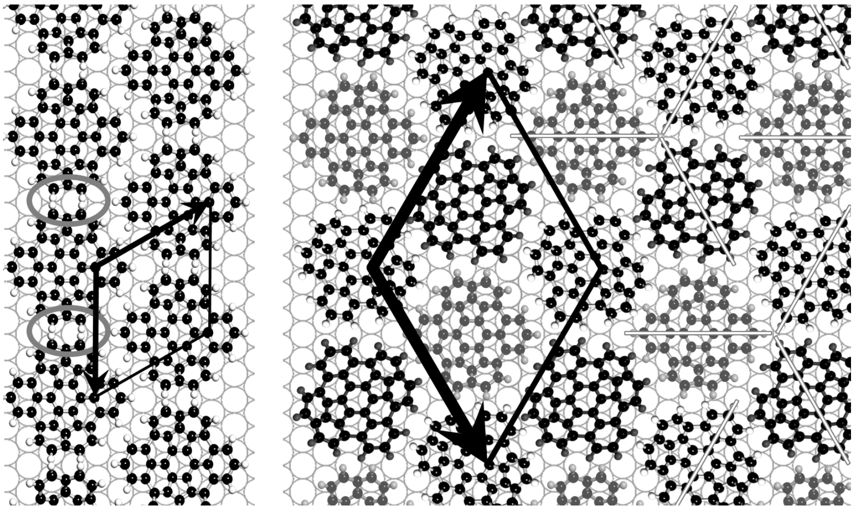

$\begin{pmatrix} 5 & 0 \\ 0 & 5 \end{pmatrix}$ $\begin{pmatrix} 10 & 5 \\ -5 & 5 \end{pmatrix}$

Figure 8.3.: A model shows that adsorbed $C_{38}H_{14}$-buckybowl on Cu(111) at *RT* prefers a bigger (10 5, −5 5) unit cell containing three molecules, rotated by $120°$ instead of a (5 0, 0 5). The steric hindrance of the molecules in the (5 0, 0 5) unit cell is indicated with overlayed ellipses. All molecules are placed with their centered six-membered ring on top of threefold hollow sites. Lines are drawn to show the orientation of the molecules.

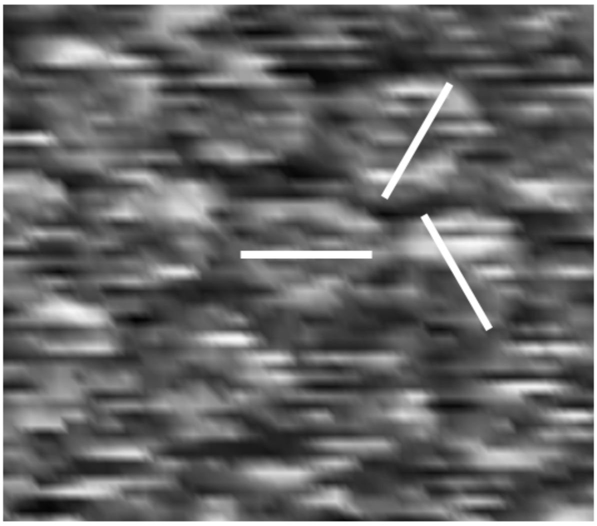

Figure 8.4.: *STM*-image ($4.7 \times 4.1\,\mathrm{nm}^2$) of a region from figure 8.2b. Lines indicate the orientation of the molecules. Neighboring molecules show a azimuthal rotation of $120°$.

Figure 8.5 shows the *STM*-image of the "(5 0, 0 5)" layer cooled to $60\,\mathrm{K}$. Now, an asymmetry of the molecules can be seen, indicating a tilt of the molecule upon cooling. Here, the *LT*-*STM*-image for a full *ML*-coverage show always random short-range stripe-wise appearance.

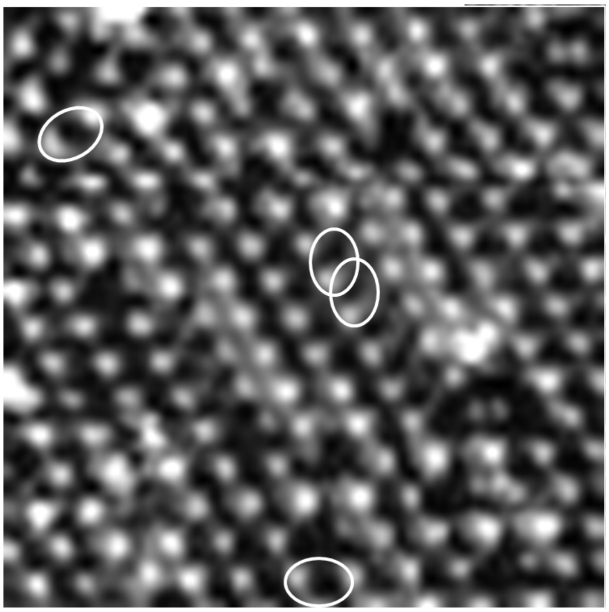

Figure 8.5.: Low temperature *STM*-images of $C_{38}H_{14}$-buckybowl on Cu(111) showing short-range stripe-like structures ($15 \times 15\,\mathrm{nm}^2$, $1.423\,\mathrm{V}$, $253\,\mathrm{pA}$, $61\,\mathrm{K}$). Ellipses highlight tilted molecules oriented in different directions.

To explore the reason of the tilting of the molecules during cooling, the crystallization behavior at sub-monolayer coverage was investigated. More detailed structures for sub-*ML*-coverage (∼0.6 *ML*) are recognizable at *LT* (Fig. 8.6). The *STM*-image shows single molecules, dimers, line formation and island of molecules forming an interesting structure.

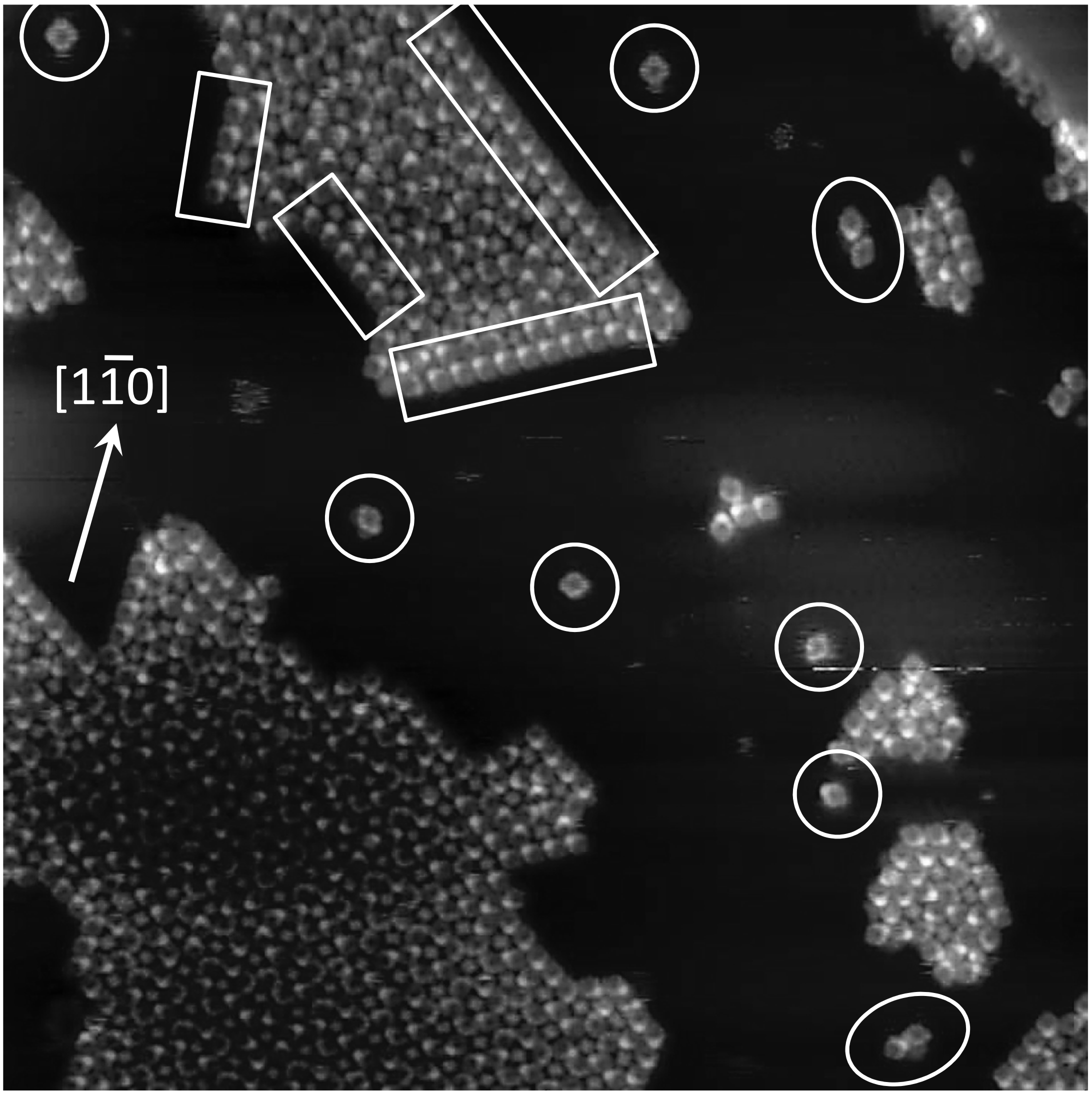

Figure 8.6.: Some characteristic **8** adsorption structures are formed at *LT* on Cu(111). Single molecules (highlighted with rings), tilted dimers (highlighted with ellipses), line formations (highlighted with rectangles) and a rosette phase (lower left part and more details in Fig. 8.8) occur (*STM* parameters: $60 \times 60\,\mathrm{nm}^2$, $0.699\,\mathrm{V}$, $168\,\mathrm{pA}$, $61\,\mathrm{K}$).

Figure 8.7 shows high-resolution *STM*-images and models of the molecules. The appearance of single molecules indicates an adsorption with its centered six-membered ring. The two highlighted regions at the front and back of the molecule can be assigned as the six-membered rings of the benzo moiety (Fig. 8.7a). The two elongated highlighted regions at the left and right side of the molecule can be assigned as the two six-membered rings of the naphthalene moiety of the molecule.

As two molecules approach each other (Fig 8.7b), they are observed to tilt either away from or towards each other. The selected example shows two molecules with an azimuthal rotation of $120°$; only one is tilted (the black arrow indicates the direction of tilt with a rotation around the y-axis of the molecule, the arrow head shows the part of the molecule which is protruding upwards, the origin of the arrow the part which is closest to the surface; the line is indicates the x-axis of a not tilted molecules). With increasing density, lines of molecules with the same tilt and same orientation are formed, which show stacked bowl molecules (Fig 8.7c).

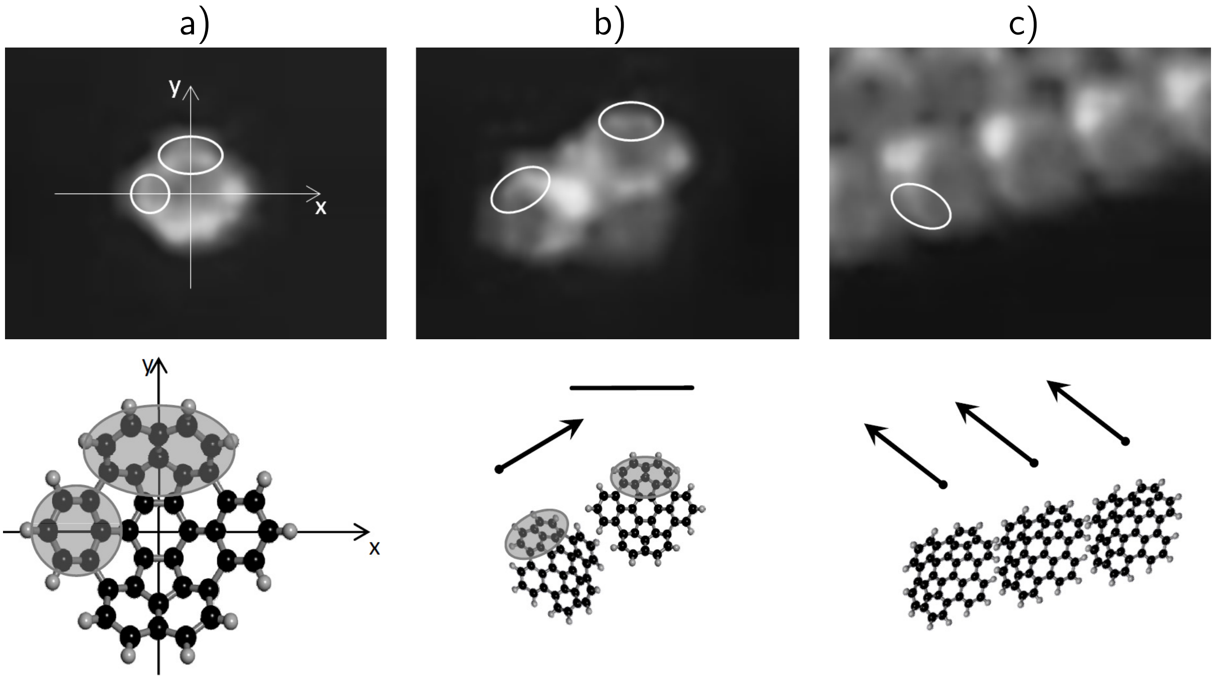

Figure 8.7.: Sub-monolayer coverage adsorbed molecules show: **a)** single molecule with highlighted benzo group along the x-axis and two highlighted benzo groups of the naphthalene moiety on the left and right side of the molecule. A darker area in the middle of the molecule and the same intensity of the front and back, left and right side of the molecule indicates an bowl opening up adsorption with the centered six-membered ring. **b)** Dimers with one tilted and one not tilted molecule. The black arrow indicating the direction of tilt around the y-axis with the arrow head showing the upwards protruding part of the molecule. The line indicating the orientation or the x-axis of a non-tilted molecule. The two benzo groups of the naphthalene moiety are highlighted. **c)** A row of molecules with part of the bowls stacking (*STM*-image parameters: $5.3 \times 4\ \mathrm{nm}^2$, $0.699\ \mathrm{V}$, $168\ \mathrm{pA}$, $61\ \mathrm{K}$).

At low coverage, islands showing a interesting structure are found to congeal at low temperature (lower left section within the *STM*-image, Fig. 8.6). Figure 8.8 reveal the basic building blocks of this phase. In the middle of each gearwheel, as well as in between the gearwheels, molecules with bowl opening down adsorption are found (appearance as a dome in the *STM*-image). Around these upside-down molecules, left and right handed structures of molecules are found.

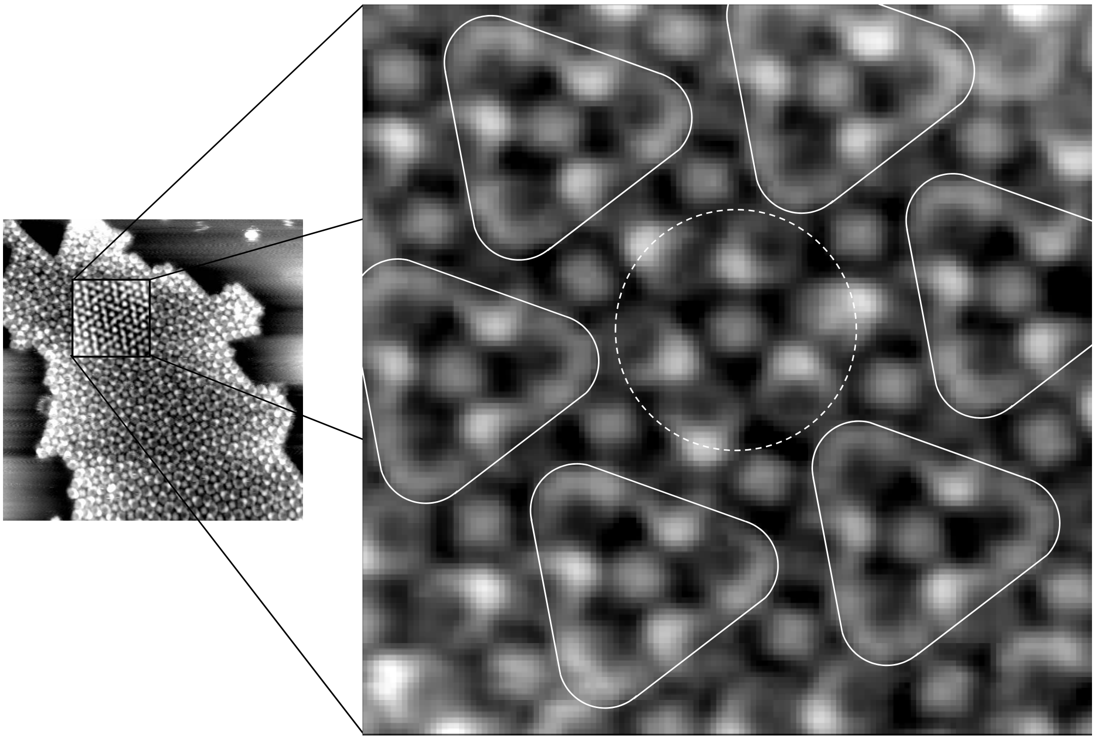

Figure 8.8.: *STM*-image of the rosette phase of $C_{38}H_{14}$-buckybowl on Cu(111) ($40 \times 40\,\mathrm{nm}^2$, $0.699\,\mathrm{V}$, $168\,\mathrm{pA}$, $61\,\mathrm{K}$, insert averaged over 308 positions).The enlarged image ($10 \times 10\,\mathrm{nm}^2$) showing a centered left-handed gearwheel hexagonal surrounded by right-handed gearwheels. The centered molecule of each gearwheel as well as the "space filling" molecules in between are pointing bowl opening down. Molecules adsorbed with their naphthalene part and molecules adsorbed with their benzo groups contributing to the gearwheel structures (for more details see Fig. 8.9 and Fig. 8.11).

More details of the centered left handed gearwheel is shown and explained in figure 8.9. In the center, a molecule with bowl opening down adsorption is surrounded by three molecules (each rotated by $120°$) tilted around the y-axis and adsorbed with their benzo group. The bowl opening of these molecules is away from the center. Three other molecules (each rotated by $120°$) are also adsorbed with their benzo group, but the bowl opening is towards the center. A side view model of a cross-section is shown in figure 8.10, with the centered bowl molecule opening down, the left bowl opening towards the centered molecule, and the right bowl opening away from the centered molecule.

The right handed gearwheel is shown and explained in figure 8.11. Three tilted molecules adsorb with their naphthalene group and three with their benzo group around a centered bowl opening down molecule, to form the right handed gearwheels (seen in the *STM*-image as either the long or short side of the molecules protruding upwards, indicated as black and gray molecules in the model, gray arrows indicating a tilt around the x-axis, the arrow head the part of the molecule which is protruding upwards). The molecules adsorbed with their benzo group are "leaning" against the center, meaning the bowl opens away from it. The rosette appearance, composed of left and right handed gearwheels, is also shown with a model (Fig. 8.13).

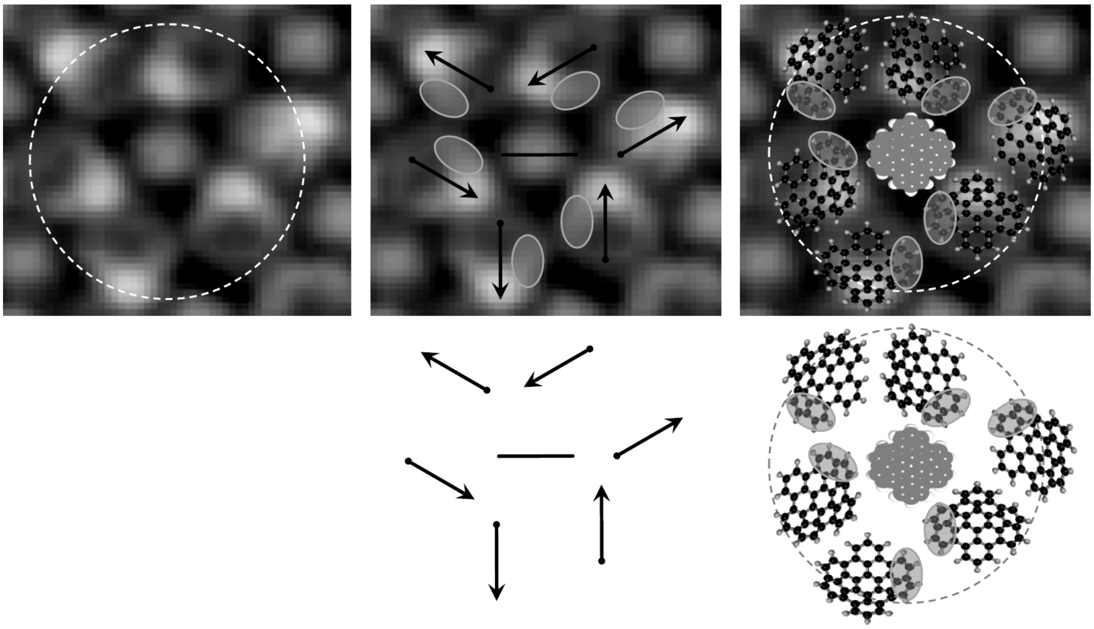

Figure 8.9.: Left-handed building block of the rosette phase. Black arrow indicate tilt around the y-axis of the molecule with the head of the arrow pointing towards the benzo moiety protruding upwards. The two benzo moieties of the naphthalene part on the left side of the molecules are highlighted with ellipses. Models are superimposed in agreement with the *STM*-image, three molecules rotated by $120°$ "leaning" against the center molecule and three facing away (see side view in Fig. 8.10). The orientation of the centered bowl opening down molecule is arbitrarily chosen.

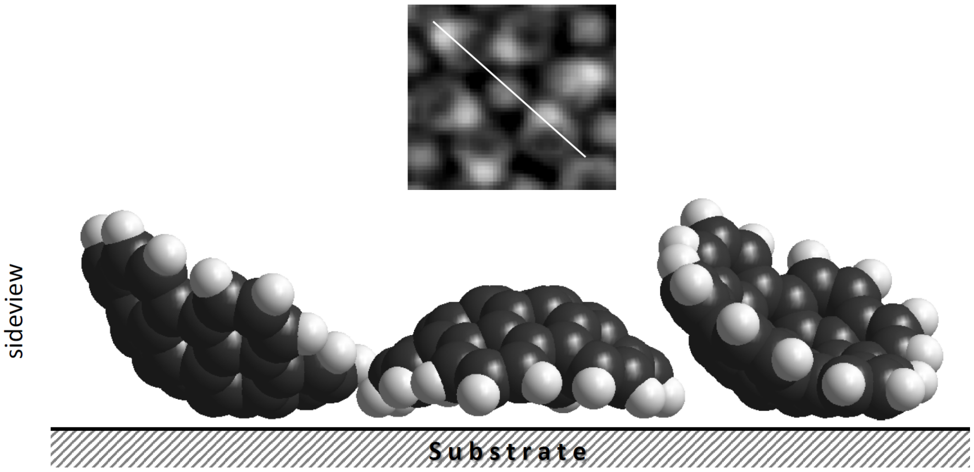

Figure 8.10.: A side view model of the left handed gearwheel (marked with a line in the *STM*-image). Centered molecule opening down, one bowl open away the other one towards the center.

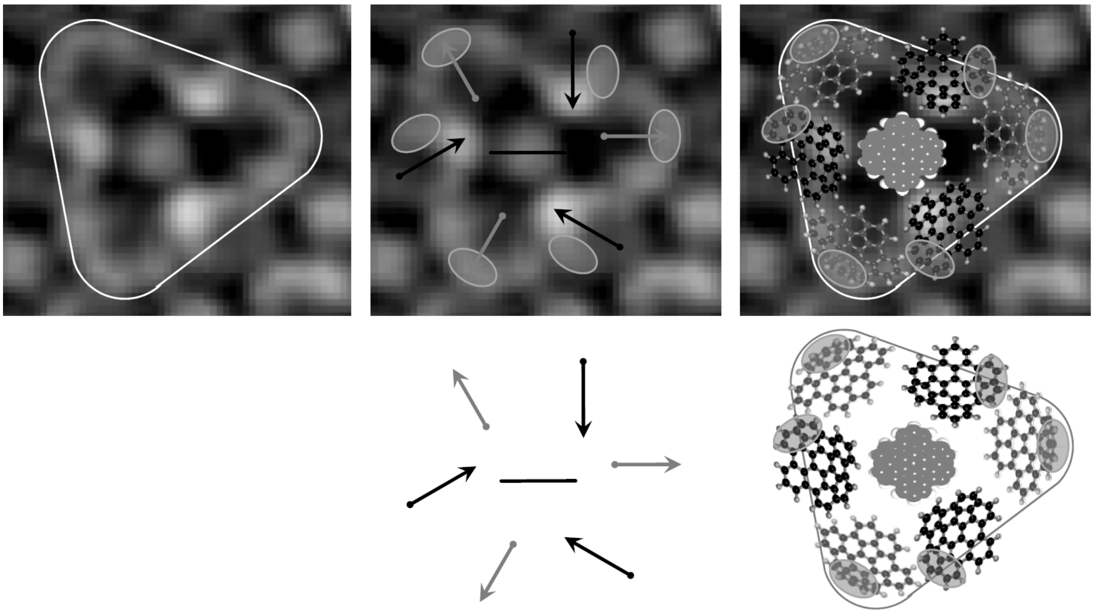

Figure 8.11.: Right-handed building block of the rosette phase. Black arrow indicate tilt around the y-axis of the molecule with the head of the arrow pointing towards the benzo moiety protruding upwards. Gray arrow indicate tilt around the x-axis of the molecule with the head of the arrow pointing towards the two benzo groups of the naphthalene moiety protruding upwards. the two benzo moieties of the naphthalene part on the left side of the molecules are highlighted with ellipses. Models are superimposed in agreement with the *STM*-image, three molecules rotated by $120°$ "leaning" against the center molecule and three away. The orientation of the centered bowl opening down molecule is arbitrarily chosen.

The determination of the unit cell of the rosette phase was done in a different way than for the rest described in this thesis. Only two consecutive images (in order to compensate thermal and mechanical drift in the *STM*-images) are taken into account for the determination of the unit cell. The angles $\alpha_1 \ldots \alpha_5$ (indicated in figure 8.12) and the lengths $L_1 \ldots L_{12}$ were measured (see Table 8.1). A Cu-Cu surface atom distance of $0.2553\,\mathrm{nm}$ was used for the determination of the unit cell for the rosette phase, which is a (27 0, 0 27) unit cell. Some molecules, especially within the left handed gearwheels and towards the boarder of the islands are aligned in the wrong direction, but the majority of the molecules are aligned according to the shown unit cell.

The full dimension of this extraordinary phase, in which 10 molecules point face down and 19 tilted molecules facing up to make a total of 29 molecules per unit cell, is shown in figure 8.13. Circles indicating the left handed gearwheel building blocks and triangles indicating the right handed gearwheels as they built up this phase.

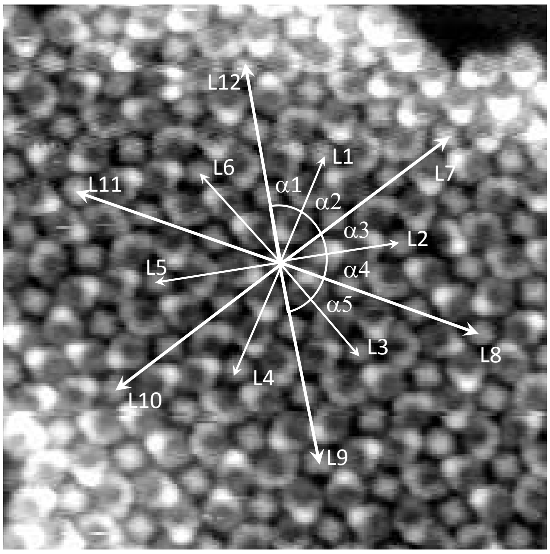

Figure 8.12.: Measured lengths and angles of two consecutive images to determine the (27 0, 0 27) rosette unit cell ($17\text{x}17\ \mathrm{nm}^2$, $0.699\ \mathrm{V}$, $168\ \mathrm{nA}$, $61\ \mathrm{K}$).

Table 8.1.: Lengths and angles of Fig. 8.12.

Angle [°] Length [nm]	Image M523	Image M524	Average
α_1	33.3	26.7	30.00
α_2	30.9	29.8	30.35
α_3	28	30.6	29.3
α_4	28.5	32.1	30.3
α_5	31.3	29.4	30.35
Average			30.06
L_1	3.55	4.43	3.99
L_2	3.96	3.89	3.93
L_3	3.88	4.11	3.99
L_4	3.62	4.12	3.87
L_5	4.05	3.87	3.96
L_6	3.89	4.00	3.95
Average			3.95
L_7	6.54	7.07	6.81
L_8	6.80	6.76	6.68
L_9	6.52	6.95	6.74
L_{10}	6.60	7.02	6.81
L_{11}	6.78	6.89	6.84
L_{12}	6.12	7.42	6.79
Average			6.79

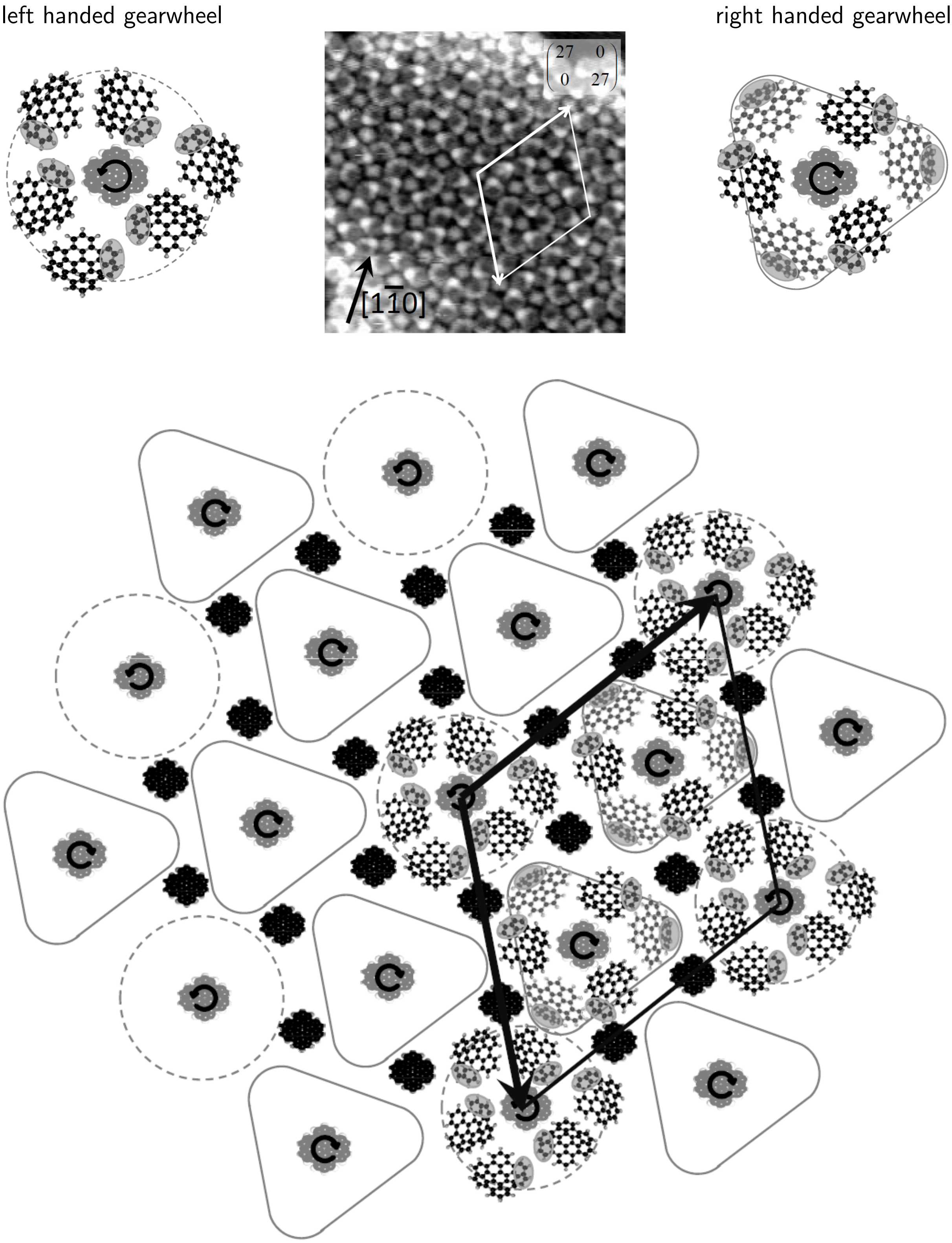

Figure 8.13.: Rosette phase of $C_{38}H_{14}$-buckybowl on Cu(111) at *LT*. **Upper:** Models of the left and right handed gearwheel and superimposed (27 0, 0 27) unit cell vectors in the *STM*-image ($17 \times 17\ \mathrm{nm}^2$, $0.699\ \mathrm{V}$, $168\ \mathrm{pA}$, $61\ \mathrm{K}$). **Lower:** A model of the hexagonal rosette phase.

Figure 8.14 shows a island of the second layer. Long range rows of molecules are adsorbed on top the layer underneath, which as cooled monolayer shows only short range ordered rows. Second layer deposition at room temperature and subsequent cooling to low temperature ($63\ \mathrm{K}$) of the sample seem to stabilize a stripe formation of the layer underneath. The unit cell of the second layer was determined to a (4 0, 4 9). First layer molecules next to the second layer show the same unit cell. The coverage in the first monolayer is one molecule per 18 Cu(111) surface atoms, which is $39\ \%$ more densely packed than in the hexagonal monolayer with one molecule per 25 Cu(111) surface atoms. Tilted molecules with a bowl-in-bowl stacking are assumed to form the overlayer (tilted molecules are visible at the edge of the second layer).

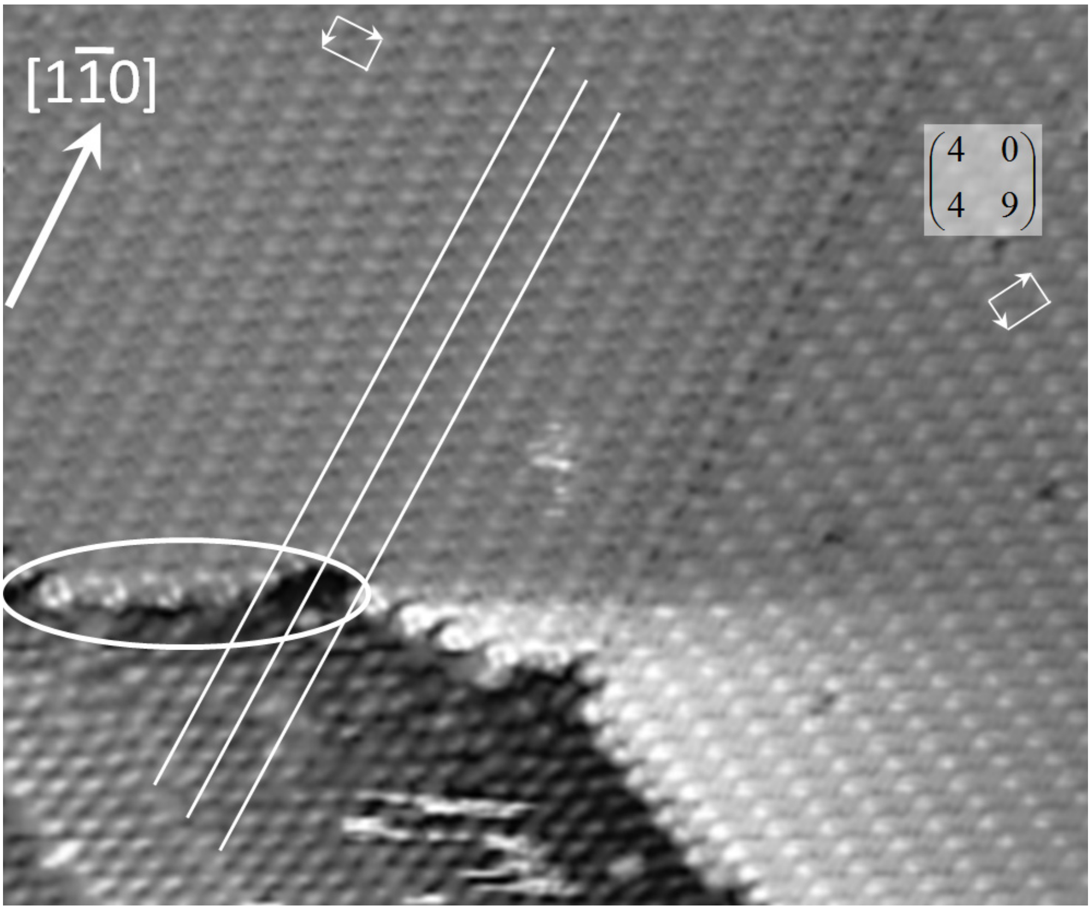

Figure 8.14.: Second layer of $C_{38}H_{14}$-buckybowl on Cu(111). Three rotational domains with a rotational angle of 60° and superimposed unit cell of (4 0, 4 9) are shown. Second layer edge molecules (highlighted with white ellipse) are tilted bowl facing up (*STM*-image $44 \times 37\ \mathrm{nm}^2$, $-1.395\ \mathrm{V}$, $303\ \mathrm{pA}$, $63\ \mathrm{K}$).

Summary:

Due to the six-membered ring in the center of **8**, the molecule has a preferred single molecule, bowl opening up, hexagonal adsorption on Cu(111). While *STM* shows a (5 0, 0 5) unit cell, a drawn model indicate that a bigger (10 5, -5 5) hexagonal unit cell with a $120°$ azimuthal rotation between adjacent molecules on the surface are preferred. During cooling, recognition between neighboring molecules results in substantial tilting of both molecules either by concave-convex bowl-stacking or convex-convex complex building, as obvious from the asymmetric appearance in *STM*. Low coverage *LT*-*STM*-images show all four possible orientations of **8** towards the surface, summarized in figure 8.15: a bowl opening up absorption on the centered six-membered ring, two tilted adsorptions, one on the two benzo groups of the naphthalene moiety of the molecule resulting in a tilt along the x-axis, the other on the benzo moiety of the molecule resulting in a tilt along the y-axis, and a bowl opening down adsorption. Molecules adopting three of the four observed adsorption modes construct the rosette-phase (27 0, 0 27) in which 10 molecules point face down and 19 tilted molecules facing up to make a total of 29 molecules per unit cell (Fig. 8.13). The second layer of **8** forms a (4 0, 4 9) stripe phase. The room temperature hexagonal phase and the rosette phase show the same surface density of one molecule per 25 Cu(111) surface atoms. A $39\,\%$ density increase to one molecule per 18 Cu(111) surface atoms is observed in the tilted row phase after stabilization with a second layer.

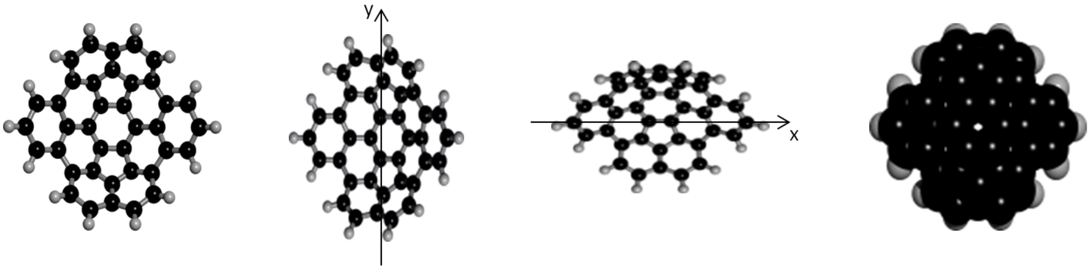

Figure 8.15.: The four different adsorption modes of **8** on Cu(111). From left to right: bowl opening up with the centered six-membered ring on top of threefold hollow sites of the substrate. Tilt around the y-axis with the benzo group as b

9. Summary & Conclusion

The adsorption and self-assembly behavior of bowl shaped hydrocarbon molecules ('buckybowls', Fig. 1.1) on *2D*-surfaces were studied. Cu(111) and Cu(100) single crystal substrates, which display threefold and fourfold surface symmetry respectively, were used. The self-assembly of bowl shaped molecules is difficult to predict as the bowls can tilt upon adsorption, and interesting patterns occur as a result of interaction between neighboring molecules. Another aspect studied in this thesis is the influence of fivefold symmetry in the self-assembly behavior. It is still not fully understood how fivefold symmetric molecules crystallize in a plane.

Influence of substituesnts on adsorption and symmetry.
One aspect studied in this thesis was the influence of fivefold symmetry on self-assembly behavior. Prior to these studies, it was still not fully understood how fivefold symmetric molecules crystallize in a plane. Thus, the work described in this thesis examined a set of molecules with a fivefold symmetric backbone. Functional groups were introduced at the rim of the molecule to:

1. induce chirality in the molecule,
2. change the vibrations of the molecule via heavy-atom substitution,
3. induce steric hindrance, and
4. reduce the fivefold symmetry of the molecule to a twofold or mirror symmetry.

Previous studies showed that fivefold symmetric molecules can self-assemble into *2D* crystals (Chapter 3). Self-assembly of fivefold symmetric objects is less favorable than with other symmetries. Fivefold-symmetric self-assembly is bypassed - if possible - by e.g. tilting or interdigitation. To illustrate, corannulene interacts with the surface as it tilts upon adsorption towards one of its five six-membered rings, which circumvents the expression of its fivefold symmetry upon adsorption. Interaction with neighboring molecules results in two 2D reversible phase transitions. The phase transitions are thought to be caused by bowl-breathing vibrations, which leads to migration of the molecule from an *fcc* to an *hcp* zig-zag zipper-like migration from the *RT* to the (4 0, 3 7) to the *LT* phase and back.

To determine if a change in the molecular vibrations has an influence on the phase transitions and self-assembly behavior, we prepared Perdeutero-corannulene (**2**, Chapter 4), expecting that the change from hydrogen to deuterium rim substituents would affect the temperature of its phase transitions. However, no change in the phase transition could be observed, perhaps because it may be too small to be detectable with *STM* experiments. The epitaxial bowl-in-bowl second-layer growth of **2** was also found to be identical to that of **1**.

Previous studies of chiral, penta-substituted molecules (**3**, **4**) demonstrated that their functional groups induced a steric hindrance between the molecules and the substrate surfaces. This steric hindrance forces the substituted corannulene into a parallel orientation relative to the surface and therefore induces the molecule to express its fivefold symmetry. A bowl-to-bowl inversion of the molecule is not allowed after adsorption due to the loss of one degree of freedom. This leads to an averaged 50:50 adsorption of each enantiomer on the surface.

We expected that due to the chirality of substituted corannulene molecule, different phases should form after the self-assembling process on the surface. However, so far no chiral expression of the molecules in the crystallization behavior was found. Pentaphenyl-corannulene (**5**, Chapter 5), with its bigger functional groups, was expected to display its chirality. However, from the *STM*-images the chirality of the molecules could not be determined. It can be assumed that the two phases are built up by either heterochiral or homochiral molecules. One of the phases is arbitrarily chosen to be heterochiral and the other homochiral. As the antiparallel stripe phase observed for **3** and **4** is the closest possible packing for antiparallel hard pentagons, so the antiparallel stripe (7 6, −5 6) phase observed for **5** is most likely the closest possible packing for hard stars. Pentaphenyl-corannulene shows interdigitation between its phenyl groups, which seems to be the driving force for close-packing in very low coverages.

Self-assembly of fivefold symmetric objects is less favorable than with other symmetries. Fivefold-symmetric self-assembly is bypassed - if possible - by e.g. tilting or interdigitation. If fivefold symmetry is unavoidable, macroscopic ordered regimes dominate molecular structures. If no steric hindrance is built within the molecule (as it was previously recognized for **1**, and demonstrated herein for **2**) a substantial tilt is observed in order to make a closer packing possible and to avoid fivefold-symmetric adsorption. Steric hindrance at the edge of the molecules (as for the previous studies of **3**, **4**, and herein for **5**) suppresses the tilt of the molecules. The fivefold-symmetric absorption is avoided by formation of rotatory- and stripe-phases, and in the case of **5**, interdigitation and overlapping of its phenyl substituents.

Another experiment was designed to get information about the thermal stability of the adsorbed molecular lattice and the electronic properties. *TPD*-experiments showed that dehydrogenation of **5** occurred at $563\,\mathrm{K}$, which indicates that this molecule is more stable upon adsorption than **1** (by $60\,\mathrm{K}$) and has similar stability to **4** (which shows dehydrogenation at $543\,\mathrm{K}$ and $620\,\mathrm{K}$). The calculated dipole moment of **5** is $3.4\,\mathrm{D}$, which is independent of temperatures since this molecule does not undergo any phase changes. The interfacial dipole moment is lower than that of **1** and **4** on Cu(111) and Cu(100) at RT and LT. Also the observed maximum work function change is with $\Delta\phi_{max} = 1.16\,[eV]$ lower than that for **1** and **4** on Cu(111) and Cu(100).

Adsorption of twofold and mirror symmetric buckybowls.
The fundamental understanding of different adsorption orientations and the two-dimensional crystallization behavior of organic, aromatic molecules on various metal surfaces is crucial for the development of new organic electronics and the optimization of their properties. The bowl shaped **1** was already shown to be an interesting molecule in self-assembly behavior, with adjustable phases and surface properties. Therefore, we also investigated the larger and deeper bowl-shaped mono-indenocorannulene, $C_{32}H_{12}$-buckybowl, and $C_{38}H_{14}$-buckybowl compounds.

The largest molecular bowl under investigation (**8**, Chapter 8) is twofold symmetric and was expected to express its symmetry after adsorption. Indeed, at room temperature, **8** showed a hexagonal phase with bowl opening up adsorption on its central six-membered ring. Drawn models and local areas in the STM-image indicate that due to minimizing of steric hindrance and maximizing in surface density, a phase in which every neighboring molecule is rotated by $120°$ is likely. During cooling a surface density increase of $39\,\%$ is observed due to tilting and denser packing of the molecules. At low temperature and low coverage an interesting rosette phase formed. The rosette phase is built up of bowl opening down molecules and molecules tilted along their x- and y-axes (tilted bowl opening up molecules). At *LT*, short range row formation is found in the full monolayer and around the islands of the rosette phase at low coverage. At low coverage and low temperature single molecules are found to be adsorbed with their central six-membered ring (bowl opening up); dimers are tilted on the surface. Second layer growth seems to stabilize the layer underneath in a long range stripe phase.

The second largest molecular bowl under investigation (**7**, Chapter 7), as well as **6** (Chapter 6) are only mirror symmetric. Both gave azimuthal zig-zag patterns with rows of molecules oriented in the same direction. Also rows of molecules in which every other molecule is oriented in the opposite direction were observed (for **7**). Every observed phase is stable at room temperature and does not change with cooling.

A tilt towards its benzene ring was observed for **6** in the monolayer, with an azimuthal angle of $10°$ towards the neighboring molecule within the same row in a high density phase and an azimuthal angle of $30°$ in a low density phase. Second layer growth starts from the empty spaces within the zig-zag rows and the indeno-moiety appears to protrude upwards.

For **7** a substantial tilt is observed upon adsorption. Three different phases were observed: a hexagonal phase in which every molecule is pointing in the same direction, a stripe phase (with an azimuthal angle of $60°$), and an antistripe phase (with bowls pointing in opposite directions from each other). Models (in agreement with the STM-data) suggest that **7** is tilted so that the middle six-membered ring is the preferred binding site.

Influence of substrate surface symmetry: from Cu(111) to Cu(100).

Changing the substrate from Cu(111) to Cu(100) influences the formed overlayer; We demonstrated that the unit cell of the mirror symmetric mono-indenocorannulene (**6**) changed from (5 1, 2 7) to (4 0, -1 4). The adsorption orientation was calculated with a MM+ force field and appeared to be more "parallel"-like then **6** shows on Cu(111), since the "hub"-bond aligned with the mirror symmetry of the molecule is bound parallel to the substrate on top of a fourfold hollow site.

Comparison:

The highest 2D molecular surface density of the investigated molecules was found for **7**, which has the same surface density as **1** and **2** after the first phase transition. Due to a substantial tilt of **7** on the surface, the molecules self-assemble into such a dense packing. A comparison of the observed phases, crystallographic plane groups, coverage, temperature, and probed substrates of all investigated molecules (**2**, **5**, **6**, **7** and **8**) and previously studied molecules (**1**, **3**, and **4**) is shown in Tab. 9.1.

Table 9.1.: Summary of symmetry, observed phases, 2D-molecular density in *[in surface atoms per molecule]*, crystallographic plane groups, and investigated substrates of **1**, derivatives of **1**, and other buckybowls. TT = transition temperature $(210 \ldots 230\,\mathrm{K})$

					1,3,5,7,9-pentasubstituted corannulene				
Compound	**1** [60]	1 [116] / **2**			**3** [80]	**4** [128]		**5**	
Symmetry	C_{5v}	C_5			C_5	C_5		C_5	
Substrate	Cu(110)	Cu(111)			Au(11 12 12)	Cu(111)		Cu(111)	
Temperature	RT, LT	RT	TT	LT	LT	LT		RT, LT	
Density	11	16	14	14	16	19	21	36	37.5
Crystallographic plane group	pm	pm	p2mg	p2mg	p2mg	p2mg	—	p2mg	p2gg
Unit cell	(4 1, −3 2)	(4 0, 0 4)	(4 0, 3 7)	(4 2, 0 7)	(8 0, 0 8)	(5 2, 1 8)	(5 3, 2 3)	(7 6, −5 6)	(13 7, −1 11)^{M}

Compound	**6**			**7**			**8**		
Symmetry	$C_{1v} = D_1$			$C_{1v} = D_1$			C_2		
Substrate	Cu(100)	Cu(111)		Cu(111)			Cu(111)		
Temperature	RT, LT			RT, LT			RT	LT	
Density	16	18.5	16.5	16	14	14	25	25	18
Crystallographic plane group	p1	p1	p1	p1	p2mg	p2mg	p3	p1	p2mg
Unit cell	(4 0, −1 4)	(5 0, 4 8)	(5 1, 2 7)	(4 0, −1 4)	(4 0, 3 7)	(4 2, 0 7)	(10 5, −5 5)	(27 0, 0 27)	(4 0, 4 9)

10. Outlook

Modifications of Corannulene may lead to many interesting and investment-worthy products, some of them already mentioned in Chapter 1.

To obtain deeper insight into *2D* self-assembly processes and (chiral) molecular recognition, one may increase the size of the functional groups of (penta-)substituted-**1** [133] and or examine their self assembly on surfaces with different symmetries. These modifications may finally lead to chiral recognition that could be observed by *STM*. Adsorbed molecules with bowls opening away from the surface could be used as a host-systems for non-covalently bonded molecules with bowl- or ball-shapes, e.g. C_{60} or other fullerenes. Adsorbed molecules with bowls opening towards the surface could be realized by adding more reactive (e.g. thiolate) functional groups, e.g. penta(phenylthiolate)-corannulene prior to absorption on Cu(111) and other substrates (Fig. 10.1) [134]. The five-membered ring would then be exposed for further surface chemistry.

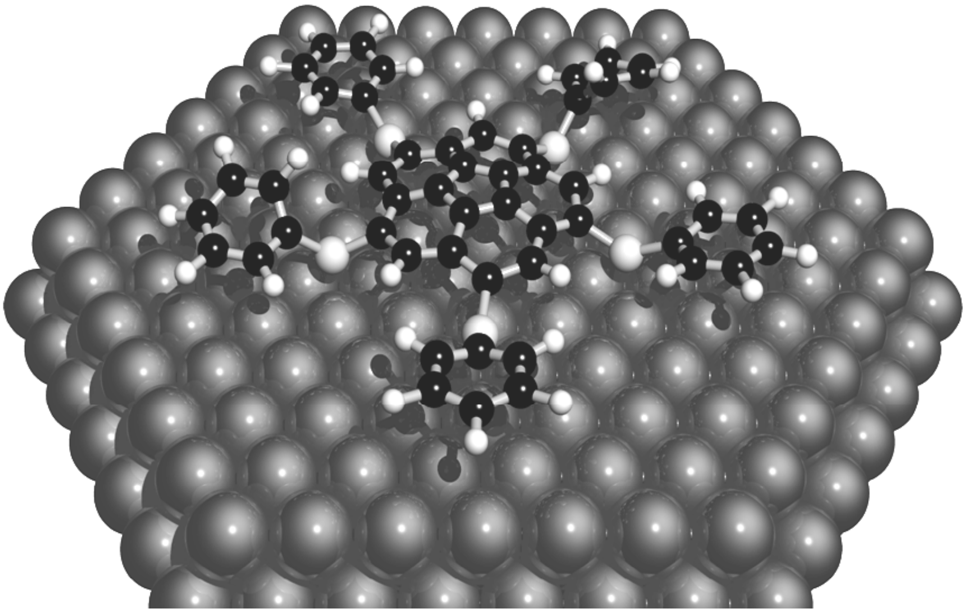

Figure 10.1.: Molecular model for a molecule with a bowl-opening facing towards the substrate surface, penta(phenylthiolate)-corannulene on Cu(111).

Doping **1** or other buckybowls with alkali-metals (Li, Nq, K) may lead to high-temperature superconductivity above the transition temperature of doped C_{60} ($T_c = 33K$). Super-atomic orbitals (observed for Buckminsterfullerenes [135, 136]) may also be observable for Corannulene-derivatives.

Corannulene-capped carbon nanotube (*CNT*) growth is envisioned by some groups to be possible via stepwise Diels-Alder addition [137–139] with ethyne, ethylene, and 1,3-butadiene. This would be favoured if the metal substrate is active enough to catalyze the addition of more carbon substituents to the rim of the starting buckybowl **1**, **8**, or others. Therefore **1** would intrinsically yield an armchair single-walled carbon nanotube (*SWCNT*) and **8** a zig-zag *SWCNT* (Fig. 10.2). Other modified Corannulenes may be used as building blocks for chiral *CNT*s [140–143].

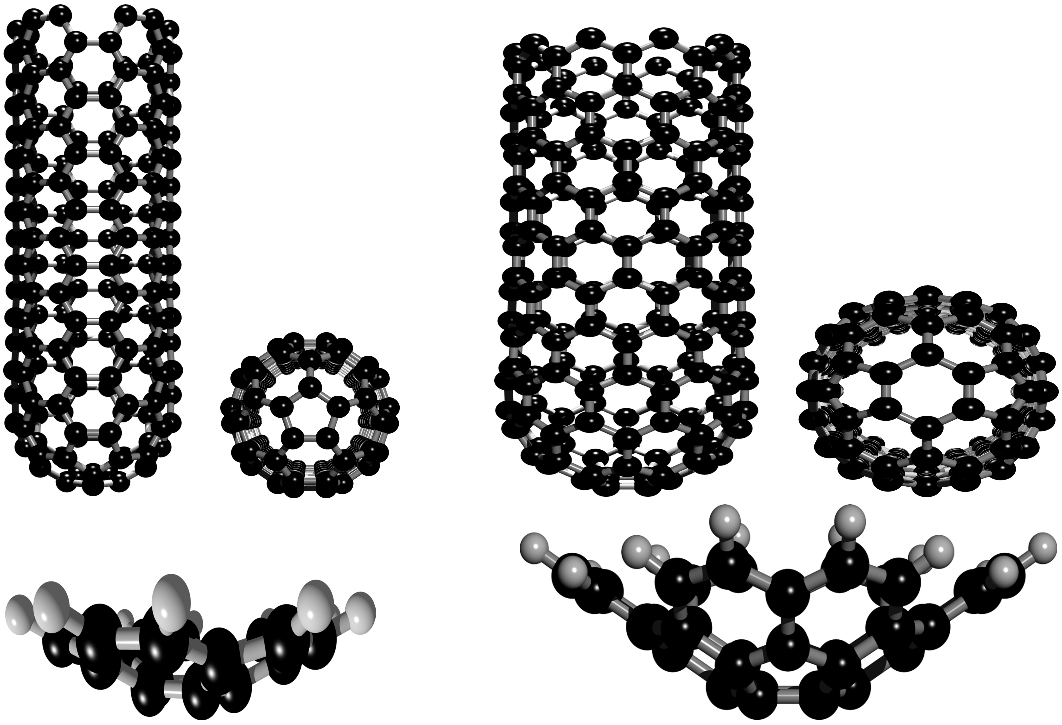

Figure 10.2.: Armchair (**left**) and zig-zag (**right**) Single-Walled Carbon Nanotubes resulting from growth of **1** and **8**.

A. Appendix

A1 Sample cleaning procedures

Sample cleaning consisted of sputtering (s. Tab. A.1) and annealing the sample (s. Tab. A.2).

Table A.1.: Sputtering procedures for the Cu(111) substrate at the different *UHV* systems.

	Time t [min]	Pressure p [mbar]	Sample Current I_S [µA]	Filament Current I_F [mA]	Ion Energy E_I [keV]
ESCA	50	$1 \cdot 10^{-5}$	~ 3	10	1
	2×25	$1 \cdot 10^{-5}$	~ 3	10	1
RAIRS	45	$3 \cdot 10^{-6}$	~ 4	10	1.5
	2×25	$3 \cdot 10^{-6}$	~ 4	10	1.5
VT-STM	40	$1 \cdot 10^{-4}$	~ 3	10	2
	2×20	$1 \cdot 10^{-4}$	~ 3	10	2

Table A.2.: Annealing procedures for the Cu(111) substrate at the different *UHV* systems.

	Time t [min]	Temperature T [°C]	Pressure p [mbar]	Filament Current I_F [A]	Filament/Accelerating Voltage $U_{F/A}$ [V]
ESCA(1)(4)	5	~ 600	$< 1 \cdot 10^{-9}$	0.9	10.8/—
RAIRS(2)(4)	5	600	$< 5 \cdot 10^{-9}$	2.52	—/500
VT-STM(3)	2	~ 333	$< 8 \cdot 10^{-9}$	9.1	2.0/—

Heating methods: (1) Direct current (resistive), (2) Electron beam, (3) *PBN* heater behind the sample and thermocouple at the manipulator, (4) Thermocouple in the sample.

Table A.3.: Temperature calibration of the *VT-STM* manipulator: Voltage applied to the *PBN* heater. Waiting periode: $\sim 30\ \mathrm{min}$ for Temperature stabilization.

Temperature at the sample T_S [°C]	Temperature Manipulator T_M [°C]	Voltage U [V]	Current I [A]
41	34	0.5	0.1
51	37	0.8	0.1
60	40	1.0	0.1
70	43	1.2	0.2
90	49	1.5	0.2
117	58	1.9	0.3
140	66	2.2	0.3
164	76	2.5	0.4
189	85	2.8	0.4
209	98	3.1	0.5
232	116	3.4	0.5
250	127	3.6	0.6
368	192	5.0	1.0
518	301	7.0	1.5
584	349	8.0	1.8
653	400	9.2	2.1

A2 Synthesis of investigated molecules

Synthesis of perdeutero-corannulene

After the first synthesis of corannulene **1** [37] numerous synthetic pathways from different groups have been published [42–47]. Recently the Siegel group published the kilogram-scale synthesis of **1** [48]. They kindly provided us with highly purified **1** suitable for the *STM* experiments in our group [60, 85, 115–118].

The perdeutero-corannulene **2** for this work was synthesized by the Siegel group, who used a strong acid [mesitylene-H][$CHB_{11}H_5Cl_6$] [119] as deuteration catalyst using toluene-d_8 (Fig. A.1) [120].

Synthesis of pentamethyl- and pentaphenyl-corannulene

Pentaphenyl-corannulene **5** shows C_5 symmetry and is considered to be a rigid star. The synthesis of **5** (as performed by the Siegel group) via a Negishi cross coupling reaction of **3**, which is obtained by chlorination of **1**, is shown in Fig. A.2 [121].

Synthesis of mono-indenocorannulene

By adding a benzene ring to **1** to form mono-indenocorannulene **6**, the overall C_5 symmetry breaks down to a simple C_{1v} mirror symmetry. The strain in the molecule is already so high that no bowl-to-bowl inversion is observed at *RT* [122]. **6** was synthesized by the Siegel group by successive direct bromination of **1**, [55, 63], boronation with pinacolborane, and Pd-catalyzed Suzuki-Heck-type coupling with 1,2-dibromobenzene (Fig. A.3) [123, 124].

Synthesis of the $C_{32}H_{12}$-buckybowl

The synthesis of $C_{32}H_{12}$-buckybowl **7** using flash vacuum pyrolysis *FVP* at $1100\,^{\circ}\mathrm{C}$ from 7,12-bis(2-bromophenyl)benzo[k]fluoranthene ($0.14\,\%$ yield) was reported by Clayton *et al.* [125]. The Wu group improved the yield to $18.6\,\%$ by using as starting material 1,8-bis(arylethynyl)naphtalene, performing a Pd-catalyzed Heck-type cycloaddition reaction with iodobenzene to produce benzo[k]fluoranthene, and cyclizing this intermediate to form **7** (Fig. A.4) [69]; a portion of this material was provided for the work described in this thesis. **7** has the same simple C_{1v} mirror symmetry as **6**.

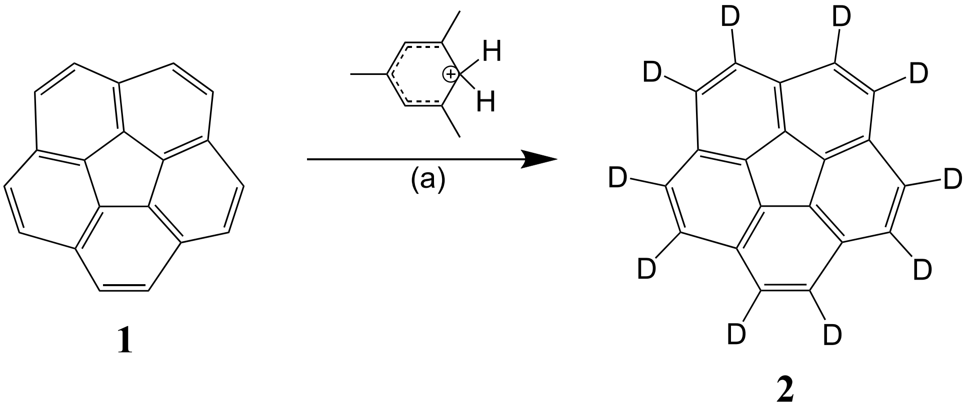

(a) $CHB_{11}H_5Cl_6^-$, Toluene-d_8, RT, 2 weeks, 76%

Figure A.1.: Synthesis of perdeutero-corannulene [120].

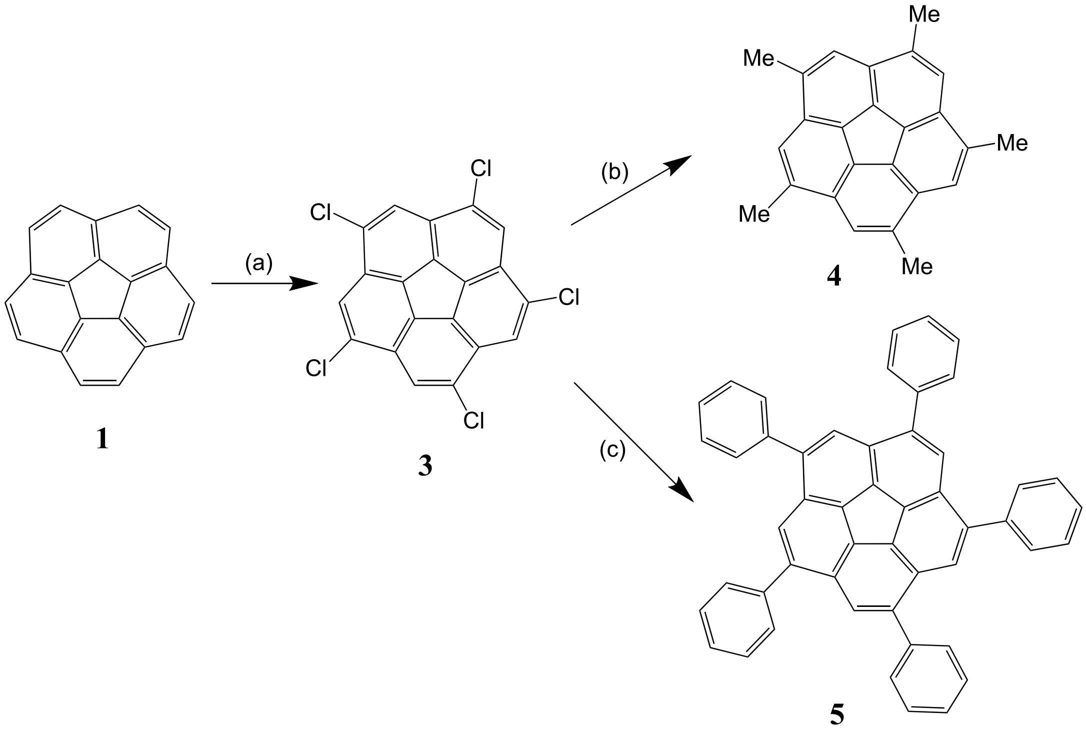

(a) ICl, CH_2Cl_2, -75 to 23 °C, 52%
(b) $AlMe_3$, $NiCl_2$(dppp), DME
(c) PhZnCl, $NiCl_2$(dppp), THF

Figure A.2.: Synthesis of pentamethyl-corannulene [63] and pentaphenyl-corannulene [121].

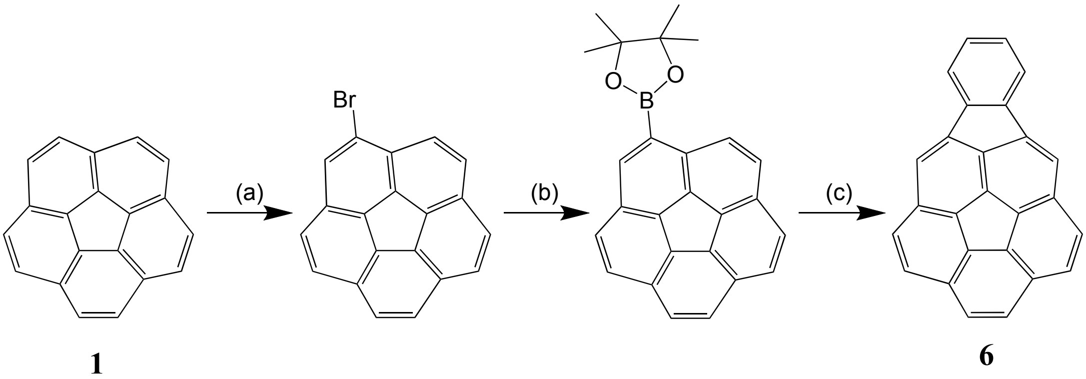

(a) *Br_2, $FeCl_3$, CH_2Cl_2, 95%*
(b) *$PdCl_2$(dppf), Et_3N, Pinacolborane, 1,4-Dioxane*
(c) *1,2-dibromobenzene,*
20% Pd_2(dba)$_3$, P(Cy)$_3$, DBU, DMF, Δ, 95%

Figure A.3.: Synthesis of mono-indenocorannulene [63, 123].

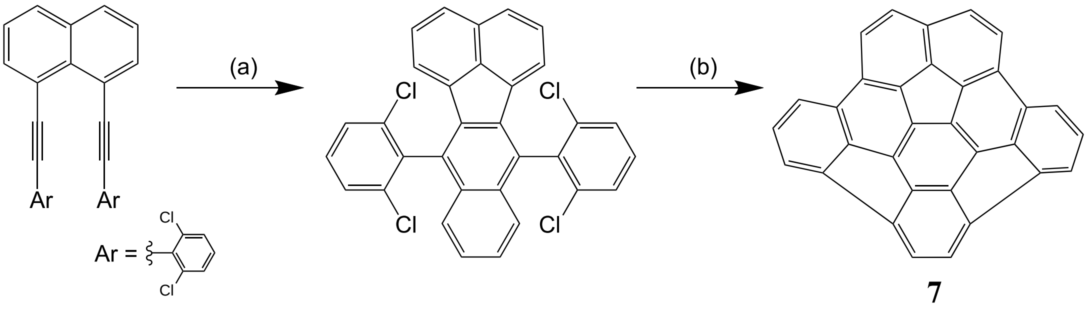

(a) *C_5H_5I (1.5 equiv.), $Pd(OAc)_2$ (5 mol%), AgOAc (1 equiv.), p-xylene, 110 °C, 36 h*
(b) *$Pd(PCy_3)_2Cl_2$ (40 mol%), DBU, DMF, 160 °C , 36 h*

Figure A.4.: Synthesis of $C_{32}H_{12}$-buckybowl [69].

Synthesis of the $C_{38}H_{14}$-buckybowl

A "fragment" of C_{70} buckminsterfullerene was synthesized by the Wu group [70]. The synthetic pathway towards this larger $C_{38}H_{14}$-buckybowl **8** (Fig. A.5) begins with 1,8-bis(arylethynyl)naphthalene. Rh-catalyzed cycloaddition with acenaphthylene produces an intermediate, which is cyclized using a Pd-catalyzed Heck-type cycloaddition to form $C_{38}H_{14}$-buckybowl. The symmetry of **8** is C_{2v}.

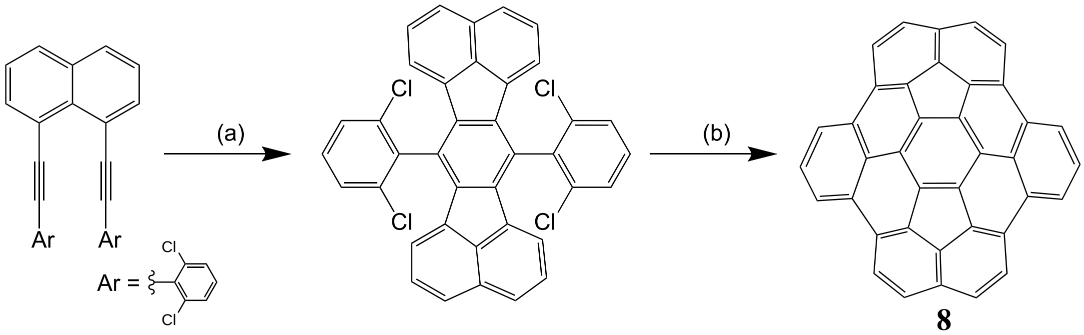

8

(a) *Acenaphthylene,*
1. $[RhCl(PPh_3)_3]$ 2.5 mol% p-xylene, Δ, 60 h,
2. DDQ, toluene
(b) *$[PdCl_2(PCy_3)_2]$ 40 mol%, DBU, DMF, 160 °C , 36 h, $>$10%*

Figure A.5.: Synthesis of $C_{38}H_{14}$-buckybowl [70].

A3 Symmetry groups

Crystallographic notation: A primitive cell is indicated **p**, a face-centered cell **c**, followed by the highest order of rotational symmetry (1-fold is not indicated, 2-fold, 3-fold, 4-fold, or 6-fold). After choosing the main translational axis (one reflection axis perpendicular to translation axis) the following symbols indicating symmetries (**m** for mirror, **g** for glide reflection, or **1** - which can also be omitted - for none) are added. For the first symbol the axis of the reflection or glide reflection is perpendicular to the main axis and for the second symbol either parallel or rotated by $180°/n$ for $n > 2$.

A3.1 Point groups

One unique property of all point-groups is the fact that a point is by all symmetry operations (rotation, reflection) mapped back onto itself. Two-dimensional point groups (see Table A.4) can be split into cyclic C_n (with only n-fold rotational symmetry) and the Dieder-(or dihedral)group D_n (n-fold rotational symmetry together with the same order reflection axes). In three-dimensional Euclidian space the cyclic group can obtain additional (n) vertical (including the rotational axis) or one horizontal (perpendicular to the rotational axis) reflection planes, indicated by C_{nv} or C_{nh} respectively. The Dieder-group can have additional (n) diagonal or horizontal reflection planes, indicated by D_{nd} or C_{nh} respectively.

Table A.4.: Overview of selected 2-dimensional point groups (Cyclic- and Dieder-group) (Ornaments [144], symmetry overlay [145]).

C_1 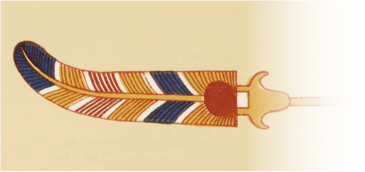 1-fold rotation center	C_4 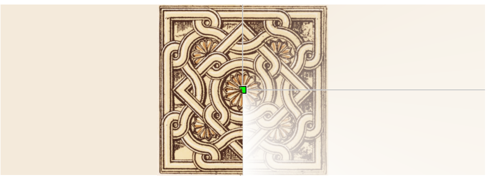 4-fold rotation center
C_6 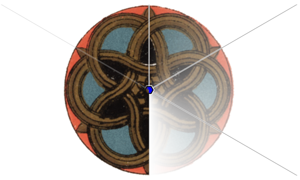 6-fold rotation center	D_1 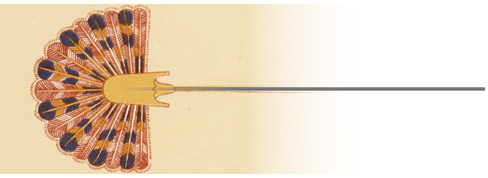 1-fold rotation center with one reflection axis

Continued on next page

Table A.4 – *Continued from previous page*

D$_4$ 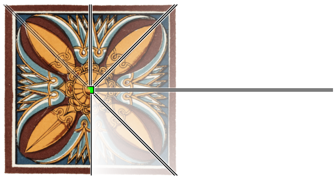 4-fold rotation center with four reflection axes	D$_{11}$ 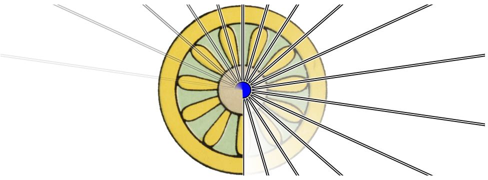 11-fold rotation center with 11 reflection axes

A3.2 Frieze groups

All seven Frieze goups consist of a translational symmetry along the Frieze direction. They can have additional vertical or horizontal line reflection axes, glide reflection axes, and/or one or two 2-fold ($180°$) rotation centers (indicated by rhombi in Table A.5).

Table A.5.: Overview of all seven Frieze groups (Ornaments [144], symmetry overlay [145]).

F-p1 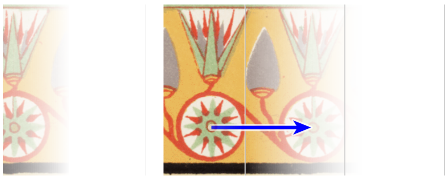 Only translation along the Frieze direction	F-p1m1 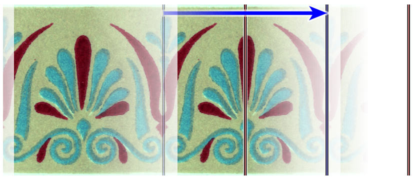 Translation and vertical line reflection
F-p11m 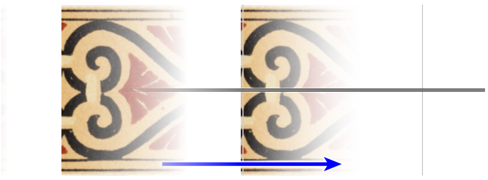 Translation, horizontal line reflection, and glide reflection	F-p11g 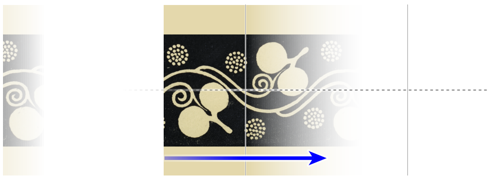 Translation and glide reflection

Continued on next page

Table A.5 – *Continued from previous page*

F-p2 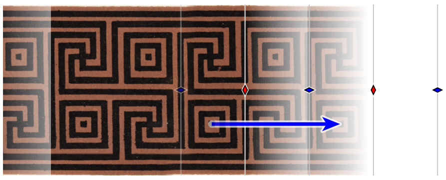 Translation and two2-fold rotation centers	F-p2mg 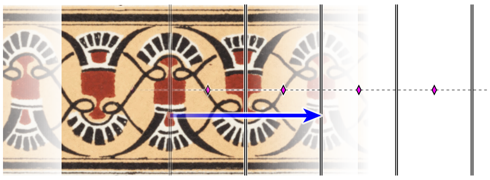 Translation, 2-fold rotation center, vertical line reflection, and glide reflection
F-p2mm 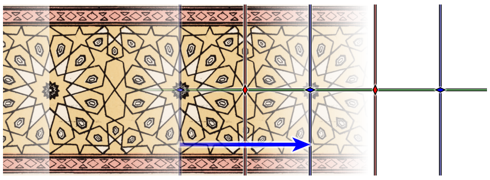 Translation, 2-fold rotation centers, horizontal line reflection, vertical line reflection, and glide reflection	

A3.3 Plane crystallographic group

In contrast to the Frieze groups, plane crystallographic groups contain of translational symmetry in two distinct directions. They can have additional reflection axes, glide reflection axes, and two-fold, three-fold (120° indicated as triangles), four-fold (90° indicated as squares), and/or six-fold (60° indicated as hexagons in Table A.6) rotation centers.

Table A.6.: Overview of all 17 two-dimensional plane crystallographic groups (Ornaments [144], symmetry overlay [145]).

p1 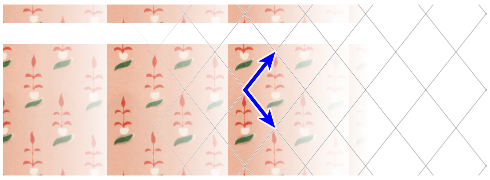 Only translations (tranlation axes may be inclined and can have different lengths)	p2 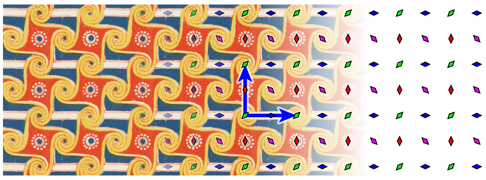 Translations and four 2-fold (180°) rotation centers

Continued on next page

Table A.6 – *Continued from previous page*

pm 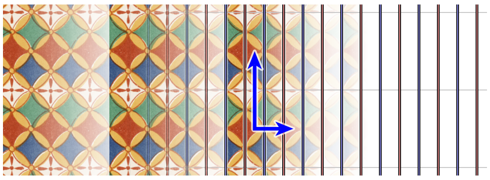 Translations and two to eath other parallel reflection axes	pg 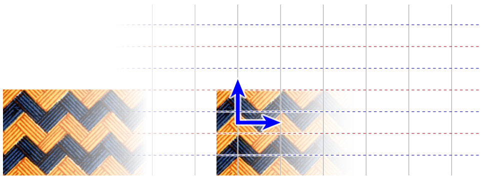 Translations and to each other parallel glide reflection axes
cm 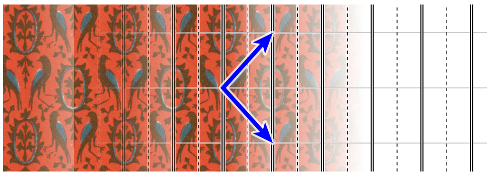 Translations and parallel alternating reflection- and glide reflection axes	p2mm 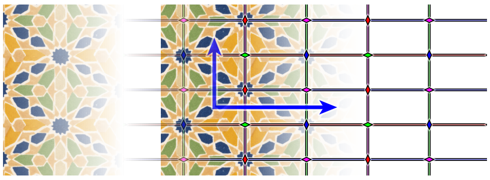 Translations, perpendicular reflection axes, and at the intersections four 2-fold rotation centers
p2mg 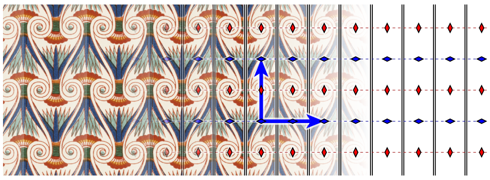 Translations, reflection axes in one direction and two perpendicular glide reflection axes, and two 2-fold rotation centers (located on the glide reflection axes)	p2gg 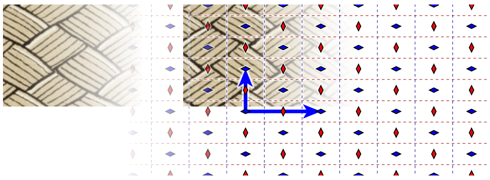 Translations, two perpendicular glide reflection axes, and two 2-fold rotation centers
c2mm 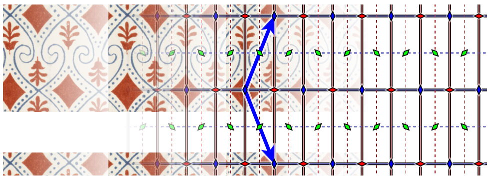 Translations, two perpendicular reflection axes with 2-fold rotation center at the intersection, and two perpendicular glide reflection axes with 2-fold rotation center	p4 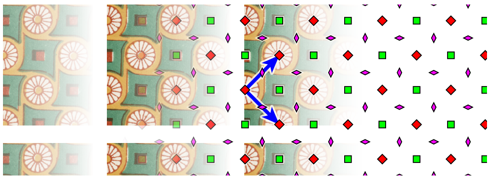 Translations, two 4-fold (90°) rotation centers inbetween 2-fold rotation centers

Continued on next page

Table A.6 – *Continued from previous page*

p4mm 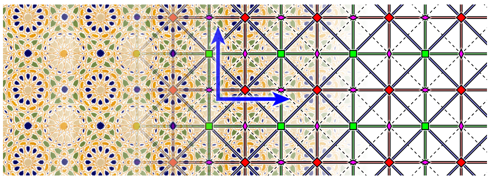 Translations, perpendicular and diagonal reflection axes, glide reflection axes, 2-fold rotation centers (at the intersection of the glide reflection axes) and two 4-fold rotation centers (all located on reflection axes)	p4gm 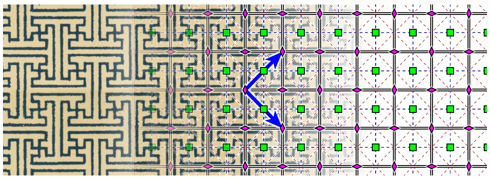 Translations, perpendicular reflection axes with 2-fold rotation centers on the intersections, glide reflection axes parallel to the reflection axes, in between them, and under 45°, and two 4-fold rotation centers (mirror image to each other)
p3 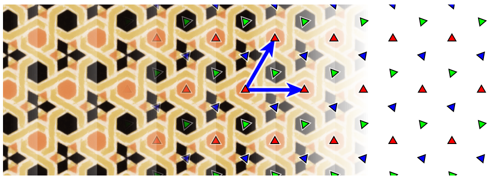 Translations and three 3-fold (120°) rotation centers	p3m1 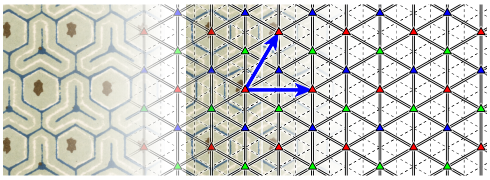 Translations, reflection axes like an equilateral triangle, three 3-fold rotation centers (lie on reflection axis), and glide reflection axes (halfway between adjacent parallel reflection axes)
p31m 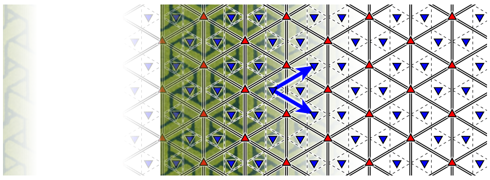 Translations, three 3-fold rotation centers (mirrow image to each other, one not located on a reflection axis), reflection axes $(60^\circ$ to each other), and glide reflection axes (halfway between adjacent parallel reflection axes)	p6 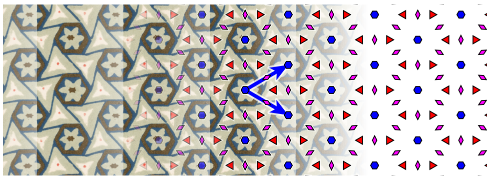 Translation, one 6-fold (60°) rotation center $(60^\circ$ rotated to each other), two 3-fold rotation centers $(120^\circ$ rotated to each other), and three 2-fold rotation centers

Continued on next page

Table A.6 – *Continued from previous page*

p6m 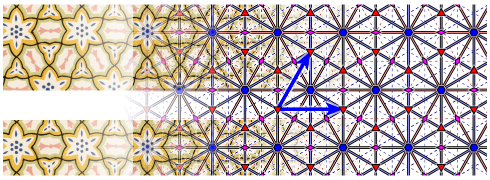 Translations, one 6-fold rotation center, two 3-fold rotation centers (60° rotated to each other), three 2-fold rotation centers (60° rotated to each other), reflection axes in six directions, and six glide reflection axes (halfway between adjacent parallel reflection axes)

A4 2D-Fourier transformation for (STM-)Images

Periodic patterns in a picture can be obtained through two-dimensional Fourier-transformation, which splits it into individual wavelength and directions. Doing so a depicted periodic structure in real space gets transformed into the fourier (reciprocal) space leading to ”clear” outlined peaks. The positions of the peaks are determined by the distance and directions of the periodic pattern. The lattice constants (vectors) and angles can be very precisely determined by the wavelengths and direction difference of the peaks respectively by transforming it back into the real space with the inverse-Fourier-transformation. The hexagonal lattice of, e.g. the Cu(111) surface, leads to 6 peaks in the Fourier-representation which are arranged in a circle around the origin. The diameter of the circle corresponds to the lattice constant, while the angle between two adjacent peaks through the center leads to the angle-lattice parameter of Cu(111). 2-D Fourier-transformations pair for $M \times N$ sized pictures (Equ. A.1):

$$F(u,v) = \frac{1}{MN} \sum_{m=0}^{M-1} \sum_{n=0}^{N-1} f(m,n) \cdot e^{-i \cdot 2\pi \cdot \left(\frac{um}{M} + \frac{vn}{N}\right)} \tag{A.1a}$$

$$f(m,n) = \frac{1}{MN} \sum_{m=0}^{M-1} \sum_{n=0}^{N-1} F(m,n) \cdot e^{-i \cdot 2\pi \cdot \left(\frac{um}{M} + \frac{vn}{N}\right)} \tag{A.1b}$$

A5 Image averaging procedure

Contrast enhancement for a selected area in an *STM*-image is done with the following procedure in the PV-WAVE v6.21 SXM-Shell program from University of Basel (Switzerland)[1]:

1. Choose an already quite good image to select your area for enhancement;
2. Apply *FFT* the copied hole image and lowpass filtering (of a selected area);
3. Choose an area of the lowpass filtered image for averaging;
4. Perform cross-correlation of the selected part with the hole image;
5. Choose the grade/points of correlation which should be implemented;
6. Average the cross-correlated parts.

---

[1] D. Brodbeck, D. Buergler, R. Hofer, G. Tarrach, 1998.

A6 Pentaphenyl-corannulene bowl opening up

Indication that the bowl opening points away from the surface due to a dark depression in the center of the pentaphenyl-corannulene is shown in figure A.6.

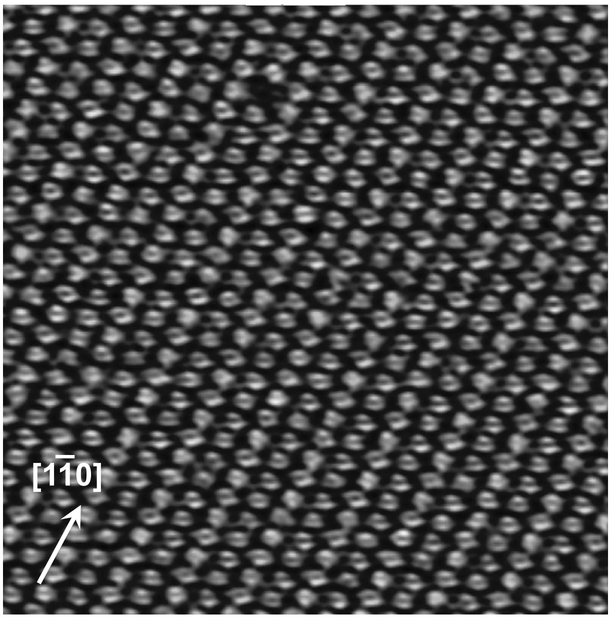

Figure A.6.: *STM*-image ($30 \times 30\,\mathrm{nm}^2$, $-0.645\,\mathrm{V}$, $129\,\mathrm{pA}$, *RT*) of the (7 6, −5 6) structure. Under these tunneling conditions, the phenyl rings are not well resolved, but the molecules show a dark depression in the center, indicating that the bowl opening points away from the surface.

A7 LEED of pentaphenyl-corannulene on Cu(111)

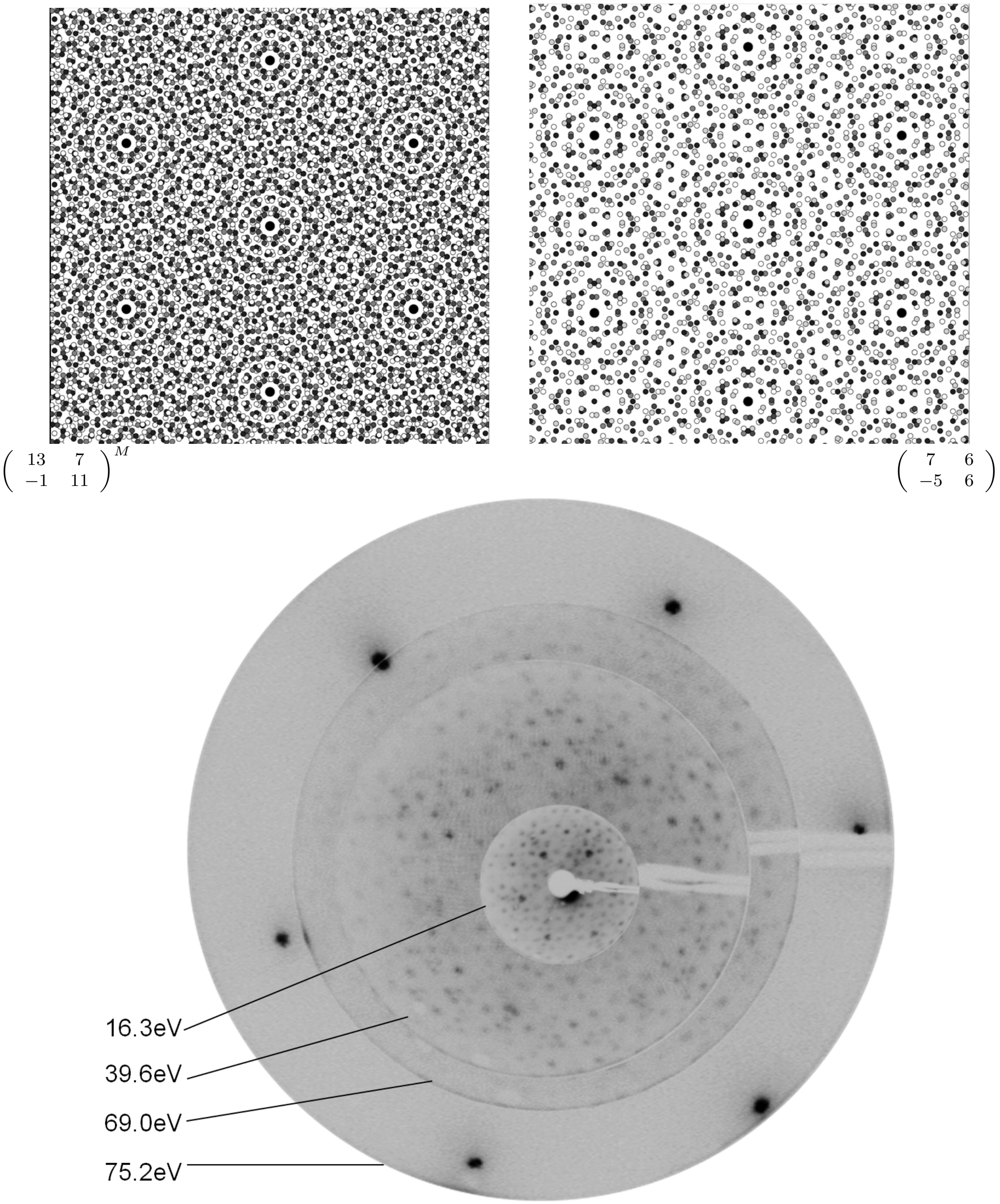

Figure A.7.: The lack of correlation between the (**upper**) simulations of the *LEED*-patterns for the (13 7, −1 11)^{M} and (7 6, −5 6) unit cells and (**lower**) overlayed *LEED*-experiments with various energies indicate the coexistence of the (13 7, −1 11)^{M} phase with the (7 6, −5 6) phase.

A8 TPD of pentaphenyl-corannulene

TPD experiments from **5** deposited on Cu(111) reveale a dehydrogenation at $563\,\mathrm{K}$ (Fig. A.8).

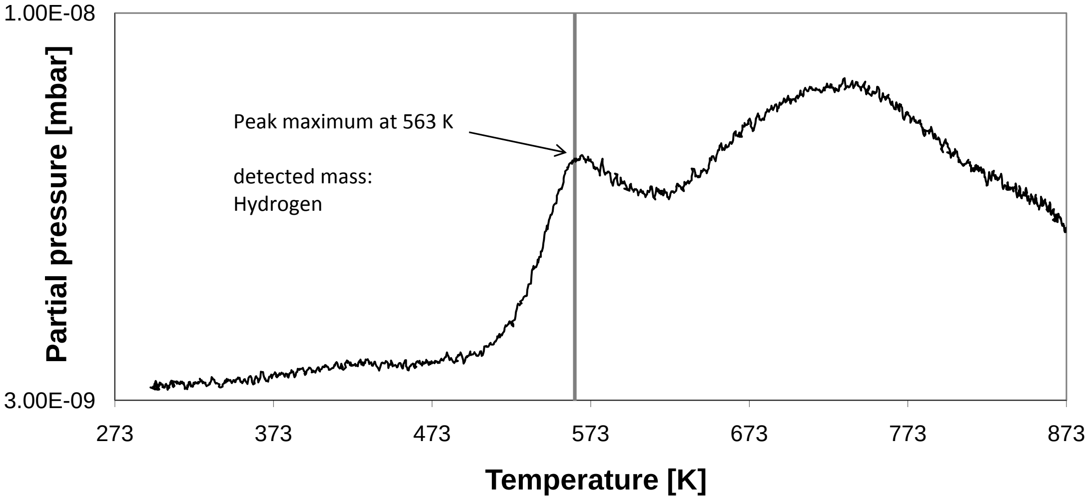

Figure A.8.: *TPD* experiments showing the beginning of hydrogen desorption from the sample, with a peak maximum at $563\,\mathrm{K}$ for the recorded mass of hydrogen $(2\,\mathrm{amu})$. The second broader peak is assumed to result from hydrogen desorption of the manipulator.

A9 Organic Solar Cells

Organic solar cells [146] rely just like any other photovoltaic cells (mono-, poly-crystalline, and amorphe silicone cells [147], GaAs-cells [148], CdTe-cells [149], Cu(In,Ga)(S,Se)$_2$ (*CIGS*)-cells [150], dye-sensitized solar cell (*DSSC*) [151], quantum dot solar cell (*QDSC*) [17]) on the photoelectric effect[2] [152, 153]. Three different types can be distinguished. The outer photoelectric effect (or photoemission) describes the "extraction" of an electron from the metal surface through irradiation ($E_{kin} = \hbar\nu - \phi$ kinetic energy equals the energy of the incident beam of light minus the work function of the material), the inner photoelectric effect describes the creation of electron hole pairs and the separation of the charge carriers leading to a photo-current, and the photo ionisation of atoms or molecules.

One or two layers of electron donor organic material (e.g. conjugated polymers), and/or an electron acceptor (e.g. fullerenes, corannulene) are sandwiched between two electrodes (typically transparent Indium tin oxide (*ITO*) with a high work function and a metal with a low work function), which transport the electrons. The working principle is then a a three step process: 1) light absorption at the donor layer to generate electron hole pairs or excitons 2) separation of the charge carriers of opposite type into the acceptor layer, 3) extraction of the charge carriers (Fig. A.9).

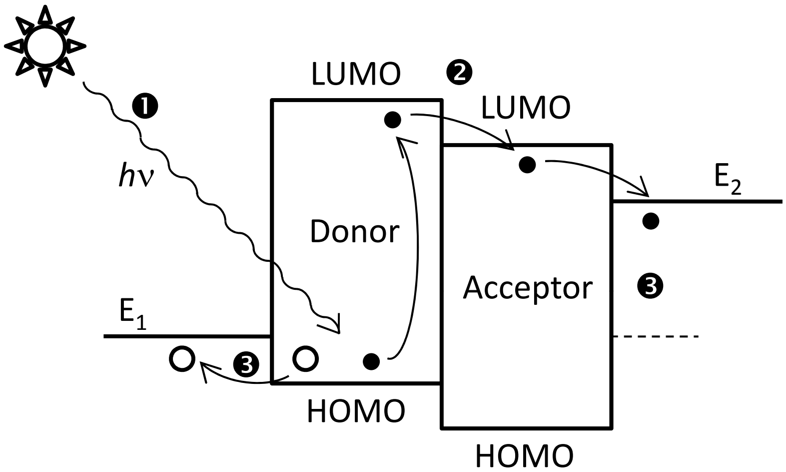

Figure A.9.: Working principle of a organic solar cell: ① light adsorption at the donor layer to generate electron hole pairs, ② separation of the charge carriers of opposite type into the acceptor (e.g. corannulene), ③ extraction of the charge carriers with the two electrodes (E$_1$ and E$_2$).

---

[2] A. Einstein was awarded the Nobel Prize in Physics 1921 for "his services to Theoretical Physics, and especially for his discovery of the law of the photoelectric effect" one year later, in 1922. www.nobelprize.org

Bibliography

[1] H. Shirakawa, E. J. Louis, A. G. MacDiarmid, C. K. Chiang, A. J. Heeger, *Synthesis of electrically conducting organic polymers: halogen derivaties of polyacetylene, (CH)$_x$*, J. Chem. Soc., Chem. Commun. 16, pp. 578-580, 1977. doi: 10.1039/C39770000578.

[2] J.-M. Tarascon, M. Armand, *Issues and challenges facing rechargeable lithium batteries*, Nature 414, pp. 359-367, 2001. doi: 10.1038/35104644.

[3] M. Armand, J.-M. Tarascon, *Building better batteries*, Nature 451, pp. 652-657, 2008. doi: 10.1038/451652a.

[4] J. H. Burroughes, D. D. C. Bradley, A. R. Brown, R. N. Marks, K. Mackay, R. H. Friend, P. L. Burns, A. B. Holmes, *Light-emitting diodes based on conjugated polymers*, Nature 347, pp. 539-541, 1990. doi: 10.1038/347539a0.

[5] R. H. Friend, R. W. Gymer, A. B. Holmes, J. H. Burroughes, R. N. Marks, C. Taliani, D. D. C. Bradley, A. A. Dos Santos, J. L. Brédas, M. Lögdlund, W. R. Salaneck, *Electroluminescence in conjugated polymers*, Nature 397, pp. 121-128, 1999. doi: 10.1038/16393.

[6] J. Mack, P. Vogel, D. Jones, N. Kaval, A. Sutton, *The development of corannulene-based blue emitters*, Org. Biomol. Chem. 5, pp. 2778-2452, 2007. doi: 10.1039/B705621D.

[7] M. A. Loi, J. Gao, F. Cordella, P. Blondeau, E. Menna, B. Bártová, C. Hébert, S. Lazar, G. A. Botton, M. Milko, C. Ambrosch-Draxl, *Encapsulation of conjugated oligomers in singe-walled carbon nanotubes: Towards nanohybrids for photonic devices*, Adv. Mater. 22, pp. 1635-1639, 2010. doi: 10.1002/adma.200903527.

[8] C. D. Dimitrakopoulos, P. R. L. Malenfant, *Organic thin film transistors for large area electronics*, Adv. Mater. 14, pp. 99-117, 2002. doi: 10.1002/1521-4095(20020116)14:2<99::AID-ADMA99>3.0.CO;2-9.

[9] S. Lee, B. Koo, J. Shin, E. Lee, H. Park, *Effects of hydroxyl groups in polymeric dielectrics on organic transistor performance*, Appl. Phys. Lett. 88, 162109, 2006. doi: 10.1063/1.2196475.

[10] N. S. Sariciftci, D. Braun, C. Zhang, V. I. Srdanov, A. J. Heeger, G. Stucky, F. Wudl, *Semiconducting polyer-buckminsterfullerene heterojunctions: Diodes, photodiodes, and photovoltaic cells*, Appl. Phys. Lett. 62, pp. 585-587, 1993. doi: 10.1063/1.108863.

[11] U. Purushotham, G. N. Sastry, *Conjugate acene fused buckybowls: evaluating their suitability for p-type, ambipolar and n-type air stable organic semiconductors*, Phys. Chem. Chem. Phys 15, pp. 5039-5048, 2013. doi: 10.1039/c3cp44673e.

[12] H. Hoppe, N. S. Sariciftci, *Organic solar cells: an overview*, J. Mater. Res. 19, pp. 1924-1945, 2004. doi: 10.1557/JMR.2004.0252.

[13] Y. Hayashi, I. Yamada, S. Takagi, A. Takasu, T. Soga, T. Jimbo, *Influence of structure and* C_{60} *composition on properties of blends and bilayers of organic donor-acceptor polymer/*C_{60} *photovoltaic devices*, Jpn. J. Appl. Phys. 44, pp. 1296-1300, 2005, doi: 10.1143/JJAP.44.1296.

[14] Y. Yao, C. Shi, G. Li, V. Shrotriya, Q. Pei, Y. Yang, *Effects of* C_{70} *derivative in low band gap polymer photovoltaic devices: Spectral complementation and morphology optimization*, Appl. Phys. Lett. 89, 153507, 2006. doi: 10.1063/1.2361082.

[15] H. Hoppe, N. S. Sariciftci, *Polymer solar cells*, Adv. Polym. Sci. 214, pp. 1-86, 2008. doi: 10.1007/12_2007_121.

[16] V. Shrotriya, *Organic photovoltaics: Polymer power*, Nature Photon. 3, pp. 447-449, 2009. doi: 10.1038/nphoton.2009.130.

[17] P. V. Kamat, *Quantum dot solar cells. The next big thing*, J. Phys. Chem. Lett. 4, pp. 908-918, 2013. doi: 10.1021/jz400052e.

[18] T. Kato, T. Yamabe, *Electron-intramolecular-phonon coupling and possible superconductivity in negatively charged coronene and corannulene*, J. Chem. Phys. 117, pp. 2324-2331, 2002. doi: 10.1063/1.1489899.

[19] A. F. Hebard, M. J. Rosseinsky, R. C. Haddon, D. W. Murphy, S. H. Glarum, T. T. M. Palstra, A. P Ramirez, A. R. Kortan, *Superconductivity at 18 K in potassium-doped* C_{60}, Nature 350, pp. 600-601, 1991, doi: 10.1038/350600a0.

[20] R. C. Haddon, *Electronic structure, conductivity, and superconductivity of alkali metal doped* C_{60}, Acc. Chem. Res 25, pp. 127-133, 1992. doi: 10.1021/ar00015a005.

[21] A. Y. Ganin, Y. Takabayashi, Y. Z. Khimyak, S. Margadonna, A. Tamai, M. J. Rosseinsky, K. Prassides, *Bulk superconductivity at 38 K in a molecular system*, Nature Mat. 7, pp. 367-371, 2008. doi: 10.1038/nmat2179.

[22] M. Mattarella, J. Garcia-Hartjes, T. Wennekes, H. Zuilhof, J. S. Siegel, *Nanomolar cholera toxin inhibitors based on symmetrical pentavalent ganglioside GM1os-sym-corannulenes*, Org. Biomol. Chem. 11, pp. 4333-4339, 2013. doi: 10.1039/c3ob40438b.

[23] S. Mizyed, P. E. Georghiou, M. Bancu, B. Cuadra, A. K. Rai, P. Cheng, L. T. Scott, *Embracing* C_{60} *with multiarmed geodesic partners*, J. Am. Chem. Soc. 123, pp. 12770-12774, 2001. doi: 10.1021/ja016761z.

[24] M. Makha, A. Purich, C. L. Raston, A. N. Sobolev, *Structural diversity of host-guest and intercalation complexes of fullerene* C_{60}, Eur. J. Inorg. Chem., pp. 507-517, 2006. doi: 10.1002/ejic.200500768.

[25] N. Kishi, Z. Li, Y. Sei, M. Akita, K. Yoza, J. S. Siegel, M. Yoshizawa, *Wide-range host capability of Pd^{II}-linked M_2L_4 molecular capsule with an anthracene shell*, Chem. Eur. J. 19, pp. 6313-6320, 2013. doi: 10.1002/chem.201204010.

[26] A. J. Olson, Y. H. E. Hu, E. Keinan, *Chemical mimicry of viral capsid self-assembly*, PNAS 104, pp. 20731-20736, 2007. doi: 10.1073/pnas.0709489104.

[27] A. Turchanin, A. Gölzhäuser, *Carbon nanomembranes from self-assembled monolayers: Functional surfaces without bulk*, Prog. Surf. Sci. 87, pp. 108-162, 2012. doi: 10.1016/j.progsurf.2012.05.001.

[28] C. A. Hunter, J. K. M. Sanders, *The nature of $\pi - \pi$ interactions*, J. Am. Chem. Soc. 112, pp. 5525-5534, 1990. doi: 10.1021/ja00170a016.

[29] E. A. Meyer, R. K. Castellano, F. Diederich, *Interactions with aromatic rings in chemical and biological recognition*, Angew. Chem. Int. Ed. 42, pp. 1210-1250, 2003. Angew. Chem. 115, pp. 1244-1287, 2003. doi: 10.1002/anie.200390319.

[30] T. Kawase, H. Kurata, *Ball-, bowl-, and belt-shaped conjugated systems and their complexing abilities: Exploration of the concave-convex $\pi - \pi$ interaction*, Chem. Rev. 105, pp. 5250-5273, 2006. doi: 10.1021/cr0509657.

[31] Y.T. Wu, D. Bandera, R. Maag, A. Linden, K.K. Baldridge, J.S. Siegel, *Multiethynyl corannulenes: synthesis, structure, and properties*, J. Am. Chem. Soc. 130, 10729, 2008. doi: 10.1021/ja802334n.

[32] F. Schreiber, *Structure and growth of self-assembling monolayers*, Prog. Surf. Sci. 65, pp. 151-256, 2000. doi: 10.1016/S0079-6816(00)00024-1.

[33] G. M. Whitesides, B. Grzybowski, *Self-assembly at all scales*, Science 295, pp. 2418-2421, 2002. doi: 10.1126/science.1070821.

[34] J. A. Theobald, N. S. Oxtoby, M. A. Phillips, N. R. Champness, P. H. Beton, *Controlling molecular deposition and layer structure with supramolecular surface assemblies*, Nature 424, pp. 1029-1031, 2003. doi: 10.1038/nature01915.

[35] K. Tahara, T. Balandina, S. Furukawa, S. De Feyter, Y. Tobe, *Molecular pentagonal tiling: self-assemblies of pentagonal-shaped macrocycles at liquid/solid interfaces*, Cryst. Eng. Comm. 13, pp. 5551-5558, 2011. doi: 10.1039/C1CE05336A.

[36] S.-S. Jester, E. Sigmund, S. Höger, *Nanopatterning by molecular polygons*, J. Am. Chem. Soc. 133, pp. 11062-11065, 2011. doi: 10.1021/ja203536t.

[37] W. E. Barth, R. G. Lawton, *Dibenzo[ghi,mno]flouranthene*, J. Am. Chem. Soc. 88, pp. 380-381, 1966. doi: 10.1021/ja00954a049.

[38] G. J. Gleicher, *Calculations on the Corannulene system*, Tetrahedron 23, pp. 4257-4263, 1967. doi: 10.1016/S0040-4020(01)88823-2.

[39] J. Janata, J. Gendell, C.-Y. Ling, W. Barth, L. Backes, H. B. Mark, R. G. Lawton, *Concerning the anion and cation radicals of Corannulene*, J. Am. Chem. Soc. 89, pp. 3056-3058, 1967. doi: 10.1021/ja00988a050.

[40] J. C. Hanson, C. E. Nordman, *The Crystal and Molecular Structure of Corannulene, $C_{20}H_{10}$*, Acta Cryst. B32, pp. 1147-1153, 197. doi: 10.1107/S0567740876012430.

[41] H. W. Kroto, J. R. Heath, S. C. O´Brien, R. F. Curl, R. E. Smalley, *C_{60}: Buckminsterfullerene*, Nature 318, pp. 162-163, 1985. doi: 10.1038/318162a0.

[42] L. T. Scott, M. M. Hashemi, D. T. Meyer, H. B. Warren, *Corannulene. A convenient new synthesis*, J. Am. Chem. Soc 113, pp. 7082-7084, 1991. doi: 10.1021/ja00018a082.

[43] A. Borchardt, A. Fuchicello, K. V. Kilway, K. K. Baldridge, J. S. Siegel, *Synthesis and dynamics of the Corannulene nucleus*, J. Am. Chem. Soc. 114, pp. 1921-1923, 1992. doi: 10.1021/ja00031a080.

[44] G. Zimmermann, U. Nuechter, S. Hagen, M. Nuechter, *Synthesis and hydropyrolysis of bis-trimethylsilyl substituted 3-(4H-cyclopenta[def]phenanthrylidene)-1,4-pentadiyne. A new route to corannulene*, Tetrahedron Lett. 35, pp. 4747-4750, 1994. doi: 10.1016/S0040-4039(00)76957-7.

[45] T. J. Seiders, K. K. Baldridge, J. S. Siegel, *Synthesis and Characterization of the first Corannulene cyclophane*, J. Am. Chem. Soc 118, pp. 2754-2755, 1996. 10.1021/ja953734y.

[46] L. T. Scott, P.-C. Cheng, M. M. Hashemi, M. S. Bratcher, D. T. Meyer, H. B. Warren, *Corannulene. A three-step synthesis*, J. Am. Chem. Soc. 119, pp. 10963-10968, 1997. doi: 10.1021/ja972019g.

[47] A. Sygula, P. W. Rabideau, *A practical, large scale synthesis of the Corannulene system*, J. Am. Chem. Soc. 122, pp. 6323-6324, 2000. doi: 10.1021/ja0011461.

[48] Anna M. Butterfield, Bruno Gilomen, Jay S. Siegel, *Kilogram-Scale Production of Corannulene*, Org. Process. Res. Dev. 16, pp. 664-676, 2012. doi: 10.1021/op200387s.

[49] E. Hückel, *Quantentheoretische Beiträge zum Benzolproblem I. Die Elektronenkonfiguration des Benzols und verwandter Verbindungen*, Z. Phys. 70, pp. 204-286, 1931. doi: 10.1007%2FBF01339530.

[50] E. Hückel, *Quantentheoretische Beiträge zum Benzolproblem II. Quantentheorie der induzierten Polaritäten*, Z. Phys. 72, pp. 310-337. doi: 10.1007%2FBF01341953.

[51] E. Hückel, *Quantentheoretische Beiträge zum Problem der aromatischen und ungesättigten Verbindungen. III*, Z. Phys. 76, pp. 628-648, 1932. doi: 10.1007%2FBF01341936.

[52] A. Hirsch, Z. Chen, H. Jiao, *Spherical aromaticity in I_h symmetrical Fullerenes: The $2(n+1)^2$ rule*, Angew. Chem. Int. Ed. 39, pp. 3915-3917, 2000. doi: 10.1002/1521-3773(20001103)39:21<3915::AID-ANIE3915>3.0.CO;2-O.

[53] R. Maag, B. H. Northrop, A. Butterfield, A. Linden, O. Zerbe, Y. M. Lee, K.-W. Chi, P. J. Stang, J. S. Siegel, *Synthesis and X-ray structural analysis of platinum and ethynylplatinum corannulenes: supramolecular tectons*, Org. Biomol. Chem. 7, pp. 4881-4885, 2009. doi: 10.1039/b916020e.

[54] T. J. Seiders, K. K. Baldridge, G. H. Grube, J. S. Siegel, *Structure/Energy correlation of bowl depth and inversion barrier in Corannulene derivatives: Combinded experimental and quantum mechanical analysis*, J. Am. Chem. Soc. 123, pp. 517-525, 2001. doi: 10.1021/ja0019981.

[55] T. J. Seiders, E. L. Elliott, G. H. Grube, J. S. Siegel, *Synthesis of Corannulene and Alkyl derivatives of Corannulene*, J. Am. Chem. Soc 121, pp. 7804-7813, 1999. doi: 10.1021/ja991310o.

[56] G. Chen, R. G. Cooks, E. Corpuz,, L. T. Scott, *Estimation of the electron affinities of* C_{60}*, Corannulene, and Coronene by using the kinetic method*, J. Am. Soc. Mass Spectrom. 7, pp. 619-627, 1996. doi: 10.1016/1044-0305(96)85610-8.

[57] H. Becker, G. Javahery, S. Petrie, P. C. Cheng, H. Schwarz, L. T. Scott, D. K. Bohme, *Gas-phase ion/molecule reactions of corannulene, a fullerene subunit*, J. Am. Chem. Soc, 115, pp. 11636-11637, 1993. doi: 10.1021/ja00077a088.

[58] R. C. Haddon, L. T. Scott, π*-Orbital conjugation and rehybridization in bridged annulenes and deformed molecules in general:* π*-orbital axis vector analysis*, Pure Appl. Chem. 58, pp. 137-142, 1986. doi: 10.1351/pac198658010137.

[59] R. C. Haddon, *Hybridization and the orientation and alignment of* π*-orbitals in nonplanea conjugated organic molecules:* π*-orbital axis vector analysis (POAV2)*, J. Am. Chem. Soc. 108, pp. 2837-2842, 1986. doi: 10.1021/ja00271a009.

[60] M. Parschau, R. Fasel, K.-H. Ernst, O. Gröning, L. Brandenberger, R. Schillinger, T. Greber, A. R. Seitsonen, Y.-T. Wu, J. S. Siegel, *Buckybowls on Metal Surfaces: Symmetry Mismatch and Enatiomorphism of Corannulene on Cu(110)*, Angew. Chem. Int. Ed. 46, pp. 8258-8261, 2007; Angew. Chem. 119, pp. 8406-8409, 2007. doi: 10.1002/anie.200700610.

[61] K. K. Baldridge, J. S. Siegel, *Corannulene-based fullerene fragments* $C_{20}H_{10}$-$C_{50}H_{10}$*: when does a buckybowl become a buckytube?*, Theor. Chem. Acc. 97, pp. 67-71, 1997. doi: 10.1007/s002140050238.

[62] K. K. Baldridge, J. S. Siegel, *Quantum chemical prediction of the* ^{13}C *NMR shifts in alkyl and chlorocorannulenes: correction of chlorine effects*, Theor. Chem. Acc. 120, pp. 95-106, 2008. doi: 10.1007/s00214-007-0291-9.

[63] T. J. Seiders, K. K. Baldridge, E. L. Elliott, G. H. Grube, J. S. Siegel, *Synthesis and quantum mechanical structure of sym-pentamethylcorannulene and decamethylcorannulene*, J. Am. Chem. Soc. 121, pp. 7439-7440, 1999. doi: 10.1021/ja991486q.

[64] B. D. Steinberg, E. A. Jackson, A. S. Filatov, A. Wakamiya, M. A. Petrukhina, L. T. Scott, *Aromatic π-Systems More Curved Than C_{60}. The Complete Family of All Indenocorannulenes Synthesized by Iterative Microwave-Assisted Intramolecular Arylations*, J. Am. Chem. Soc. 131, pp. 10537-10545, 2009. 10.1021/ja9031852.

[65] A. Sygula, A. h. Abdourazak, P. W. Rabideau, *Cyclopentacorannulene: π-Facial Stereoselective Deuterogenation and Determination of the Bowl-to-Bowl Inversion Barrier for a Constrained Buckybowl*, J. Am. Chem. Soc. 118, pp. 339-343, 1996. doi: 10.1021/ja9521987.

[66] B. D. Steinberg, *Examining the boundaries of strained aryl-aryl coupling reactions in polycyclic aromatic hydrocarbons*, Dissertation, Boston College, Departement of Chemistry, 2009.

[67] A. S. Filatov, L. T. Scott, M. A. Petrukhina, *$\pi - \pi$ Interactions and solid state packing trends of polycyclic aromatic bowls in the indenocorannulene family: Predicting potentially useful bulk properties*, Cryst. Growth Des. 10, pp. 4607-4621, 2010. doi: 10.1021/cg100898g.

[68] Y.-T. Wu, T. Hayama, K. K. Baldridge, A. Linden, J. S. Siegel, *Synthesis of Fluoranthenes and Indenocorannulenes: Elucidation of Chiral Stereoisomers on the Basis of Static Molecular Bowls*, J. Am. Chem. Soc. 128, pp. 6870-6884, 2006. doi: 10.1021/ja058391a.

[69] T.-Ch. Wu, H. J. Hsin, M.-Y. Kuo, C.-H. Li, Y.-T. Wu, *Synthesis and Structural Analysis of a Highly Curved Buckbowl Containing Corannulene and Sumanene Fragments*, J. Am. Chem. Soc. 133, pp. 16319-16321, 2011. doi: 10.1021/ja2067725.

[70] T.-C. Wu, M.-K. Chen, Y.-W. Lee, M.-Y. Kuo, Y.-T. Wu, *Bowl-Shaped Fragments of C_{70} or Higher Fullerenes: Synthesis, Structural Analysis, and Inversion Dynamics*, Angew. Chem. Int. Ed. 52, pp. 1289-1293, 2013. doi: 10.1002/anie.201208200.

[71] B. Grünbaum, G. C. Shephard, *Tilings and Patterns*, W. H. Freeman and Company New York, 1986. ISBN: 0-7167-1193-1.

[72] J. H. Conway, H. Burgiel, C. Goodman-Strass, *The Symmetries of Things*, A. K. Peters, Ltd., 2008, ISBN: 978-1-56881-220-5.

[73] A. Dürer, *Underweysung der Messung mit dem Zirckel und Richtscheyt, in Linien, Ebenen unnd gantzen corporen*, Nürnberg, 1538.

[74] J. Kepler, *Astronomi Opera Omnia Vol. 5, Harmonices mundi liber II - De congruentia figurarum harmonicarum* Edited by Ch. Frisch, Heyder & Zimmer, Francofurti, 1864.

[75] R. Penrose, *The role of aesthetics in pure and applied mathematical research*, Bull. Inst. Math. Appl. 10, pp. 266–271, 1974.

[76] D. Shechtman, I. Blech, D. Gratias, J. W. Cahn, *Metallic phase with long-range oriental order and no translational symmetry*, Phys. Rev. Lett. 53, pp. 1951-1953, 1984. doi: 10.1103/PhysRevLett.53.1951.

[77] D. Shechtman, I. A. Blech, *The microstructure of rapidly solidified* Al_6Mn, Metal. Trans. A 16, pp. 1005-1012, 1985. doi: 10.1007/BF02811670.

[78] S. Förster, K. Meinel, R. Hammer, M. Trautmann, W. Widdra, *Quasicrystalline structure formation in a classicla crystalline thin-film system*, Nature 502, pp. 215-218, 2013. doi: 10.1038/nature12514.

[79] S. Sachdev, D. R. Nelson, *Statistical mechanics of pentagonal and icosahedral order in dense liquids*, Phys. Rev. B 32, pp. 1480-1502, 1985. doi: 10.1103/PhysRevB.32.1480.

[80] T. Bauert, L. Merz, D. Bandera, M. Parschau, J. S. Siegel, K.-H. Ernst, *Building 2D crystals from 5-fold symmetry molecules*, J. Am. Chem. Soc. 131, pp.3460-3461, 2009. doi: 10.1021/ja8101083.

[81] Y. L. Duparcmeur, A. Gervois, J. P. Troadec, *Crystallization of pentagon packings*, J. Phys. Condens. Matter 7, pp. 3421-3430, 1995. doi: 10.1088/0953-8984/7/18/006.

[82] T. Schilling, S. Pronk, B. Mulder, D. Frenkel, *Monte Carlo study of hard pentagons*, Phys. Rev. E 71, 036138, 2005. doi: 10.1103/PhysRevE.71.036138.

[83] T. Bauert, K. K. Baldridge, J. S. Siegel, K.-H. Ernst, *Surface-assisted bowl-in-bowl stacking of nonplanar aromatic hydrocarbons*, Chem. Commun. 47, pp. 7995-7997, 2011. doi: 10.1039/c1cc12540k.

[84] T. Bauert, L. Zoppi, G. Koller, A. Garcia, K. K. Baldridge, K.-H. Ernst, *Large induced interface dipole moments without charge transfer: Buckybowls on metal surfaces*, J. Phys. Chem. Lett. 2, pp. 2805-2809, 2011. doi: 10.1021/jz2012484.

[85] T. Bauert, *Fundamental aspects of the self-assembly behavior and electronic properties of Corannulenes*, Dissertation, University of Zurich, Organic Chemistry Institute, 2011.

[86] J.C. Vickermann, I.S. Gilmore, *Surface Analysis - The Principal Techniques 2nd Edition*, Wiley, 2009, ISBN 978-0-470-01763-0.

[87] M. Henzler, W. Göpel, *Oberflächenpysik des Festkörpers*, Teubner, 1994, ISBN 978-3-519-13047-5.

[88] T.A. Carlson, *Photoelectron and Auger Spectroscopy*, Plenum Press, 1975. ISBN: 978-0-306-33901-1.

[89] P.K. Gosh, *Introduction to Photoelectron Spectroscopy*, Wiley, 1975. ISBN: 978-0-471-06427-5.

[90] K. Siegbach, *Electron-Spectroscopy for Atoms, Molecules, and Condensed Matter*, Science 217 (4555), pp. 111-121, 1982. doi: 10.1126/science.217.4555.111

[91] N.H. Turner, J.A. Schreifels, *Surface Analysis: X-ray photoelectron spectroscopy and Auger electron spectroscopy*, Analytical Chemistry 68, pp. 309-331, 1996. doi: 10.1021/a19600146

[92] D. Briggs, M.P. Seah, *Practical Surface Analysis*, Wiley, 1990. ISBN: 978-0-741-26279-4.

[93] R. A. Meyers, *Encyclopedia of Analytical Chemistry: Applications, Theory, and Instrumentation*, Wiley, 2000, ISBN 978-0-471-97670-7.

[94] C.D. Wagner, W.M. Riggs, L.E. Davis, J.F. Moulder, G.E. Muilenberg, *Handbook of X-Ray photoelectron spectroscopy - A reference book of standard data for use in X-Ray photoelectron spectroscopy*, Perkin-Elmer Corporation, Minnesota, 1979.

[95] P.P. Ewald, *Introduction to the Dynamical Theory of X-Ray Diffraction*, Acta Cryst. A25, pp. 103-108, 1969. doi: 10.1107/S0567739469000155.

[96] J. Pendry, *Low energy electron diffraction: the theory and its application to determine of surface structure*, Academic Press, London, 1974. ISBN: 978-0-125-50550-5.

[97] M.A.Van Hove, W.H. Weinberg, C.-M. Chan, *Low-Energy Electron Diffraction - Experiment, Theory and Surface Structure Determination*, Springer Series in Surface Science 6, 1986. ISBN 3-540-16262-3.

[98] K. Oura, V.G. Lifshits, A.A. Saranin, A.V. Zotov, M. Katayama, *Surface Science - An Introduction*, Springer, Berlin, 2003. ISBN 978-3-540-00545-2.

[99] L. Merz, K.-H. Ernst, *Unification of the matrix notation in molecular surface science*, Surf. Sci. 604, pp. 1049-1054, 2010. doi: 10.1016/j.susc.2010.03.023.

[100] J. Bardeen, *Tunneling from a Many-Particle point of view*, Phys. Rev. Lett. 6, pp. 57–59, 1961. doi: 10.1103/PhysRevLett.6.57.

[101] G. Binnig, H. Rohrer, Ch. Gerber, E. Weibel, *Tunneling throuhg a controllable vacuum gap*, Appl. Phys. Lett. 40, 178, 1982. doi: 10.1063/1.92999.

[102] G. Binnig, H. Rohrer, Ch. Gerber, E. Weibel, *Surface Studies by Scanning Tunneling Microscopy*, Phys. Rev. Lett. 49, pp. 57–61, 1982. doi: 10.1103/PhysRevLett.49.57.

[103] G. Binnig, H. Rohrer, Ch. Gerber, E. Weibel, *7x7 Reconstruction on Si(111) Resolved in Real Space*, Phys. Rev. Lett. 50, pp. 120–123, 1983. doi: text10.1103/PhysRevLett.50.120.

[104] G. Binnig, H. Rohrer, *The scanning tunneling microscope*, Sci. Am., Vol. 253, pp. 50-56, 1985. doi: 10.1038/scientificamerican0885-50.

[105] G. Binnig, H. Rohrer, *In touch with atoms*, Rev. Mod. Phys. 71, No. 2, pp. S324-S330, 1999. doi: 10.1103/RevModPhys.71.S324.

[106] P.W. Atkins, R.S. Friedman, *Molecular Quantum Mechanics*, Oxford University Press, 5th Ed, 2010. ISBN: 978-0-19-954142-3.

[107] J. Tersoff, D.R. Hamann, *Theory of the scanning tunneling microscope*, Phys. Rev. B 31, pp. 805-813, 1985. doi: 10.1103/PhysRevB.31.805.

[108] C.J. Chen, *Origin of atomic resolution on metal surfaces in scanning tunneling microscopy*, Phys. Rev. Lett. 65, pp. 448–451, 1990. doi: 10.1103/PhysRevLett.65.448.

[109] C.J. Chen, *Introduction to Scanning Tunneling Microscopy*, Oxford University Press, 2nd Ed, 2008. ISBN: 978-0-19-921150-0.

[110] C. F. Quate, *Vacuum tunneling: A new technique for microscopy*, Physics Today, Vol. 39, pp. 26-33, 1986. doi: 10.1063/1.881071

[111] Y. Kuk, P.J. Silverman, *Scanning tunneling microscope instrumentation*, Rev. Sci. Instrum. 60, pp. 165-180, 1989. doi: 10.1063/1.1140457.

[112] I. Horcas, R. Fernández, J. M. Gómez-Rodríges, J. Colchero, J. Gómez-Herrero, A. M. Baro, *WSXM: A software for scanning probe microscopy and a tool for nanotechnology*, Rev. Sci. Instrum. 78, 013705, 2007. doi: 10.1063/1.2432410.

[113] C.N. Banwell, *Fundamentals of molecular spectroscopy*, London, McGraw-Hill, 1966. ISBN: 978-0-071-28221-5.

[114] P.R. Griffiths, J.A. de Haseth, *Fourier transform infrared spectrometry*, Hoboken, Wiley, 2007. doi: 10.1002/047010631X.

[115] L. Merz, M. Parschau, J. S. Siegel, K.-H. Ernst, *Condensation of Fivefold-Symmetric Molecules in Two Dimensions*, CHIMIA 63, pp. 214-216, 2009. doi: 10.2533/chimia.2009.214.

[116] L. Merz, T. Bauert, M. Parschau, G. Koller, J. S. Siegel, K.-H. Ernst, *Polymorph selection in 2D crystals by phase transition blocking*, Chem. Commun. 39, pp. 5871-5873, 2009. doi: 10.1039/b911056a.

[117] L. Merz, M. Parschau, L. Zoppi, K. K. Baldridge, J. S. Siegel, K.-H. Ernst, *Reversible Phase Transition in a Buckybowl Monolayer*, Angew. Chem. Int. Ed. 48, pp. 1966-1969, 2009. Angew. Chem. 121, pp. 2000-2003, 2009. doi: 10.1002/anie.200804563.

[118] T. Bauert, K. K. Baldridge, J. S. Siegel, K.-H. Ernst, *Surface-assisted bowl-in-bowl stacking of nonplanar aromatic hydrocarbons*, Chem. Commun. 47, pp. 7995-7997, 2011. doi: 10.1039/c1cc12540k.

[119] M. Juhasz, S. Hoffmann, E. Stoyanov, K.-C. Kim, C. A. Reed, *The Strongest Isolable Acid*, Angew. Chem. Int. Ed. 43, pp. 5352-5355, 2004. doi: 10.1002/anie.200460005.

[120] S. Duttwyler, A. M. Butterfield, J. S. Siegel, *Arenium Acid Catalyzed Deuteration of Aromatic Hydrocarbons*, J. Org. Chem. 78, pp. 2134-2138, 2013. doi: 10.1021/jo302201a.

[121] G.H. Grube, E. L. Elliott, R. J. Stettens, C. S. Jones, K. K. Baldridge, J. S. Siegel, *Synthesis and Properties of sym-Pentasubstituted Derivatives of Corannulene*, Org. Lett. 5, pp. 713-716, 2003. doi: 10.1021/ol027565f.

[122] A. H. Abdourazak, A. Sygula, P. W. Rabideau, *"Locking" the bowl-shaped geometry of corannulene: Cyclopentacorannulene*, J. Am. Chem. Soc. 115, pp. 3010-3011, 1993. doi: 10.1021/ja00060a073.

[123] H. A. Wegner, L. T. Scott, A. de Meijere, *A new Suzuki-Heck-Type coupling cascade: Indeno[1,2,3]-annelation of polycyclic aromatic hydrocarbons*, J. Org. Chem. 68, pp. 883-887, 2003. doi: 10.1021/jo020367h.

[124] Y.-T. Wu, J. S. Siegel, *Aromatic molecular-bowl hydrocarbons: Synthetic derivatives, their structure, and physical properties*, Chem. Rev. 106, pp. 4843-4867. 2006. doi: 10.1021/cr050554q.

[125] Mark D. Clayton, Peter W. Rabideau, *Synthesis of a New $C_{32}H_{12}$ Bowl-Shaped Aromatic Hydrocarbon*, Tetrahedron Letters 38, pp. 741-744, 1997. doi: 10.1016/S0040-4039(96)02450-1.

[126] A. K. Geim, K. S. Novoselov, *The rise of graphene*, Nature Mater. 6, pp. 183-191, 2007. doi: 10.1038/nmat1849.

[127] Amit Kumar-Dutta, Dissertation to be published, University of Zurich, Institute of Organic Chemistry, 2013.

[128] L. Zoppi, A. Garcia, K. K. Baldridge, *Theoretical Investigation of the Binding Process of Corannulene on a Cu(111) Surface*, j. Phys. Chem. A 114, pp. 8864-8872, 2010. doi: 10.1021/jp102662t.

[129] L. Zoppi, T. Bauert, J. S. LSiegel, K. K. Baldridge, K.-H. Ernst, *Pentagonal tiling with buckybowls: pentamethylcorannulene on Cu(111)*, Phys. Chem. Chem. Phys. 14, pp. 13365-13369, 2012. doi: 10.1039/c2cp41732d.

[130] B. H. Stuart, *Infrared spectroscopy: fundamentals and applications*, John Wiley & Sons Ltd., 2005. ISBN: 978-0-470-85428-0.

[131] B. C. Smith, *Infrared spectral interpretation: a systematic approach*, CRC Press, 1998. ISBN: 0-8493-2463-7.

[132] R. M. Silverstein, F. X. Webster, D. Kiemle, *Spectrometic identification of organic compounds*, John Wiley & Sons, 7th Ed., 2005. ISBN: 978-0-471-39362-7.

[133] D. Pappo, T. Mejuch, O. Reany, E. Solel, M. Gurram, E. Keinan, *Diverse functionalization of corannulene: easy access to pentagonal superstructure*, Org. Lett. 11, pp. 1063-1066, 2009. doi: 10.1021/ol8028127.

[134] P. Angelova, E. Solel, G. Parvari, A. Turchanin, M. Botoshansky, A. Gölzhäuser, E. Keinan, *Chemisorbed monolayers of corannulene penta-thioethers on gold*, Langmuir 29, pp. 2217-2223, 2013. doi: 10.1021/la304600s.

[135] M. Feng, H. Petek, *Atomlike, hollow-core-bound molecular orbitals of C_{60}*, Science 320, pp. 359-362, 2008. doi: 10.1126/science.1155866.

[136] M. Feng, J. Zhao, T. Huang, X. Zhu, H. Petek, *The electronic properties of superatom states of hollow molecules*, Acc. Chem. Res. 44, pp. 360-368, 2011. doi: 10.1021/ar1001445.

[137] N. J. Smith, *Towards the synthesis of a carbon nanotube end-cap: application of a new benzannulation method to the first synthesis of pentabenzo[a,d,g,j,m]corannulene*, Dissertation, Boston College, Dezember 2011.

[138] S. Schrettl, H. Frauenrath, *Elements for a rational polymer approach towards carbon nanotubes*, Angew. Chem. Int. Ed. 51, pp. 6569-6571, 2012. Angew. Chem. 124, pp. 6673-6675, 2012. doi: 10.1002/anie.201201423.

[139] M. Mojica, F. Méndez, J. A. Alonso, *Growth of fullerene fragments using the Diels-Alder cycloaddition reaction: First step towards a C_{60} synthesis by dimerization*, Molecules 18, pp. 2243-2254, 2013. doi: 10.3390/molecules18022243

[140] T. Hayama, *Synthesis and properties of corannulene derivatives: Journey to materials chemistry and chemical biology*, Dissertation, University of Zurich, 2008.

[141] J. M. Quimby, *Fivefold annulation of corannulene as a route toward carbon nanotubes and nanocones*, Dissertation, Boston College, May 2011.

[142] U. H. F. Bunz, S. Menning, N. Martín, *para-Connected cyclophenylenes and hemispherical polyarenes: building blocks for single-walled carbon nanotubes?*, Angew. Chem. Int. Ed. 51, pp. 7094-7101, 2012. doi: 10.1002/anie.201201494.

[143] L. T. Scott, E. A. Jackson, Q. Zhang, B. D. Steinberg, M. Bancu, B. Li, *A short, rigid, structurally pure carbon nanotube by stepwise chemical synthesis*, J. Am. Chem. Soc, 134, pp. 107-110, 2012. doi: 10.1021/ja209461g.

[144] O. Jones, *The Grammar of Ornament*, Day and Son, London, 1868.

[145] M. F. S Freiherr von Gagern, *Computergestützes Zeichnen in den Symmetriegruppen der euklidischen Ebene*, Diploma-Thesis, Fakultät für Informatik, TU München, 2008.

[146] C. Brabec, V. Dyakonov, U. Scherf, *Organic Photovoltaics - Materials, Device Physics, and Manufacturing Technologies*, Wiley-VCH, 2013. doi: 978-3-527-62320-4.

[147] A. Goetzberger, C. Hebling, H.-W. Schock, *Photovoltaic materials, history, status and outlook*, Mat. Sci. Eng. R. 40, pp. 1-46, 2003. doi: 10.1016/S0927-796X(02)00092-X.

[148] G. Mariani, A. C. Scofield, C.-H. Hung, D. L. Huffaker, *GaAs nanopillar-array solar cells employing in site surface passivation*, Nat. Commun. 4, pp. 1497-, 2013. doi: 10.1038/ncomms2509.

[149] L. Kranz, C. Gretener, J. Perrenoud, R. Schmitt, F. Pianezzi, F. La Mattina, P. Blösch, E. Cheah, A. Chirilă, C. M. Fella, H. Hagendorfer, T. Jäger, S. Nishiwaki, A. R. Uhl, S. Beucheler, A. N. Tiwari, *Doping of polycrystalline CdTe for high-efficiency solar cells on flexible metal foil*, Nat. Commun. 4, pp. , 2013. doi: 10.1038/ncomms3306.

[150] A. N. Tiwari, M. Hagmann, *A new world record for solar cell efficiency*, Media release, Empa, 18 January 2013.

[151] I. Chung, B. Lee, J. He, R. P. H. Chang, M. G. Kanatzidis, *All-solid-state dye-sensitized solar cells with high efficiency*, Nature 485, pp. 486-489, 2012. doi: 10.1038/nature11067.

[152] A. Einstein, *Über einen die Erzeugung und Verwandlung des Lichtes betreffenden heuristischen Gesichtspunkt*, Ann. Phys. 322, pp. 132-148, 1905. doi: 10.1002/andp.19053220607.

[153] P. T. Landsberg, *An introduction to the theory of photovoltaic cells*, Solid-State Electron 18, pp. 1043-1052, 1975. doi: 10.1016/0038-1101(75)90165-3.

Publications

- Q. S. Stöckl, D. Bandera, C. S. Kaplan, J. S. Siegel, K.-H. Ernst,
  Gear-Meshed Tiling of Surfaces with Molecular Pentagonal Stars,
  J. Am. Chem. Soc. 136 (2), pp. 606-609, 2014. doi: 10.1021/ja411279r.
- J. Prinz, R. Gaspari, Q. S. Stoeckl, P. Gille, M. Armbrüster, H. Brune, O. Gröning, C. A. Pignedoli, D. Passerone, R. Widmer,
  Ensemble effect evidence by CO adsorption on the threefold PdGa surfaces,
  J. Phys. Chem. C, 118 (23), pp. 12260-12265, 2014. doi: 10.1021/jp501584f.
- J. Prinz, C. A. Pignedoli, Q. S. Stöckl, M. Armbrüster, H. Brune, O. Gröning, R. Widmer, D. Passerone,
  Adsorption of Small Hydrocarbons on the Three-Fold PdGa surfaces: The Road to Selective Hydrogenation,
  J. Am. Chem. Soc. 136 (33), pp. 11792-11798, 2014. doi: 10.1021/ja505936b.

Curriculum Vitae

Surname, given names	STÖCKL, Quirin Sebastian
Date of birth	January 15, 1985
Citizenship	Germany

Education

1997-2001	Staatlich Realschule Ergolding, Germany - subject area: engineering
2001-2003	Fachoberschule Landshut, Germany - subject area: engineering
2004-2008	University of Applied Sciences Landshut Mechanical Engineering (Dipl.-Ing. (FH)) Diploma thesis on "Hochtemperatur Kriechverhalten oxidischer Faserkeramiken mit partiell einkristallinen Verstärkungsfasern" in the group for composite materials of Dr.-Ing. B. Thielicke, Fraunhofer Institute for Mechanics of Materials IWM, Freiburg, Germany.
2008-2010	University of Applied Sciences Regensburg Mechanical Engineering (M. Sc.) Master thesis on "Kriechverhalten der AlSi6Cu4-Gusslegierung bei hohen Verformungsgeschwindigkeiten" in the group for materials testing and metallography (LWM) of Prof. Dr. J. Hammer, University of Applied Sciences Regensburg, Germany.
2009-2010	Non-scientific employee at the windtunnel and flow measurement laboratory (LWS) of Prof. Dr. S. Lämmlein, University of Applied Sciences Regensburg, Germany.
2010-2014	University of Zurich PhD student in the research area of Molecular Surface Science in the group of Prof. Dr. K.-H. Ernst, Nanoscale Materials Science, Empa - Swiss Federal Laboratories for Materials Science and Technology, Dübendorf, Germany. Supported by the Swiss National Science Foundation (SNF) (126776 and 144509)

Acknowledgments

A thankful heart is not only the greatest virtue,
but the parent of all other virtues..

Marcus Tullius Cicero, (106 – 43 AC)

So I would like to conclude my thesis with saying thank you very much. My thanks to all who have supported me during this period, contributing to the success of my studies.

First and foremost I want to thank you Heidi and my parents, my brother, and my sister for giving me such hearty support all the time and understanding the ups and downs of PhD studies.

In particular I would like to thank my supervisor and doctoral father Karl-Heinz Ernst (Kalle) for giving me the opportunity to join his group and support in the laboratory. Also to Jay Siegel at the University of Zurich for supplying the molecules and mentoring, Hans Hug for your reviews, discussions, and support.
Furthermore, special thanks to Manfred Parschau for the excellent technical support and discussions, and for his way of helping out whenever needed. Georg Simon for long scientific discussions and help with the experiments. Also Chrysanthi Karageorgaki, Johannes Seibel, Andreas Bliersbach, and Jingyi Li for helping with the lab-equipment, experiments, and good evenings outside the lab.

I also thank all colleagues at Empa and the Departement of Nanoscale Materials Science, which have strengthened me during the thesis work and provided advice and assistance whenever needed. To Tobias Bauert and Christian Roth for their great insight and support in explaining to me all the equipment.

A big thanks to all friends who motivated me during my studies again and again and provided the necessary distraction from lab-work.

Financial support of the Swiss National Science Foundation (SNF) is gratefully acknowledged.

Thanks to all of you!